ABSTRACT

Title of Dissertation: IMPROVED SATELLITE MICROWAVE RETRIEVALS AND THEIR INCORPORATION INTO A SIMPLIFIED 4D-VAR VORTEX INITIALIZATION USING ADJOINT TECHNIQUES

Xiaoxu Tian, Doctor of Philosophy, 2017

Dissertation directed by: Professor Xiaolei Zou
Earth System Science Interdisciplinary Center

Microwave instruments provide unique radiance measurements for observing surface properties and vertical atmosphere profiles in almost all weather conditions except for heavy precipitation. The Advanced Microwave Scanning Radiometer 2 (AMSR2) observes radiation emitted by Earth at window channels, which helps to retrieve surface and column integrated geophysical variables. However, observations at some X- and K-band channels are susceptible to interference by television signals transmitted from geostationary satellites when AMSR2 is scanning regions including the U.S. and Europe, which is referred to as Television Frequency Interference (TFI). It is found that high reflectivity over the ocean surface is favorable for the television signals to be reflected back to space. When the angle between the Earth scene vector

and the reflected signal vector is small enough, the reflected TV signals will enter AMSR2's antenna. As a consequence, TFI will introduce erroneous information to retrieved geophysical products if not detected. This study proposes a TFI correction algorithm for observations over ocean.

Microwave imagers are mostly for observing surface or column-integrated properties. In order to have vertical temperature profiles of the atmosphere, a study focusing on the Advanced Technology Microwave Sounder (ATMS) is included. A traditional AMSU-A temperature retrieval algorithm is modified to remove the scan biases in the temperature retrieval and to include only those ATMS sounding channels that are correlated with the atmospheric temperatures on the pressure level of the retrieval. The warm core structures derived for Hurricane Sandy when it moved from the tropics to the mid-latitudes are examined.

Significant improvements have been obtained for the forecasts of hurricane track, but not intensity, especially during the first 6-12 hours. In this study, a simplified four-dimensional variational (4D-Var) vortex initialization model is developed to assimilate the geophysical products retrieved from the observations of both microwave imagers and microwave temperature sounders. The goal is to generate more realistic initial vortices than the bogus vortices currently incorporated in the Hurricane Weather Research and Forecasting (HWRF) model in order to improve hurricane intensity forecasts. The case included in this study is Hurricane Gaston (2016). The numerical results show that the satellite geophysical products have a desirable impact on the structure of the initialized vortex.

IMPROVED SATELLITE MICROWAVE RETRIEVALS AND THEIR INCORPORATION INTO A SIMPLIFIED 4D-VAR VORTEX INITIALIZATION USING ADJOINT TECHNIQUES

by

Xiaoxu Tian

Dissertation submitted to the Faculty of the Graduate School of the
University of Maryland, College Park, in partial fulfillment
of the requirements for the degree of
Doctor of Philosophy
2017

Advisory Committee:
Professor Kayo Ide, Chair
Adjunct Professor Xiaolei Zou, Co-Chair
Professor Fernando Miralles-Wilhelm
Professor Russell R. Dickerson
Dr. Fuzhong Weng
Professor Michael N. Evans, Dean's Representative

Acknowledgements

First and foremost, I thank my research advisor, Dr. Xiaolei Zou, for her continuous support, patience, and motivations. Her guidance helped me in all times of my research and thesis writing. I couldn't have think of a better advisor and mentor for my Ph.D. study. My special thanks go to Dr. Kayo Ide, Dr. Fuzhong Weng, Dr. Fernando Miralles-Wilhelm, Dr. Russell R. Dickerson, and Dr. Michael N. Evans for their insightful comments on my dissertation.

My sincere gratitude also goes to my labmates for our stimulating discussions and for all the fun we have had during the years we were together. I would like to thank NOAA for providing the observation data of the ATMS and AMSU-A, and JAXA for the data of AMSR2. Without these nicely distributed observational data, this research wouldn't have been possible.

Last but not least, I dedicate my dissertation to my family, including my son who is about to join us, for their unconditional support and love.

Table of Contents

List of Tables

List of Figures

Chapter 1: Introduction

1.1 Motivation of Research

Tropical cyclones generally appear and develop over oceans where conventional observations are often rare or unavailable. Since 1990s, meteorological satellites have been providing abundant observations globally. In deep convective and precipitating atmosphere, satellite measurements at the infrared spectrum are only sensitive to the cloud top information and are not able to sense the internal atmospheric structures. Up to today, the operational Hurricane Weather Research and Forecasting (HWRF) model is initialized with empirically specified vortices (Liu et al. 2006) without much relying on satellite data. Essentially, the vortices in the Global Forecast System (GFS) are firstly removed and replaced with an empirically specified bogus vortices (Kurihara et al. 1995) because the vortices from the global model tend to be either too weak or misplaced. The specific procedures include 1) removing the poorly analyzed tropical cyclone vortices from the large-scale analysis, 2) empirically specifying a wind field, 3) generating all other model variables by solving the balance model with the specified wind field, 4) obtaining an asymmetric wind component by integrating a simplified barotropic model with the axisymmetric initial condition, and 5) adjusting the mass fields based on the divergence equation. In the above five procedures, only a few observed parameters including maximum wind, radius of the maximum wind, and central sea level pressures are considered when specifying the wind field. While the hurricane thermal and dynamic structure can vary from case to case, the vortex initialization process is the same as specified from above steps.

Therefore, in this study, a 4D Variational (4D-Var) scheme is developed to initialize the hurricane vortex through assimilating the satellite observed vortex features.

In this new satellite-driven hurricane vortex initialization scheme, some of surface and atmospheric parameters within the hurricanes are retrieved from two satellite microwave instruments and then used for assimilation. The observations at K/Ka bands from the Advanced Microwave Scanning Radiometer 2 (AMSR2) are sensitive to total precipitable water (TPW), liquid water path (LWP) (Weng and Grody 1994) whereas those at C and X bands can be used to derive the sea surface temperatures (SST). However, it is known that AMSR2 observations over ocean are subject to interference by TV signals that are also known as Television Frequency Interferences (TFI). Therefore, before assimilating the retrieved geophysical variables for vortex initialization, a TFI correction model is developed to detect and correct the interfered observations (Chapter 3). Additionally, the three-dimensional temperature field of the atmosphere can be retrieved with the observations of the Advanced Technology Microwave Sounders (ATMS). Previous studies (Zhu and Weng 2013; Zhu et al. 2002) proposed a retrieval algorithm (referred to the traditional retrieval algorithm hereafter) with microwave temperature sounding instruments including the Advanced Microwave Sounding Unit (AMSU)-A and ATMS. The retrieved temperatures were applied in hurricane cases for warm core structure analysis. It is found that the atmospheric temperatures from the traditional retrieval algorithm display some angular dependent bias and the bias has some irregularities across the scan direction. Hence, a modified temperature retrieval algorithm is also proposed in this study and described in Chapter 4. The improved temperature fields from our

modified algorithm are illustrated by comparing with those from the traditional algorithm, the Microwave Integrated Retrieval System (MIRS), and the European Center for Medium range Weather Forecasting (ECMWF) interim reanalysis within the selected hurricane cases.

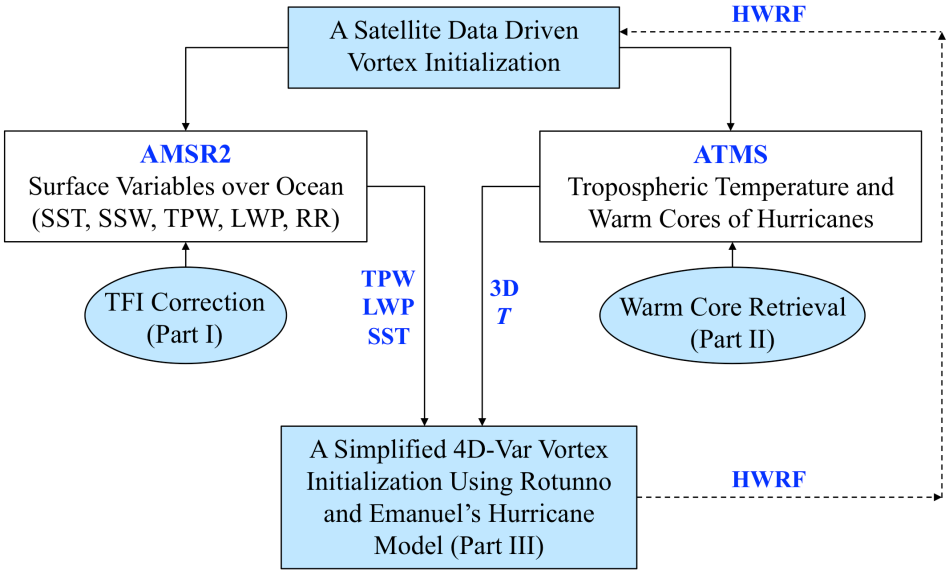

Figure 1.1: A flow chart illustrating the motivation of this dissertation.

Both the AMSR2 observed surface and ATMS observed atmospheric features are then incorporated into a 4D-Var vortex initialization model developed based on an axisymmetric hurricane model proposed by Rotunno and Emanuel (1987), which was originally developed to verify the air-sea interaction theory described in (Emanuel 1986) (Chapter 5). As shown in Fig. 1.1, the initialization model assimilates TPW and LWP retrieved from AMSR2 observations and three-dimensional atmospheric temperature field retrieved from ATMS observations. In future studies, the initialized vortices obtained by the proposed 4D-Var scheme will be incorporated in HWRF system to improve hurricane track and intensity forecasts.

1.2 Television Frequency Interferences in AMSR2

The Advanced Microwave Scanning Radiometer 2 (AMSR2) is onboard the Global Change Observation Mission—Water 1 (GCOM-W1) satellite, which was successfully launched onto a sun-synchronous orbit at an altitude of 705 km on May 17, 2012. As the successor of AMSR-E carried by Aqua satellite, AMSR2 inherited all AMSR-E's channels from 6.925 to 89.0 GHz, and it has an additional pair of dual-polarized channels with center frequencies at 7.3 GHz (Kachi et al. 2008). The purpose of adding the 7.3-GHz channels is for mitigating radio frequency interference (RFI). Other passive microwave conical-scanning radiometer instruments similar to AMSR-E include the WindSat radiometer onboard the Coriolis satellite and the Microwave Radiation Imager onboard the FY3B and FY3C satellites. The 6.926 (C-band), 10.65 (X-band), and 18.7 (K-band) channels of these instruments can be applied for retrievals of geophysical variables over both ocean (Wilheit et al. 2003) and land (Kelly et al. 2003; Njoku and Li 1999; Njoku et al. 2003; Zou et al. 2012). However, these low-frequency channels are located in unprotected bands and are exposed to signals from ground-based and/or space-based military or commercial active sensors (Zhao et al. 2013; Zou et al. 2014; Zou et al. 2012).

Over ocean, the primary source of interference is the geostationary TV satellites that transmit TV signals at frequencies that are within the bandwidth of radiometer channels (Adams et al. 2010; Truesdale 2013). The ocean surface has a relatively higher reflectivity compared with that of the land surface due to a high permittivity of seawater. When the TV signals transmitted by the geostationary satellite reach the sea surface, a portion of the signals could be reflected back toward

space. When a radiometer's antenna happens to be facing the reflected signal, these reflected TV signals will be mixed with the natural radiation emitted by the Earth surface (Figure 1.2). The interferences of the radiance measurements from the meteorological satellite radiometric instruments with TV signals reflected off the ocean surface are known as television frequency interferences (TFIs).

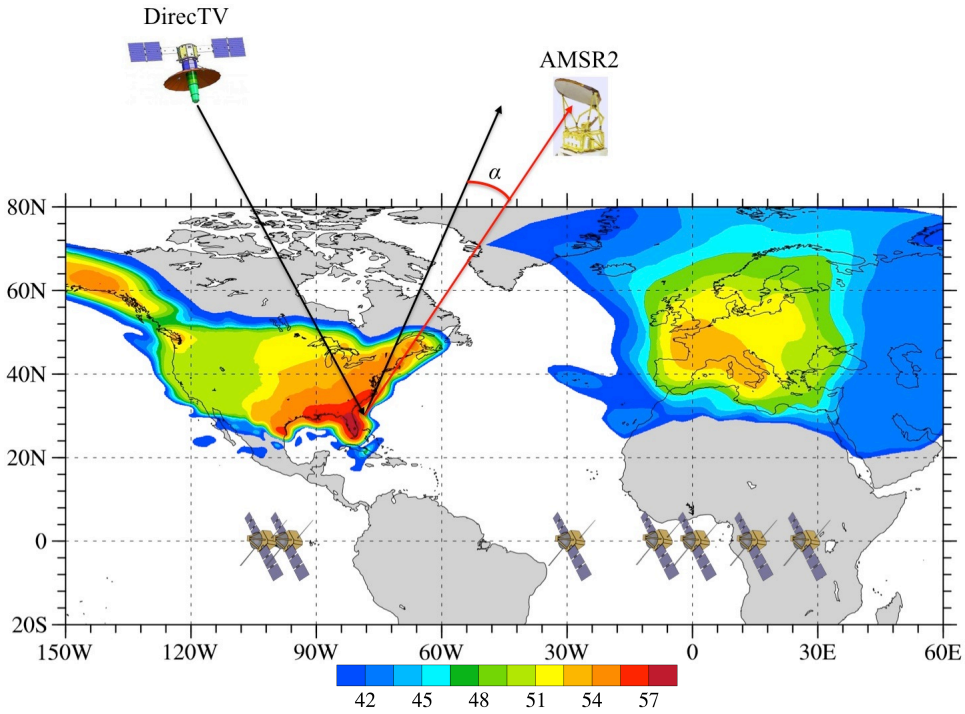

Figure 1.2: Radio signal intensity (unit: dBW) from DirecTV 11 located at 102.8˚W and Eutelsat 13B at 13.5˚E (color shading), as well as a schematic illustration of the reflection of TV signals (black arrow) off the ocean surface, an earth emission into the AMSR2 field-of-view (red arrow), and the glint angle (α). Locations of two geostationary satellites over United States (DirecTV 11, DirecTV 12) and five geostationary satellites over Europe (Hispasat 1E, Eutelsat West 7A, Thor 6, Hot Bird 13B, Astra 2E) located above the equator are indicated by a schematic satellite image.

In Europe, over five TV satellites are operating at X-bands that overlap with the AMSR2 10.65-GHz channels. Over North America, the DirecTV satellite groups operate at frequencies close to the K-band channels of radiometers (Wentz and

Meissner 2000; Wiltshire et al. 2004). The occurrence of TFI, if not detected and corrected, would introduce erroneous information into radiance observations and then to AMSR2-retrieved geophysical products, such as total precipitable water (TPW), liquid water path (LWP), sea surface wind (SSW), and sea surface temperatures (SSTs) (Weng and Grody 1994; Wentz and Meissner 2000; Yan and Weng 2008).

Numerous previous studies had attempted to identify the TFI among observations in order to minimize the detrimental impacts of TFI on meteorological satellite observations. Li et al. (2006) proposed a regression method to predict the TFI-free brightness temperature for the interfered channels with the aid of other channels. The accuracies of such regression-predicted brightness temperatures are promising. However, derivations of the regression coefficients require observation data from a long time period (e.g., six months in Li et al. (2006)). Adams et al. (2010) developed an algorithm to detect the interference based on the goodness-of-fit between the modeled and measured brightness temperatures, which are essentially chi-square probability. McKague et al. (2010) pointed out an existence of TFI signals at K band over land that could be reflected by snow surfaces based on the maximum differences of brightness temperature measurements between 19 and 22 GHz at the same polarization over a winter month period. In this paper, an empirical model is developed for evaluating the occurrence and intensity of TFI over ocean. This model is based on the same principle used by Yang and Weng (2016) for mitigation of lunar contamination in the Advanced Technology Microwave Sensor (ATMS) observations. A quantitative determination of TFI contribution to an AMSR2 observation can be derived given the TFI glint angle, which is defined as the angle

between the direction that the radiometer's antenna faces and the direction of the reflected TV signal, latitude, longitude, sensor zenith, and sensor azimuth angles of the AMSR2 observation as well as the background TV signal intensity of each relevant geostationary TV satellite that could be affecting the area of interest. The calculation of TFI correction using this empirical model does not involve any AMSR2 radiance observations, as did the earlier methods.

McKague et al. (2010) investigated the possible interference by TV signals to observations of WindSat, AMSR-E, and SSMI. The accumulated maximum spectral differences between observations of channels at 18.7 GHz and those at 23.8 GHz showed that K-band channel observations over land are likely to be interfered by TV signals reflected from snow surfaces. Zou et al. (2014) pointed out that, the TFI glint angle, i.e., the angle between the line-of-sight vector and the reflected TV signal vector, is a necessary condition for the interference to occur. This research develops a TFI detection algorithm based on principal component analysis (PCA) with TFI glint angles as the constraint. Since TFI is caused by reflected TV signals, it is not correlated with natural emission from a snow-covered land surface. Based on this characteristic, the PCA can isolate the TFI from the observations even when obscured by snow. Numerical results are made with AMSR2 L1B observation data.

1.3 Tropical Cyclones and Temperature Sounder Observations

Tropical cyclones (TCs) emerge and intensify over the oceans. Only a handful of in situ measurements are available for observing TCs: sparsely distributed buoys, weather stations over islands, ships, in situ temperature sensors equipped on airplanes, and aircraft dropsondes. In comparison, meteorological satellites are able to

provide remote sensing observations within and around TCs with high horizontal, vertical, and/or temporal resolutions. Of particular interest for TC observations and numerical weather prediction are infrared and microwave instruments. A polar-orbiting satellite provides global radiance measurements at microwave and infrared frequencies twice daily. A geostationary satellite can provide time-continuous visible and infrared radiance observations within its observing disk centered at its subsatellite point at the equator. The infrared instruments such as Atmospheric Infrared Sounder, Infrared Atmospheric Sounding Interferometer, and Cross-track Infrared Sounder are extremely valuable for providing radiance measurements with thousands of channels for profiling the atmospheric temperature and water vapor with high vertical resolutions (Chen et al. 2013; Hilton et al. 2011; Janssen 1993; LeMarshall et al. 2006). However, the infrared channels cannot penetrate the clouds except for optically thin clouds (e.g., cirrus), while tropical cyclones are dominated with thick clouds. In contrast, microwave instruments do not provide as many channels as infrared sounders but can provide unique radiance measurements for profiling the atmospheric temperature and water vapor in almost all weather conditions except for heavy precipitation (Weng et al. 2003). Observations from microwave sounders for window channels are also sensitive to cloud liquid water path and ice water path (Ferraro et al. 1996; Weng and Grody 1994). Since the radiances observed by microwave sounders above the top of atmosphere sample atmosphere layers at different altitudes, it is possible to retrieve atmospheric temperatures in the troposphere and stratosphere from the temperature sounding channels. Hence,

microwave sounders are unique for observing TCs populated by clouds, and infrared sounders are important for observing TC's environments.

The Suomi National Polar-orbiting Partnership (S-NPP) satellite was successfully launched on 28 October 2011 into a Sun-synchronous orbit with an ascending equator crossing local time of 1:30 P.M. (Weng et al. 2012). The Advanced Technology Microwave Sounder (ATMS) on board S-NPP is a total power cross-track microwave radiometer. It is an advanced successor of both Advanced Microwave Sounding Unit-A (AMSU-A) and Microwave Humidity Sounder (MHS) to provide spectrum samplings from the Earth's surface to the stratosphere. Kidder et al. (2000) gave a comprehensive overview of applying AMSU data in estimating TC intensities, retrieving upper tropospheric temperature anomalies, and determining TC precipitation potentials. Spencer and Braswell (2001) estimated TC maximum sustained wind (MSW) using the temperature gradient derived from AMSU-A measurement. Demuth et al. (2004) and Demuth et al. (2006) developed algorithms to apply AMSU observations in evaluating the maximum sustained wind (MSW), minimum sea level pressure, and radii of winds of TCs. Zou et al. (2013) found consistently positive impacts of assimilating ATMS observations on hurricane track and intensity forecasts. Compared with its predecessors AMSU-A and MHS, ATMS has more channels, improved spatial resolutions, and a wider swath width. It has much smaller gaps between two consecutive ATMS swaths than AMSU-A swaths in the low latitudes. Given the above-mentioned advantages of ATMS over AMSU-A, ATMS can provide a much better depiction of the thermal structures associated with TCs than AMSU-A. The microwave temperature sounding observations from ATMS

on board the S-NPP satellite will be used for deriving the warm core structures of TCs in this study (Weng et al. 2012; Zhu and Weng 2013).

Zhu et al. (2002) proposed an atmospheric temperature retrieval algorithm for AMSU-A observations. Based on the fact that AMSU-A brightness temperatures at temperature sounding channels respond linearly to the temperature within various atmosphere layers, they successfully applied a linear regression atmospheric temperature retrieval algorithm for obtaining warm core structures of hurricanes in the middle and upper troposphere. Recently, Zhu and Weng (2013) applied the same temperature retrieval algorithm to ATMS observations to obtain the vertical temperature structures of Hurricane Sandy (2012). They found that unlike a typical TC for which the AMSU-A-retrieved warm core was found in the upper troposphere (Zhu et al. 2002), the ATMS-retrieved warm cores of Hurricane Sandy extended throughout the troposphere with quite large horizontal sizes.

The TC's warm core formation, intensification, and structures in the middle and upper troposphere and low stratosphere are closely related to TC evolution. Galarneau et al. (2013) investigated the dynamical processes that contribute to the intensifications of Hurricane Sandy during its warm core seclusion. Dolling and Barnes (2011) investigated the formation of the TC warm core and its role in the evolution of TCs. Through model simulations, Zhang and Chen (2012) showed an important role of the development and intensification of upper level warm core to the rapid intensification (RI) of Hurricane Wilma (2005). The formation of an upper level warm core from the descending stratospheric air in the eye was associated with the detrainment of convective bursts in the eyewall. At the completion of RI, the warm

core reached its peak magnitude of more than 18 K at the time when the model-predicted Hurricane Wilma achieved the peak intensity. There were cyclonic radial inflows above the upper outflow layer that could have caused the subsidence adiabatic warming. Given the importance of warm core structures on TC intensity changes, satellite microwave temperature soundings can be utilized in vortex initialization of TCs (Boukabara et al. 2011; Kurihara et al. 1993; Kurihara et al. 1995; Wang 1995; Zou and Xiao 2000; Zou et al. 2015; Zou et al. 2013) for better forecasting and monitoring of TCs. In this study, the original algorithm developed by Zhu et al. (2002) is modified for better capturing TC warm core structures based on the brightness temperature measurements from ATMS. The first modification is to establish a regression model at each scan angle of ATMS in order to remove scan biases in temperature retrievals. The second modification is to use only the most highly correlated channels for retrieving atmospheric temperatures at each specific pressure level. The revised algorithm is applied to ATMS observations for Hurricane Sandy during its entire life cycle.

1.4 Vortex Initializations and Hurricane Predictions

Improving the accuracy of hurricane track and intensity forecasts has been of significant importance but challenging. A hurricane landfall in a densely populated region can result a major disaster to both people's lives and properties. The challenge of an accurate hurricane position and intensity forecast comes from a few factors: the lack of observation coverage over the ocean, the difficulties in assimilating satellite radiance data, and the limited ability of model to simulate small scale events like convections (Park and Zou 2004; Xiao et al. 2000; Zou and Xiao 2000). The errors of

hurricane track forecasts have been shown to be promising with a 50% reduction within ten years, while results for the intensity forecasts are still struggling between 5% to 10% (Gall et al. 2012). Therefore, accurate intensity forecasts are particularly difficult. Numerous previous studies argue that the initial vortex for the numerical prediction model to start integration with is essential to hurricane forecasts. Xiao et al. (2000) proposed a bogus data assimilation scheme to initialize hurricane vortices and found that the intensity of the warm core in the initial vortex is a key factor for hurricane intensity prediction. Kurihara et al. (1993) stated that the slow spin-up of a poorly representative initial vortex can make the tropical cyclone intensity forecast out of the question. As the vortices in large-scale analysis are too large, too weak, or misplaced, the vortex initialization requires improvement in order to further improve intensity forecast accuracies (Kurihara et al. 1993; Kurihara et al. 1990; Park and Zou 2004; Thu and Krishnamurti 1992).

Kurihara et al. (1993) proposed to replace the vortex in a large-scale analysis with a specified initial vortex for high-resolution forecast models to integrate from. Both the axisymmetric and asymmetric components of the initial vortex specification details are described. Bender et al. (1993) verified the positive impacts on both the hurricane track and intensity forecasts of the vortex initialization scheme. This scheme represents a major improvement as it alleviates the model adjustment during the early stage and false spinup of the vortex in the model. Kurihara et al. (1995) further revised the scheme by minimizing the analysis region modified, introducing an optimal interpolation technique to determine the environmental fields, and using the axisymmetric version of the forecast model to generate the symmetric component

of the vortex. These revisions helped to preserve the non-hurricane features of the analysis field and further improved the track forecast performance.

The 4D-Var is an elegant way of incorporating observation into model simulations, the bogus data assimilation scheme that Zou and Xiao (2000) proposed can generate a hurricane vortex by fitting the forecast model to a specified bogus surface low based on a few observed and estimated parameters. The satellite water vapor wind data were also assimilated. This scheme greatly improved the intensity forecast accuracy in the case of Hurricane Felix (1995). In Xiao et al. (2000), the sensitivities of forecast results to the assimilated variables were studied. It was found that the track and intensity predictions were sensitive to the size of the specified bogus vortex, where the larger the radius, the weaker the predicted hurricane. It was also indicated that fitting the model to the bogused pressure data reproduced the hurricane structure more efficiently than fitting it to bogused wind data. However, Pu and Braun (2001) found that assimilating wind fields yield better results than assimilating sea level pressures. They suggested that the different sizes of the bogus vortices are likely the cause of this disagreement.

Rotunno and Emanuel (1987) developed a numerical hurricane model (RE model hereafter) to validate the air-sea interaction theory proposed in Emanuel (1986) that a mature storm can be thought of as a simple Carnot engine. The numerical model is nonhydrostatic and axisymmetric with convections explicitly accounted for. In this study, the tangent linear model and adjoint model corresponding to the aforementioned RE model are developed to compose a 4D-Var assimilation model for hurricane vortex initializations. The assimilated variables include liquid water path

(LWP), total precipitable water (TPW) retrieved with AMSR2 observations, and three-dimensional temperature field retrieved with ATMS observations. The impact of these observations on the initialized vortices and the structures of the vortices will be examined.

Chapter 2: Instrument Data Characteristics

2.1 AMSR2 Instrument Characteristics

Table 2.1: AMSR2 Instrument Characteristics

Channel Frequency [GHz]	Band Width [MHz]	Beam Width [deg]	IFOV [km]	NEDT [K]	Sampling Interval [km]	Pol.
6.925	350	1.8	35×62	0.34	10	H/V
7.3	350	1.8	34×58	0.43		
10.65	100	1.2	24×42	0.7		
18.7	200	0.65	14×22	0.7		
23.8	400	0.75	15×26	0.6		
36.5	1000	0.35	7×12	0.7		
89.0	3000	0.15	3×5	1.2	5	

AMSR2 is the only instrument onboard the Global Change Observing Mission—Water satellite, which was successfully launched on May 17, 2012, onto a sun-synchronous orbit at 705-km altitude. It is the successor of the Advanced Microwave Scanning Radiometer—EOS (AMSR-E), which ceased to operate on October 4, 2011. AMSR2 retains the same conical scan feature as AMSR-E with a constant local zenith angle of 55◦. Its swath width is 1450 km. AMSR2 has a total of 14 dual-polarized channels with 7 center frequencies located at 6.925, 7.3, 10.65, 18.7, 23.8, 36.5, and 89.0 GHz. Compared with AMSR-E, the two 7.3-GHz channels are newly added for a more effective detection and mitigation of RFI signals over land. The bandwidth, beamwidth, along-track and across-track sizes of an instantaneous field of view (IFOV), noise equivalent differential temperature (NEDT), and sampling interval are provided in Table 2.1.

Over ocean, the TFI-contaminated channels include those at 10.65 GHz over Europe and 18.7 GHz over North America. Along with the 36.5-GHz channels, the

AMSR2 radiance observations at the 10.65-GHz channels are used for retrieving SSWs (Yan and Weng 2008). Combined with the 6.925-GHz channels, the AMSR2 radiance observations at the 10.65-GHz channels are also used for generating SST products (Yan and Weng 2008). The AMSR2 channels at 18.7 GHz are used for retrieval of both cloud LWP and TPW (Weng and Grody 1994).

2.2 ATMS and AMSU-A Channel Characteristics

Table 2.2 Channel Features of ATMS and AMSU-A

Channel No.		Frequency (GHz)		NEDT (K)		Peak WF (hPa)
ATMS	AMSU	ATMS	AMSU	ATMS	AMSU	
1		23.8		0.5		Window
2		31.4		0.6		Window
3		50.3		0.7		Window
4		51.76		0.5		950
5	4	52.8		0.5	0.25	850
6	5	53.596 ± 0.115		0.5	0.25	700
7	6	54.4		0.5	0.25	400
8	7	54.94		0.5	0.25	250
9	8	55.5		0.5	0.25	200
10	9	57.29		0.75	0.25	100
11	10	57.29 ± 0.217		1	0.4	50
12	11	57.29 ± 0.322 ± 0.048		1	0.4	25
13	12	57.29 ± 0.322 ± 0.022		1.25	0.6	10
14	13	57.29 ± 0.322 ± 0.010		2.2	0.8	5
15	14	57.29 ± 0.322 ± 0.0045		3.6	1.2	2
16	15	88.2	89.0	0.3	0.5	Window
	16		89.0		0.84	Window
17	17	165.5	157.0	0.6	0.84	Window
18	20	183.31 ± 7.0	190.31	0.8	0.6	800
19		183.31 ± 4.5		0.8		700
20	19	183.31 ± 3.0		0.8	0.7	500
21		183.31 ± 1.8		0.8		400
22	18	183.31 ± 1.0		0.9	1.06	300

ATMS is a microwave cross-track scanner with a maximum scan angle of 52.7° with respect to the nadir. It has in total 22 channels with center frequencies

ranging from 23 to 183 GHz. ATMS channels 1–16 are similar to those of AMSU-A designed for sounding atmospheric temperatures, and channels 17–22 are similar to those of MHS for water vapor sounding. ATMS consists of two antennas: one observes radiation at channels below 60 GHz and the other observes radiation at all remaining channels. The beam widths are 5.2° for channels 1–2, 2.2° for channels 3–16, and 1.1° for channels 17–22. A single scan line of ATMS consists of 96 fields of view (FOVs) sampled at an interval of 8/3 s. Details of the channel characteristics of both ATMS and AMSU-A are provided in Table 2.2.

Suomi NPP orbits the Earth 14.1875 times each day in a Sun-synchronous, near-circular, and polar orbit that allows ATMS to observe nearly the entire global atmosphere twice daily. Each orbit ascends across the equator at about 1:30pm local time. A single Suomi NPP orbit takes 101.498min. The repeat cycle is 16 days. Of particular interest to this study are ATMS channels 5–15 whose weighting functions (WFs) shown in Figure 2.1 are evenly distributed in the vertical throughout the troposphere and low stratosphere. The weighting function for a specific channel describes the relative contribution of each atmospheric layer to the measured radiance at this channel's frequency. Also used in this study are the National Center for Environmental Prediction (NCEP) global forecast system (GFS) 6h forecasts, which have a horizontal resolution of 0.3125° × 0.3125°, a total of 64 vertical levels, and a model top located near 0.01 hPa, as well as European Centre for Medium-Range Weather Forecasts (ECMWF) Interim analysis data with a horizontal resolution of 0.25° × 0.25° and 60 vertical levels.

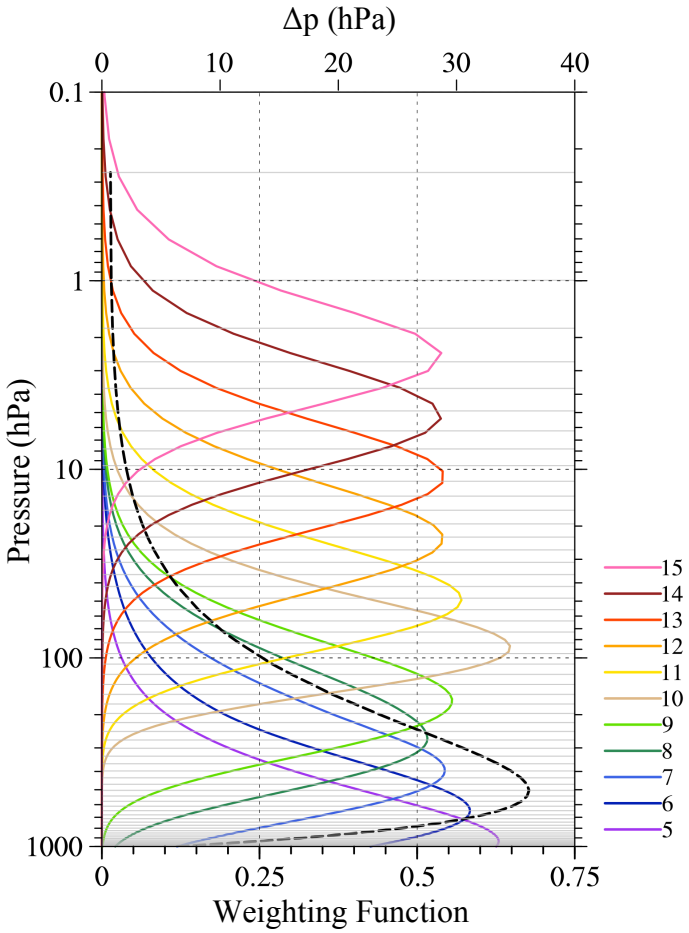

Figure 2.1: Weighting functions of ATMS channels 5–15 (curves in color) and the pressure difference (black dashed curve) between any two neighboring GFS model levels. The 64 GFS model levels are indicated (grey horizontal lines). The weighting functions are calculated using the U.S. standard atmosphere.

Chapter 3: AMSR2 TFI Correction over Ocean and Detection over Land

3.1 TFI Correction Model Description

A. An Empirical Model for TFI Correction over U.S.

TFI is caused by the ocean-reflected TV energy entering AMSR2's antenna. Physically, it is similar to a lunar contamination in ATMS observations caused by the lunar radiation entering into ATMS antenna. Yang and Weng (2016) found that the brightness temperature increment from lunar contamination could be expressed as a function of antenna response function, solid angle of the moon, and the microwave radiance of the moon disk. The solid angle and microwave radiance of the moon disk together determine the amplitude. The antenna response within the mean beam range can be accurately simulated by a one-dimensional Gaussian function (Poisel 2012). An empirical model similar to a lunar correction model developed is developed for TFI correction. It is based on the fact that the antenna response to either the reflected TV energy is in principle the same process as lunar contamination. Over the United States, there are two geostationary TV satellites: DirecTV-11 and the DirecTV-12. DirecTV 12 is located at 102.8˚W and DirecTV 11 at 99.2˚W. The change of the brightness temperature at 18.7 GHz, $\Delta T_{b,18p}^{TFI}$, is

$$\Delta T_{b,18p}^{TFI,phy} = \Omega_{TV11,p} \exp\left(\frac{-\alpha_{TV11}^2}{2\sigma_{TV11}^2}\right) + \Omega_{TV12,p} \exp\left(\frac{-\alpha_{TV12}^2}{2\sigma_{TV12}^2}\right) \tag{3.1}$$

where *p* denotes either vertical or horizontal polarization; $\Omega_{TV11,p}$ and $\Omega_{TV12,p}$ are the background TFI intensity related to TV signal strengths of DirecTV-11 and DirecTV-12 and have the same physical unit as the brightness temperatures, respectively; σ_{TV11}

, and σ_{TV12} are the 3dB beam width of AMSR2 antenna to TV signals from DirecTV-11 and DirecTV-12, respectively, and quantifies the sensitivity of AMSR2 to the signals from a specific TV satellite; and α_{TV11} and α_{TV12} are AMSR2 glint angles with respect to DirecTV-11 and DirecTV-12, respectively, and represent the angle between the reflect TV signal vectors and the AMSR2 Earth scene vector. The unknown parameters $\Omega_{TV11,p}$, $\Omega_{TV12,p}$, α_{TV11} and α_{TV12} in eq. (3.1) are to be determined using AMSR2 data in year 2014.

Since at a fixed location, $\Omega_{TV11,p}$ and $\Omega_{TV12,p}$ are invariant with time. Therefore, the antenna pattern parameters (σ_{TV11}, and σ_{TV12}) can be firstly determined at two fixed locations. TFI occurs at small glint angles. In order to better fit the values of the antenna pattern parameter σ_{TV11} and σ_{TV12}, it is desirable to have enough data at small glint angles. In one hand, the geostationary satellites are fixed in space with respect to the Earth. The spatial distribution of incident angle of a TV satellite does not vary with time. On the other hand, being a conical scanner, AMSR2 has a fixed incident angle 55˚ at the Earth surface. A necessary but not sufficient condition for AMSR2 glint angle to be small is that the AMSR2 pixels are located at a place where the incident angle of geostationary satellite is close to 55˚. Figure 3.1a shows the incident angle field of DirecTV-11 (θ_{TV11}, black curve) and that of DirecTV-12 (θ_{TV12}, purple curve). Data within the grid boxes A and B that are close to the 55˚ incident angle contour lines in a one-year period of 2014 were selected for determining the 3dB beamwidth of AMSR2 antenna to TV signals from DirecTV-11 and DirecTV-12. The TV signal intensity (dBW) of DirecTV-11 and DirecTV-12

over water areas over and around the U.S. are provided in Figure 3.1b-c. These data are obtained from a publically available website[+].

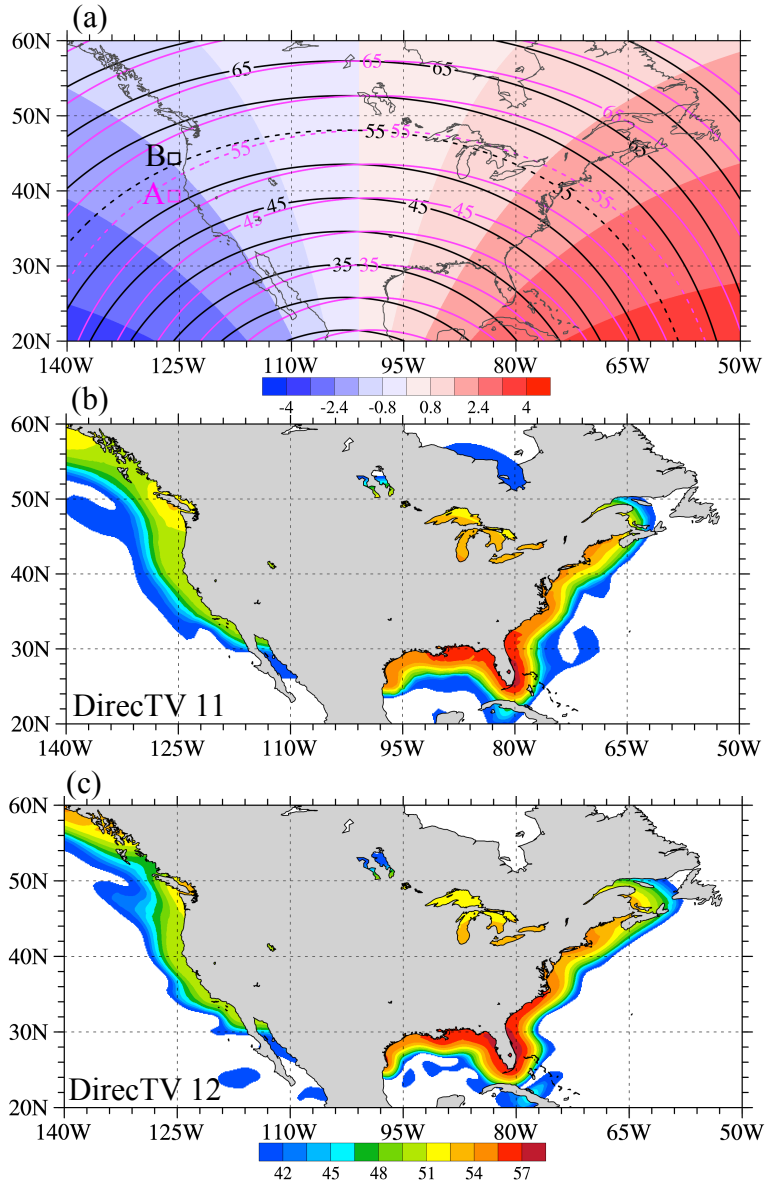

Figure 3.1: (a) Spatial distributions of the incident angles (unit: deg) of DirecTV-11 (θ_{TV11}, black curve) and DirecTV-12 (θ_{TV12}, purple curve) satellites and the differences between the two incident angles ($\theta_{TV12} - \theta_{TV11}$, color shading). (b)-(c) TV signal intensity (unit: dBW) of (b) DirecTV 11 and (c) DirecTV 12. The sizes of grid boxes A and B are [39˚N-40˚N, 126˚W-125˚W] and [44˚N-45˚N, 126˚W-125˚W], respectively.

[+]http://www.satbeams.com/footprints?beam=6219

Due to a close distance between DirecTV-11 and DirecTV-12, differences of AMSR2 glint angle with respect to two TV satellites are less than 5˚. In order to isolate the effect from one satellite from the other satellite as much as possible, a further selection is made to data in grid boxes A and B to satisfy the following requirements: (i) differences of glint angles between DirecTV-11 and DirecTV-12 (i.e., $\alpha_{TV11} - \alpha_{TV12} \le -3.5$) are less than 3.5˚; (ii) sea surface wind speed is less than 6 m s^{-1}; (iii) LWP is less than 0.5 kg m^{-2}, and (iv) glint angles are smaller than 25˚. Once the two datasets are selected, one for DirecTV-11 and the other for DirecTV-12, the change of the brightness temperature at 18.7 GHz, $\Delta T_{b,18p}^{TFI}$, can be written separately for each of the two satellites

$$\Delta T_{b,18p}^{TFI_{TV11},phy} = \Omega_{TV11,18p} \exp\left(-\frac{\alpha_{TV11}^2}{2\sigma_{TV11}^2} \right) \tag{3.2a}$$

$$\Delta T_{b,18p}^{TFI_{TV12},phy} = \Omega_{TV12,18p} \exp\left(-\frac{\alpha_{TV12}^2}{2\sigma_{TV12}^2} \right) \tag{3.2b}$$

Taking a logarithmic operation of eq. (3.2) gives the following relationships among the TFI correction terms, the glint angles and the 3dB beam width of AMSR2 antenna:

$$\ln\left(\Delta T_{b,18p}^{TFI_{TV11},phy}\right) = \ln\left(\Omega_{TV11,18p}\right) - \frac{1}{2\sigma_{TV11}^2}\alpha_{TV11}^2 \tag{3.3a}$$

$$\ln\left(\Delta T_{b,18p}^{TFI_{TV12},phy}\right) = \ln\left(\Omega_{TV12,18p}\right) - \frac{1}{2\sigma_{TV12}^2}\alpha_{TV12}^2 \tag{3.3b}$$

In other words, $\ln\left(\Delta T_{b,18p}^{TFI,TV11}\right)$ is a linear function of the glint angle α_{TV11}^2, and the 3dB beam width of AMSR2 antenna σ_{TV11}^2 is simply the inverse slope of this

linear fitting. The same is true for DirecTV-12. The values of α_{TV11}^2 and α_{TV12}^2 are finally obtained by minimizing the following cost functions

$$J(\sigma_{TV11}^2) = \sum_i \left(\ln\left(\Delta T_{b,18p}^{TFI_{TV11},phy}\right) - \ln\left(\Delta T_{b,18p}^{TFI,reg}\right) \right)_i^2 \quad (3.4a)$$

$$J(\sigma_{TV12}^2) = \sum_i \left(\ln\left(\Delta T_{b,18p}^{TFI_{TV12},phy}\right) - \ln\left(\Delta T_{b,18p}^{TFI,reg}\right) \right)_i^2 \quad (3.4b)$$

where i represents data points, $\Delta T_{b,18p}^{TFI,reg} = T_{b,18p}^{obs} - T_{b,18p}^{reg}$. The $T_{b,18p}^{obs}$ represents the AMSR2 actual observations at 18.7 GHz channels. The $T_{b,18p}^{reg}$ is the TFI-free brightness temperature at 18.7 GHz predicted with sufficient accuracy using observations at other channels (Li et al. 2006). Outliers with $T_{b,18p}^{obs} - T_{b,18p}^{reg} < 3K$ are removed from the linear fitting.

Li et al. (2006) argued that the portion of the natural radiation of a TFI channel, i.e. the TFI-free brightness temperature, can be predicted with sufficient accuracy using observations at other channels due to high channel correlations. Specifically, the TFI-free brightness temperature at 18.7 GHz channels can be predicted according to

$$T_{b,18p}^{reg} = a_0 + \sum_i a_i T_{b,i} + \sum_i b_i T_{b,i}^2 + c_1 \ln\left(290 - T_{b,23v}\right) + c_2 \ln\left(290 - T_{b,23h}\right) \quad (3.5)$$

where the subscript "p" can be either vertical or horizontal polarization. The $T_{b,i}$ include brightness temperature at channels at 6.925, 10.65, and 36.5 GHz of both polarizations. Channels at 18.7, 23.8, and 89.0 GHz are not involved in equation (3.5). The a_i, b_i, and c_i are regression coefficients to be determined. For each month, the observations over the entire globe were collected to train the coefficients, excluding those over land, coastlines, sea ice, and those where TFI glint angles are

smaller than 30˚. Over Europe, a similar regression model is developed to predict the TFI-free brightness temperatures at 10.65 GHz channels, for which the left hand side of eq. (3.5) becomes $T_{b,10p}^{reg}$ and $T_{b,18p}^{reg}$ becomes the predictors in both the second and the third terms on the right hand side of eq. (3.5). The regression coefficients are given in Table 2. The regression errors are unbiased and have and small standard deviations (e.g., ≤ 1.2K) (Li et al. 2006).

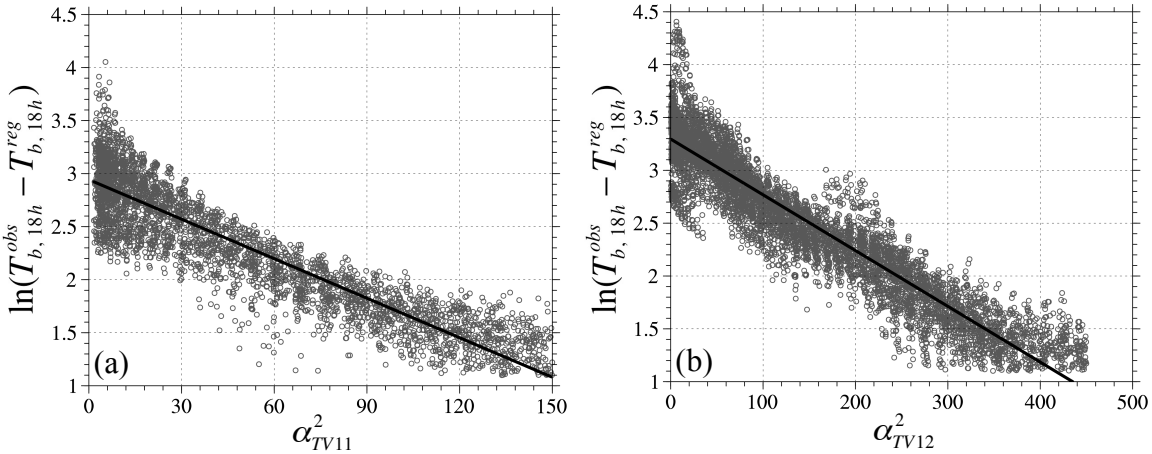

Figure 3.2: Scatter plots of $\ln(T_{b,18h}^{obs} - T_{b,18h}^{reg})$ versus squared glint angle (α^2) with respect to DirecTV-11 (α_{TV11}^2, left panel) and DirecTV-12 (α_{TV11}^2, right panel) for TFI affected data in year 2014 within two 1˚x1˚ boxes (see boxes A and B in Figure 3. 1a) in clear-sky conditions. The linear regression line is also indicated.

Figures 3.2 provides two scatter plots of the natural logarithm of model differences (i.e., $\ln\left(T_{b,18h}^{obs} - T_{b,18h}^{reg}\right)$) versus the squared AMSR2 glint angles α_{TV11}^2 (Figure 3.2a) and α_{TV12}^2 (Figure 3.2b). It is seen that $\ln\left(T_{b,18h}^{obs} - T_{b,18h}^{reg}\right)$ varies linearly with glint angles. The slopes of the regression lines in Figure 3.2 are 1.242×10^{-2} and 0.527×10^{-2}, which give the following values of the 3dB beam width of AMSR2 antenna to TV signals from DirecTV-11 and DirecTV-12: $\sigma_{TV11} = 6.345°$ and

$\sigma_{TV12} = 9.734^{\circ}$. A larger value of the 3dB beam width implies more probable TFI occurrences.

Once the unknown parameters α_{TV11} and α_{TV12} are determined, the background TFI intensity due to TV signals of DirecTV-11 and DirecTV-12, $\Omega_{TV11,18p}$ and $\Omega_{TV12,18p}$, can then be determined using AMSR2 data in year 2014. It is pointed out that both background TFI intensities (i.e., $\Omega_{TV11,18p}$ and $\Omega_{TV12,18p}$) have a linear relationship to $\Delta T_{b,18p}^{TFI_{TV11},phy}$. To obtain a spatial distribution of any of $\Omega_{TV11,18p}$ and $\Omega_{TV12,18p}$, the area over U.S. and its coastal areas, (15˚N-70˚N, 140˚W-50˚W), is divided into 0.25˚×0.25˚ grid boxes. The field of $\Omega_{TV11,18p}$ and $\Omega_{TV12,18p}$ within each grid box can be generated through minimizing the following cost function:

$$J(\Omega_{TV11,18p},\Omega_{TV12,18p}) = \sum_i \left(\Delta T_{b,18p}^{TFI,phy} - \Delta T_{b,18p}^{TFI,reg}\right)_i^2 \tag{3.6}$$

with all TFI affected AMSR2 observations in 2014 in the grid box, where TFI data is defined by $T_{b,18p}^{obs} - T_{b,18p}^{reg} > 3K$. Spatial distributions of data count of TFI pixels within each 0.25˚x0.25˚ grid box for all the data in 2014 and the TFI intensity field for 18.7 GHz channel at horizontal polarization from DirecTV-12 ($\Omega_{TV12,18h}$), which is obtained by minimizing eq. (3.6), is presented in Figure 3.3a and 3.3b, respectively. Figure 3.3b can be compared with Figure 3.1c to find out that the characteristic spatial variations of TFI intensity of $\Omega_{TV12,18h}$ being strongest in the coastal areas of Miami and weaker in the west coast of U.S. (Figure 3.3b) are consistent with those of the TV signal intensity of DirecTV 12 (Figure 3.1c).

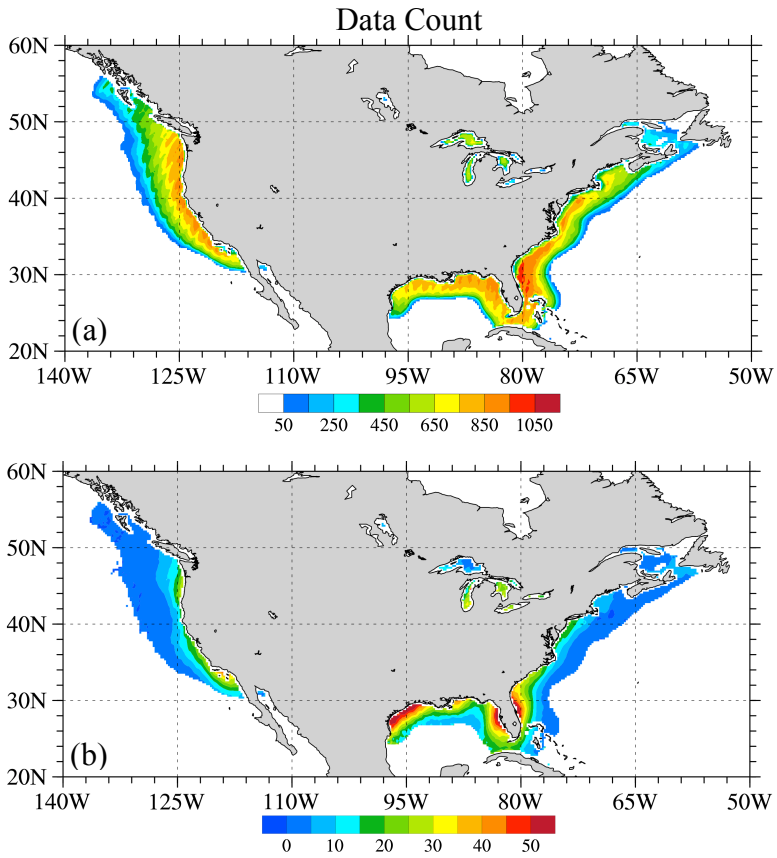

Figure 3.3: Spatial distributions of (a) data count of TFI affected AMSR2 pixels and (b) TFI intensity for 18.7 GHz channel at horizontal polarization from DirecTV-12 ($\Omega_{TV12,18h}$, unit: K) derived from the empirical model for TFI correction.

B. An Empirical Model for TFI Correction over Europe

Around Europe, the AMSR2 dual-polarized X-band channels at 10.65 GHz could have TFI from Hispasat 1E, Eutelsat West 7A, Thor 6, Hot Bird 13B, and Astra 2E satellites (Table 3.1 and Figure 1.1). The spatial distributions of the incident angles of these five European TV satellites are provided in Figure 3.4. At a fixed location, the AMSR2 X-band channels could be interfered with the ocean reflected TV signals from multiple TV satellites varying from one to five and of different strengths. Different TV satellites have different focusing areas. Figure 6 shows the TV signal intensity of Hispasat 1E, Eutelsat West 7A, Thor 6, HotBird 13B, and

Astra 2E. It is seen that Astra 2E transmits signals mainly to a limited area surrounding the United Kingdom, HotBird 13B covers a much broader area of Greater Europe, and the Thor 6 focuses to high latitudes.

Table 3.1: Interfering Geostationary TV Satellites

Longitude	TV Satellites	Focusing Areas	Interfered Channel (GHz)
102.8W	DirecTV-10	North America	18.7
	DirecTV-12	North America	18.7
99.2W	DirecTV-11	North America	18.7
30.0W	Hispasat 1E	South Europe	10.65
7.2W	Eutelsat 7 West A	North Africa	10.65
0.8W	Thor 6	North Europe	10.65
13.0E	Hot Bird 13B	Greater Europe	10.65
	Hot Bird 13C	Greater Europe	10.65
28.2E	Astra 2E	United Kingdom	10.65

The TFI correction model over Europe is similar to that described in section 3.1. When selecting TFI data samples for determining the 3dB beam width parameter (σ) of the five European TV satellites, each TV satellite's focusing area need be taken into consideration. For example, the TFI given rise by Astra 2E will occur in a limited area surrounding the United Kingdom (U.K.). Therefore, considering the distributions of both the incident angles (Figure 3.4) and the TV signal intensities (Figure 3.5a-e), the geographical locations selected for determining the antenna pattern parameter of the five satellites (σ_i, i=1, 2, …, 5) are shown in Figure 3.4. All TFI affected AMSR2 observations in 2014 that fall into each of the five boxes are

extracted to calculate the 3dB beam width parameters. The following values of the 3dB beam width of AMSR2 antenna to TV signals: 5.631 for Hispasat 1E, 6.172 for Eutelsat West 7A, 6.898 for Thor 6, 9.068 for Hot Bird 13B, and 5.308 for Astra 2E.

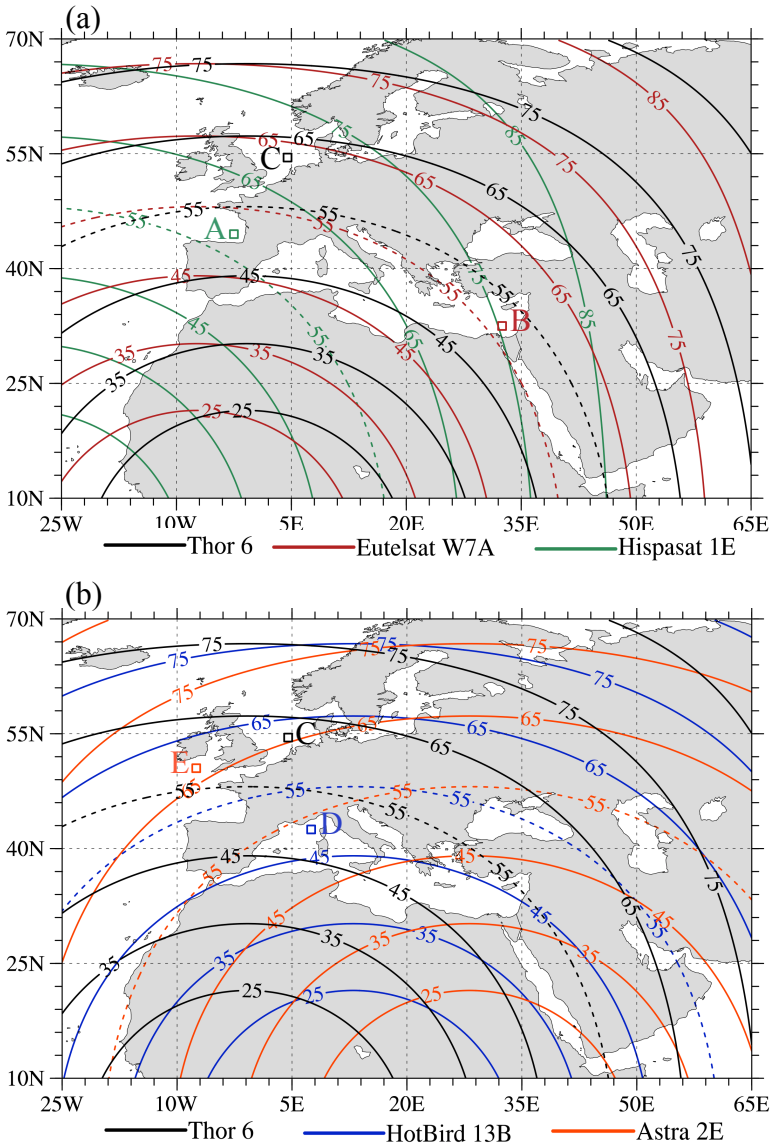

Figure 3.4: Spatial distributions of the incident angles (unit: deg) of (a) Hispasat 1E, Eutelsat West 7A, and Thor 6, and (b) Hot Bird 13B, Astra 2E and Thor 6. The sizes of grid boxes A-E are [44°N-45°N, 3°W-2°W] for Hispasat 1E, [32°N-33°N, 33°E-33°E] for Eutelsat West 7A, [54°N-55°N, 4°E-5°E] for Thor 6, [42°N-43°N, 7°E-8°E] for Hot Bird 13B, and [50°N-51°N, 8°W-7°W] for Astra 2E.

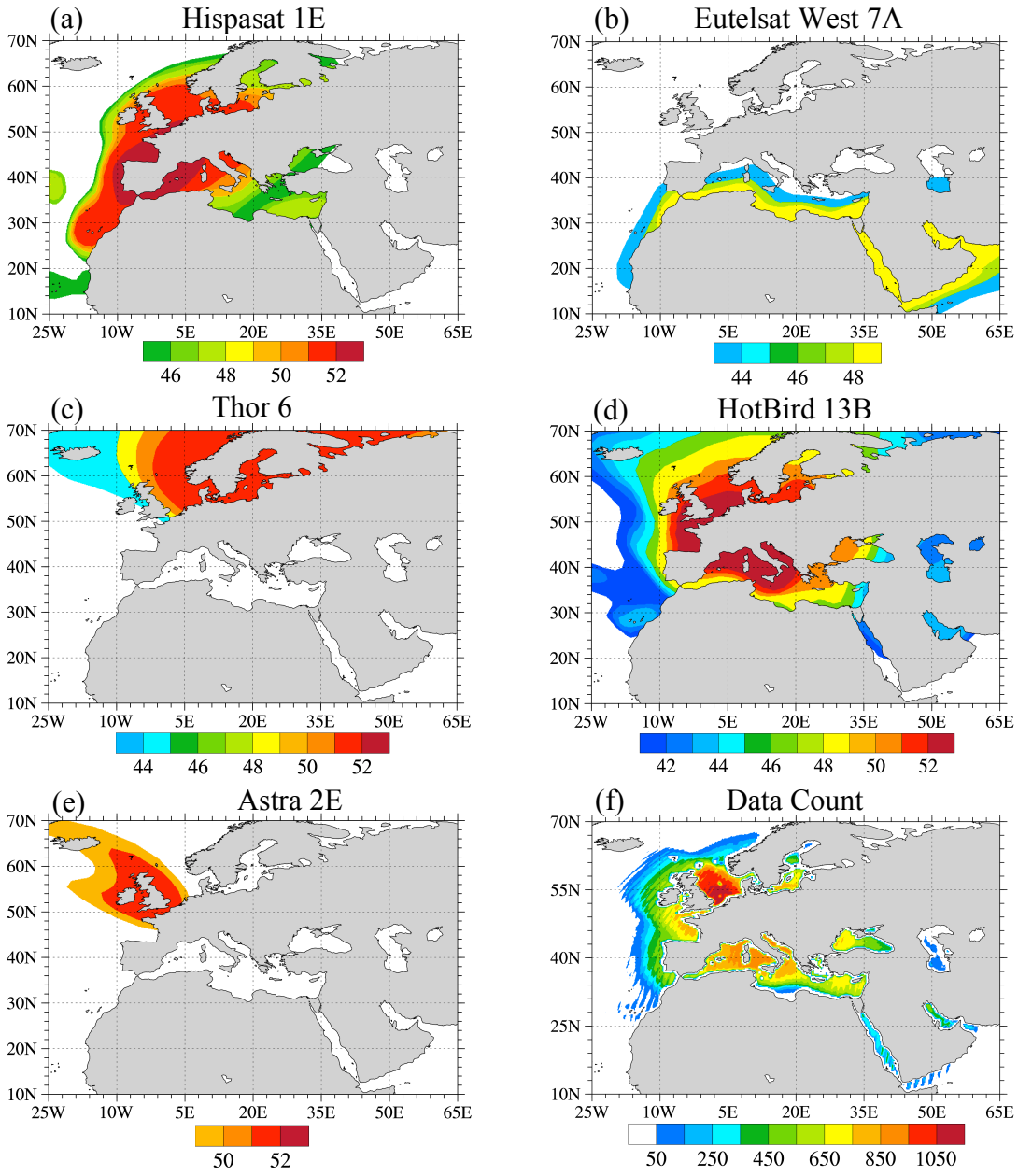

Figure 3.5: (a)-(e) TV signal intensities (unit: dBW) of Hispasat 1E, Eutelsat West 7A, Thor 6, HotBird 13B, and Astra 2E. Spatial distributions of data count of TFI contaminated observations at a 10.65 GHz channel within 0.25˚×0.25˚ grid box in 2014.

Once the AMSR2 antenna's 3dB beam width to reflected TV signals of the five European satellites are obtained, the background TFI intensities ($\Omega_{i,10p}$, i=1, 2, …, 5) can be obtained by minimizing the following cost function:

$$J(\Omega_{1,10p},\Omega_{2,10p},\cdots,\Omega_{5,10p}) = \sum_i \left(\Delta T_{b,10p}^{TFI,phy} - \Delta T_{b,10p}^{TFI,reg}\right)_i^2 \quad (3.7)$$

where *i* represents TFI data points within each 0.25˚×0.25˚ grid box. The total number of TFI affected data in each 0.25˚×0.25˚ grid box during 2014 is shown in Figure 3.5f. It is seen that TFI occurs are most frequently over North Sea area between U.K. and Norway due to the fact that this is an area that are covered with strong TV signals from three different TV satellites: Thor 6, HotBird 13B, and Astra 2E.

3.2 Applications of the Two Empirical Models for AMSR2 TFI Correction

A. Impacts on AMSR2 18.7 GHz over U.S.

The amount of natural radiation in AMSR2 observed brightness temperatures at K-band channels over interfered pixels is concealed by the reflected TV signals. An example is given in Figure 3.6 that shows the AMSR2 observed brightness temperature ($T_{b,18h}^{obs}$, Figure 3.6a), the regression-model predicted brightness temperatures ($T_{b,18h}^{reg}$, Figure 3.6b) of 18.7 GHz channel at horizontal polarization, TFI correction calculated by the empirical model eq. (3.1) ($\Delta T_{b,18h}^{TFI,phy}$, Figure 3.6c), and differences of brightness temperature between AMSR2 observations with TFI correction term incorporated and the regression model simulation ($\left(T_{b,18h}^{obs} - \Delta T_{b,18h}^{TFI,phy}\right) - T_{b,18h}^{reg}$, Figure 3.6d) of the descending node on January 4, 2014. Over an area located at the west coast of U.S. in the east half of the AMSR2 swath and another area located at the west cost of Miami in the west half of the AMSR2 swath, the TFI raises the observed brightness temperatures for more than 30 K. After TFI correction, the differences between AMSR2 observations and regression model

simulations are no more than $\pm 4K$. How much impacts do the TFI correction has on geophysical retrieval products involving 18.7 GHz channels?

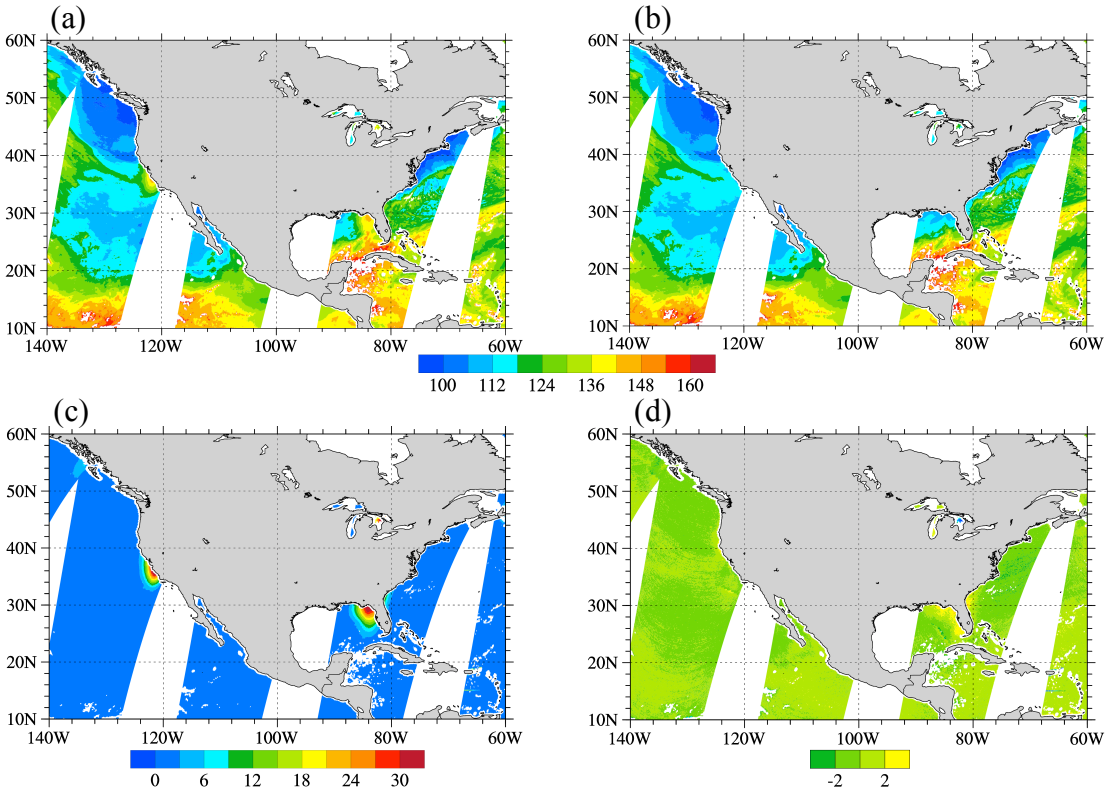

Figure 3.6: (a) AMSR2 observed and (b) regression-model predicted brightness temperatures (unit: K) of 18.7 GHz channel at horizontal polarization. (c) TFI correction (unit: K). (d) Differences of brightness temperature between AMSR2 observations with TFI correction term incorporated and the regression model simulation of 18.7 GHz at horizontal polarization on January 4, 2014.

Liquid water path (LWP) and total precipitable water (TPW) can be retrieved with multiple microwave window channels, so that the absorptions of atmosphere and the emission of the surface can be removed. The LWP and TPW can be retrieved either with brightness temperature observations at 18.7 and 23.8 GHz channels, or with those at 36.5 and 23.8 GHz channels, shown by following equations,

$$LWP_{18} = A_{01}\mu\left[\ln\left(T_s - T_{b,18}\right) - A_{11}\ln\left(T_s - T_{b,23}\right) - A_{21}\right] \tag{3.8a}$$

$$LWP_{36} = A_{02}\mu\left[\ln\left(T_s - T_{b,36}\right) - A_{12}\ln\left(T_s - T_{b,23}\right) - A_{22}\right] \tag{3.8b}$$

$$TPW_{18} = B_{01}\mu\left[\ln\left(T_s - T_{b,18}\right) - B_{11}\ln\left(T_s - T_{b,23}\right) - B_{21}\right] \quad (3.8c)$$

$$TPW_{36} = B_{02}\mu\left[\ln\left(T_s - T_{b,36}\right) - B_{12}\ln\left(T_s - T_{b,23}\right) - B_{22}\right] \quad (3.8d)$$

where A_{ij} and B_{ij} (i=0, 1, 2, i=1, 2) are coefficients and μ is the cosine value of the zenith angle.

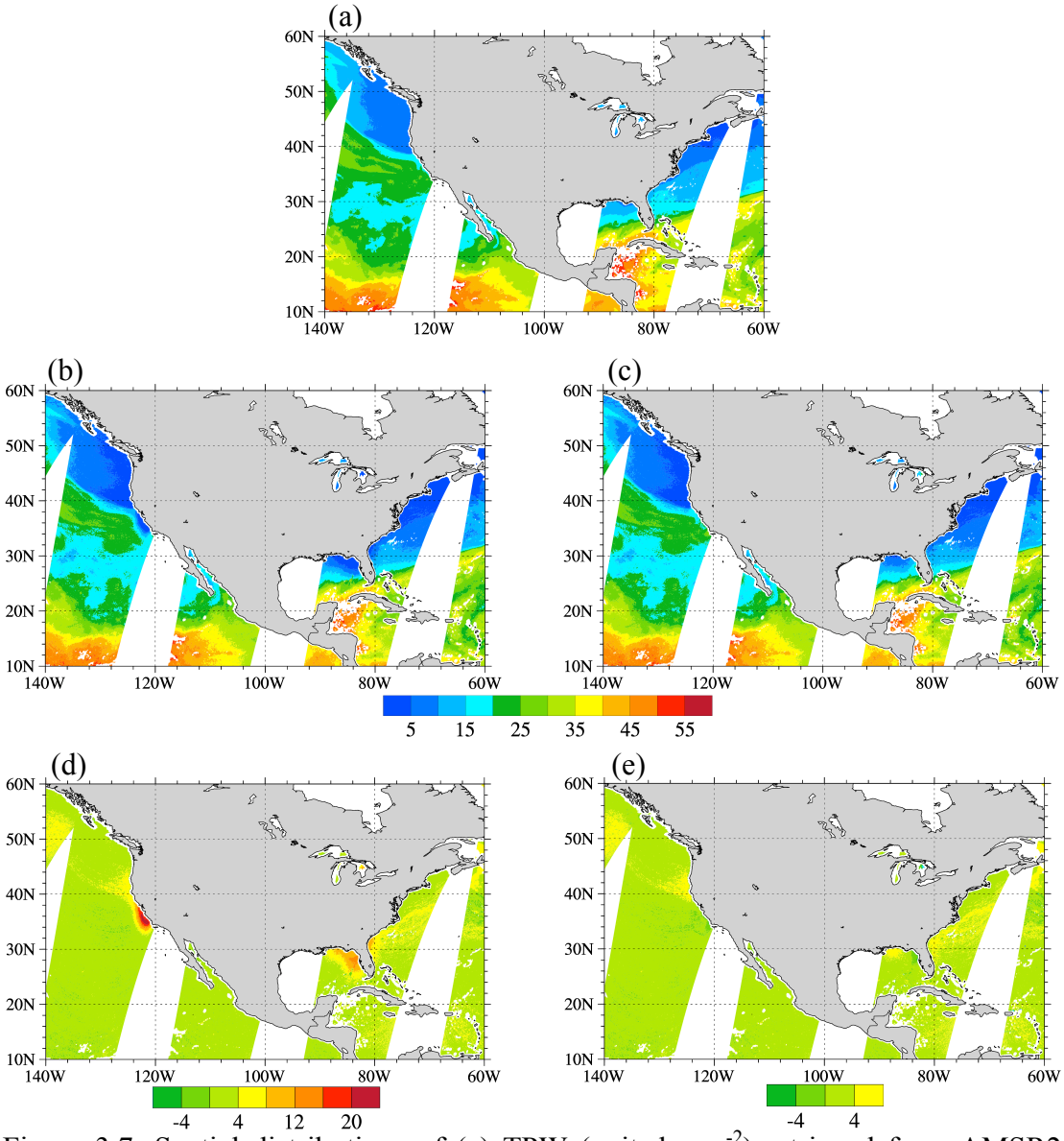

Figure 3.7: Spatial distributions of (a) TPW (unit: kg m^{-2}) retrieved from AMSR2 brightness temperature observations of 36.5 GHz ($TPW_{36.5}$), as well as (b)-(c) TPW retrieved from AMSR2 brightness temperature observations of 18.7 GHz ($TPW_{18.7}$) channels, and (d)-(e) TPW differences between retrievals from the two different frequencies ($TPW_{36.5}$-$TPW_{18.7}$) without (left panels) and with (right panels) TFI correction on January 4, 2014.

At any location, the same geophysical variable retrieved with observations at either frequency channels is expected to have similar variations. However, the 18.7 GHz channels are subject to TFI, and the 36.5 GHz channels are free of TFI. As a consequence, retrieval products of both LWP and TPW from 18.7 GHz channels could have errors in the presence of TFI signals. The impact of TFI correction derived from the empirical model can be evaluated by comparing the same variable retrieved with K-band brightness temperatures before and after the correction with that retrieved from 36.5 GHz channels. Figure 3.7 shows spatial distributions of TPW retrieved from AMSR2 brightness temperature observations at 36.5 GHz ($TPW_{36.5}$, Figure 3.7a), TPW retrieved from AMSR2 brightness temperature observations using 18.7 GHz ($TPW_{18.7}$) channels without (Figure 3.7b) and with (Figure 3.7c) TFI correction, as well as TPW differences ($TPW_{36.5}$-$TPW_{18.7}$) between 36.5 GHz retrieval and 18.7 GHz retrieval without (Figure 3.7d) and with (Figure 3.7e) TFI correction incorporated using the descending data on January 4, 2014. It is seen that over the coastal areas with TFI (Figure 3.6c), the TPW retrieved from 18.7 GHz is more than 20 kg m^{-2} smaller than that with TFI correction or retrieved from TFI free channels at 36.5 GHz (Figure 3.7d). Differences of TPW between 36.5 GHz retrieval and 18.7 GHz retrieval with TFI correction or over areas without TFI are usually less than ±4 kg m^{-2}. Impacts of TFI on LWP retrieval are also significant (Figure 3.8). The TFI signals cause a false amount of LWP for more than 0.5 kg m^{-2}. Differences of LWP between 36.5 GHz retrieval and 18.7 GHz retrieval are usually less than ±4 kg m^{-2} over areas without TFI. Differences of LWP between 36.5 GHz retrieval and

18.7 GHz retrieval with TFI correction or over TFI-free areas are larger over areas with larger LWP.

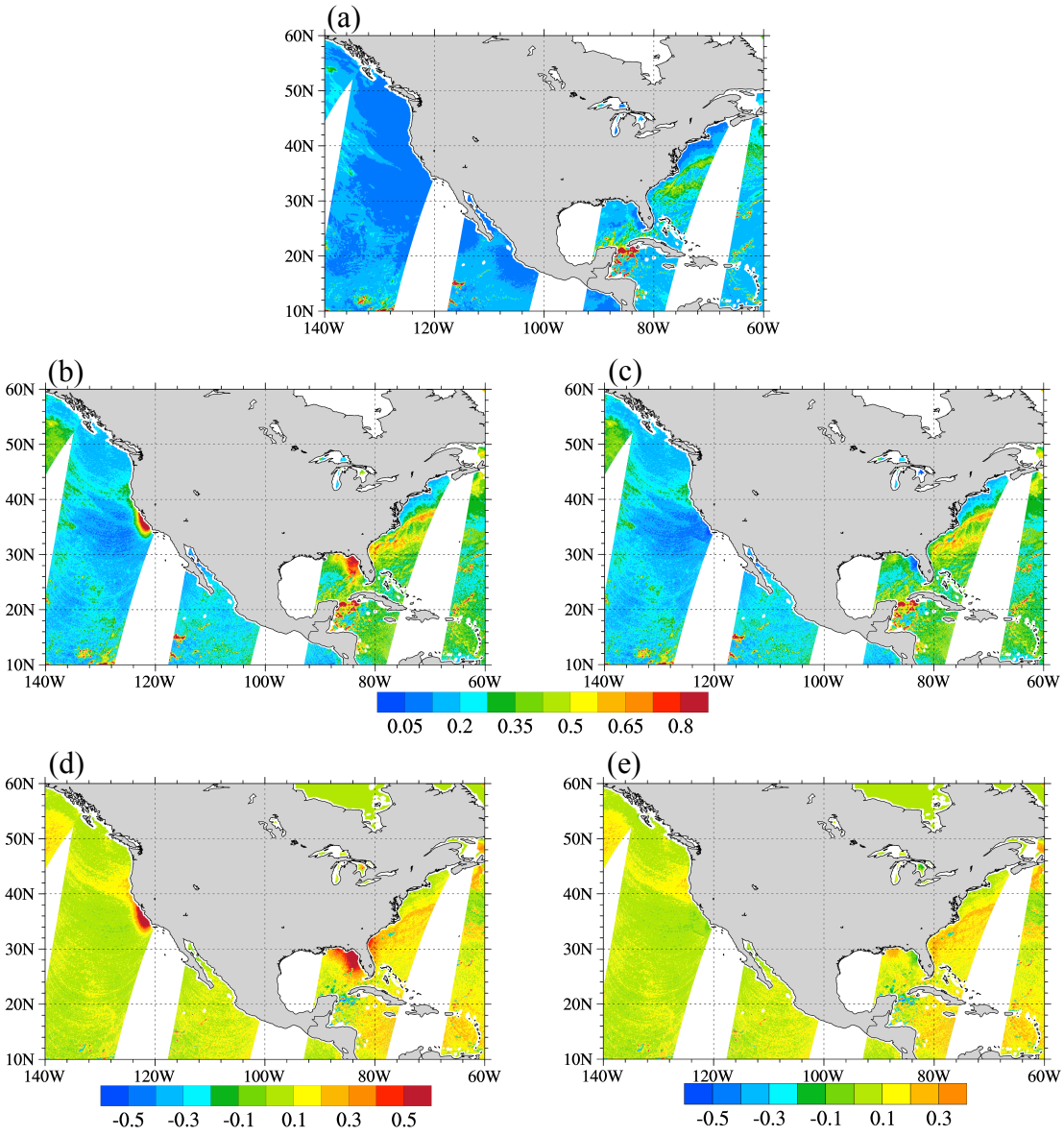

Figure 3.8: Same as Figure 3.7 except for LWP (unit: kg m^{-2}).

Monthly variations of biases calculated from differences between AMSR2 observed and regression-model predicted brightness temperature of the 18.7 GHz channel at horizontal and vertical polarization for all clear-sky data in 2014 with AMSR2 glint angle being less than or equal to 30˚ before and after TFI correction

calculated by the empirical models developed in this study. The percentage number of TFI affected AMSR2 pixels of in each month of 2014 is also given in Figure 3.9. It is seen that there are about 3% of TFI affected data with glint angle $\alpha \le 30^o$. The monthly mean differences between AMSR2 observations without TFI correction and regression-model predicted brightness temperature of the 18.7 GHz channel at horizontal polarization varies from 5.5 to 6.5 K in 2014. After TFI correction, the monthly mean differences of the 18.7 GHz channel at horizontal polarization are significantly reduced in magnitude, with its values varying between -0.25 K and -0.7 K. The TFI introduced biases for the 18.7 GHz channel at vertical polarization are around 1.5 K, which is smaller than at the horizontal polarization. After TFI correction, the monthly biases of the 18.7 GHz channel at vertical polarization are reduced to between -0.1 K and -0.3 K.

As illustrated in Figure 1.1, TFI arising from geostationary satellite TV signals' being picked up by AMSR2 will travel through the entire atmosphere twice. Thus, TFI are subject to atmospheric attenuations. Since the reflection of TV signals occurs at ocean surface, the amount of reflected microwave signals will be influenced by the surface roughness. Under windy circumstances, the ocean surface can become rougher than the calm ocean surface. Figure 3.10 shows the differences between the TFI intensities yielded by the regression method and the modeled TFI intensities with respect to the sea surface winds and total precipitable water. It seems that the TFI model will slightly overestimate the interference intensity when either SSW or TPW are high if the surface roughness and/or atmospheric attenuations are not considered as the case for the current model. The neglect of surface roughness and atmospheric

attenuation might be the reason for the slight negative biases in the monthly mean of differences between TFI intensities from regression method and those from model seen in Figure 3.9.

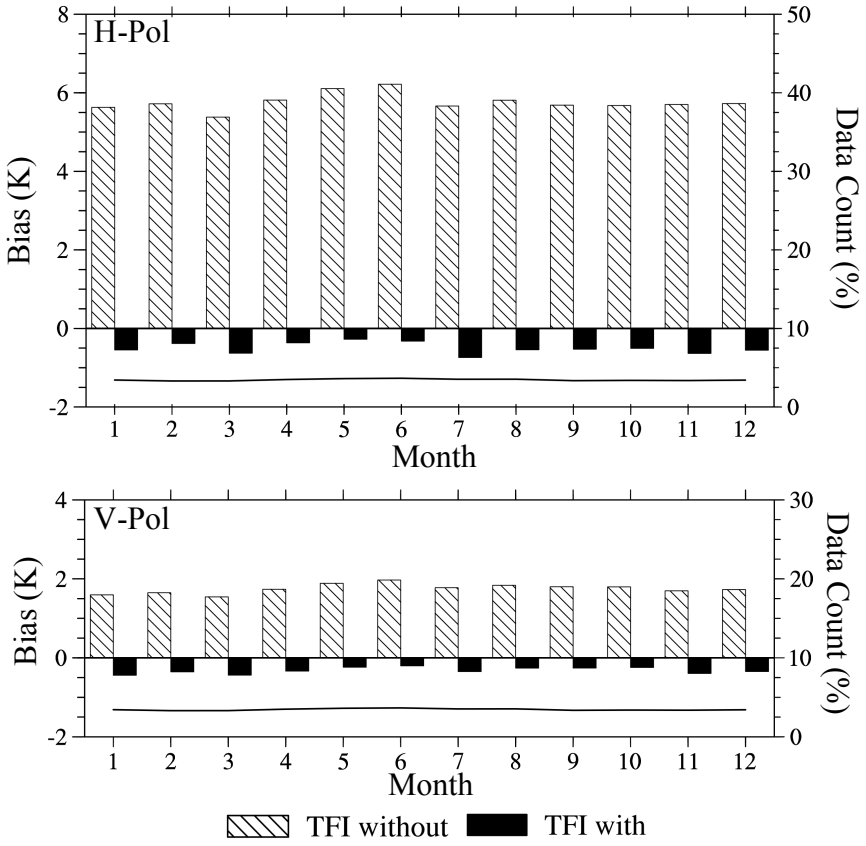

Figure 3.9: Monthly variations of biases (unit: K) calculated from differences between AMSR2 observed and regression-model predicted brightness temperature (unit: K) of the 18.7 GHz channel at horizontal (top panel) and vertical (bottom panel) polarization for global clear-sky data in 2014 with AMSR2 glint angle being less than or equal to 30˚ before (dashed bar) and after (solid bar) TFI correction. The percentage number (unit: %) of TFI-affected AMSR2 pixels in each month of 2014 is indicated by black curve.

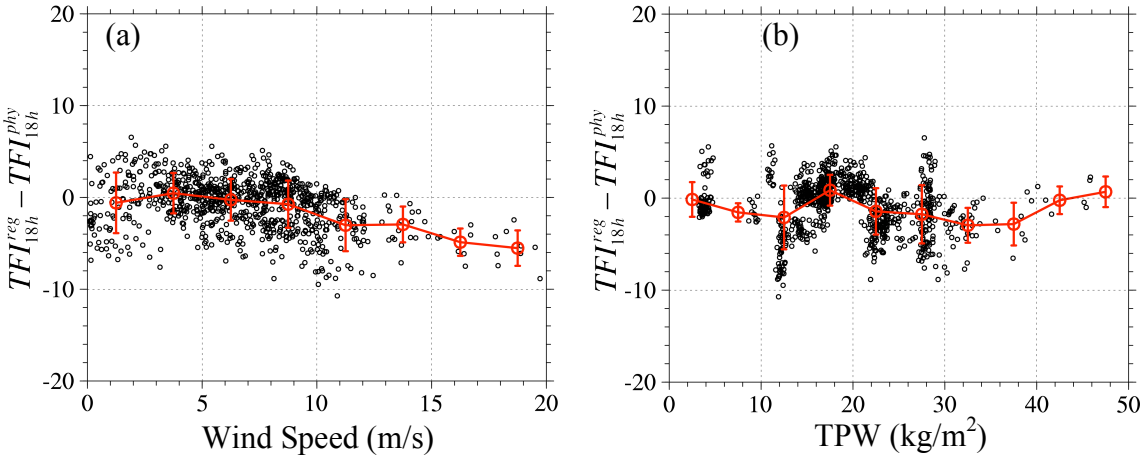

Figure 3.10: Scatter plot of $T_{b,\,18h}^{obs} - T_{b,\,18h}^{reg}$ with respect to the surface wind speed and TPW. Data are selected within the geographical range of [39˚N – 41˚N, 127˚W – 125˚W] in January and February 2014. The glint angles with respect to DirecTV-12 are between 8˚ – 10˚. The red circles and red lines are the mean and error bar at each 2.5 (left panel) and 5 (right panel) interval.

B. Impacts on AMSR2 10.65 GHz over Europe

Over Europe, impacts of TFI correction using the established empirical model on AMSR2 10.65 GHz channels are also significant and positive. As mentioned above, there are five TV satellites that could introduce TFI to these two X-band channels depending on the locations of AMSR2 pixels, TV signal intensities of the five TV satellites (Figure 3.5a-e), and AMSR2 glint angles with respect to the five TV satellites. An example is provided to show AMSR2 glint angles with respect to the five TV satellites over Europe (i.e., Hispasat 1E, Eutelsat West 7A, Thor 6, HotBird 13B, and Astra 2E) for the descending node on March 2, 2014 (Figure 3.11a-e). Due to different geographical locations of the five TV satellite (see Table 3.1), the AMSR2 glint angles with respect to the five TV satellites over Europe are significantly different. With the same AMSR2 observation geometry and the given TV signal intensities of the five TV satellites (Figure 3.5a-e), the TFI correction

calculated from the empirical model (Figure 3.11f) seems to capture the TFI reasonably well. This is further confirmed by a comparison of results of TFI correction calculated from the empirical model in Figure 3.11f with the differences between AMSR2 observations (Figure 3.12a) and the model predicted brightness temperatures using a regression equation for 10.65 GHz channel at horizontal polarization (i.e, similar to eq. (3.5)) (Figure 3.12c) on March 2, 2014.

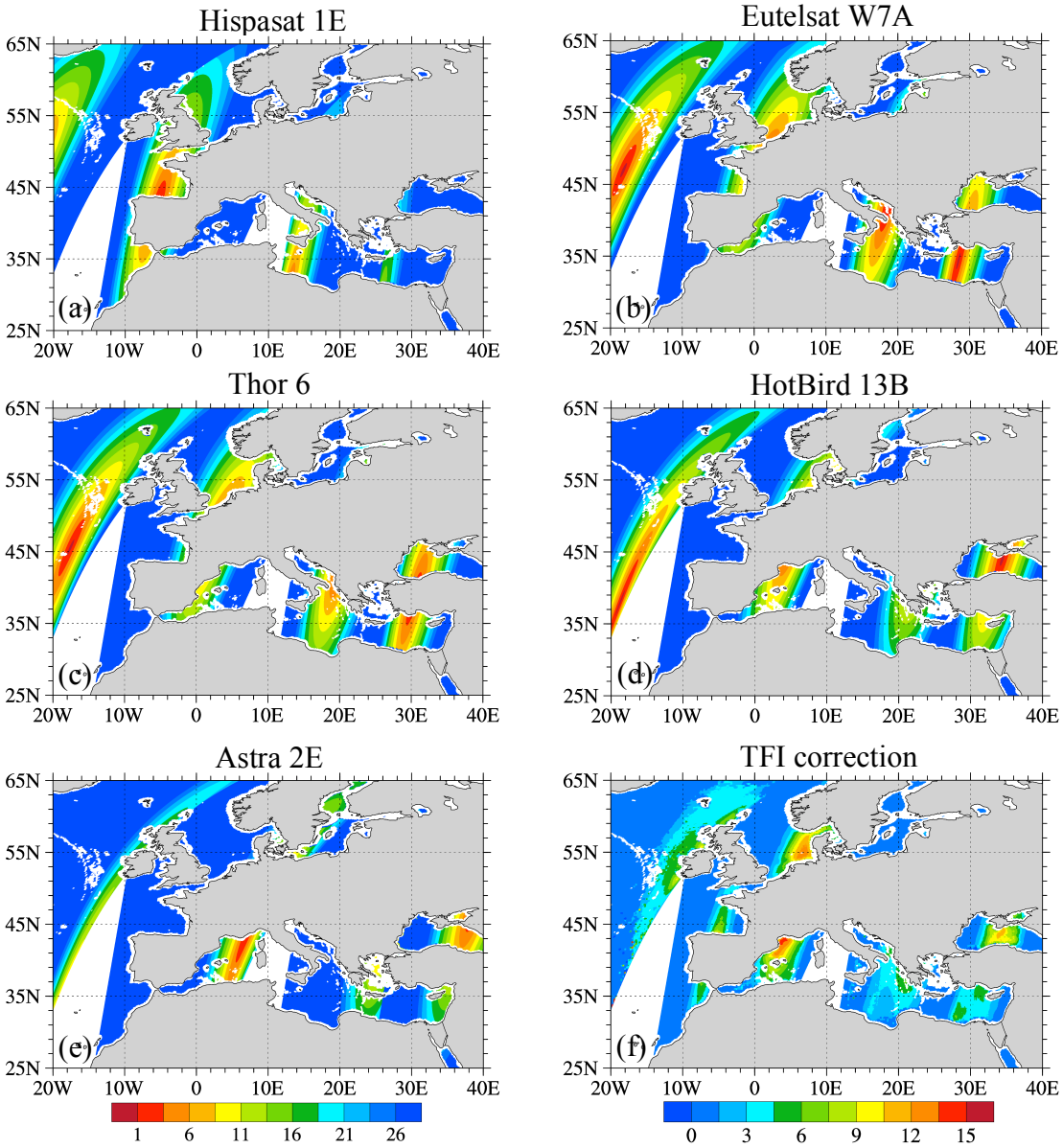

Figure 3.11: (a)-(e) AMSR2 glint angles (unit: deg) with respect to the five TV satellites over Europe (i.e., Hispasat 1E, Eutelsat West 7A, Thor 6, HotBird 13B, and Astra 2E), and (f) TFI correction (unit: K) as a combined TFI impacts from all five European satellites for the descending node on March 2, 2014.

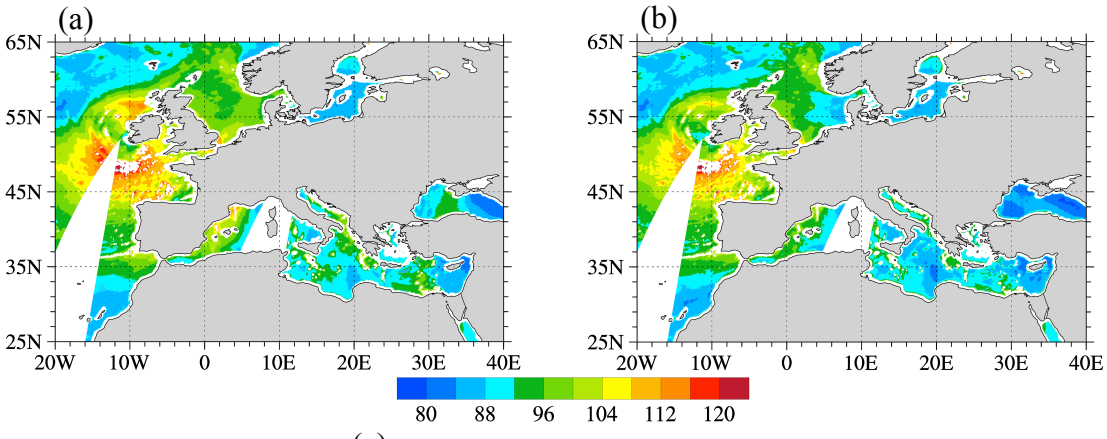

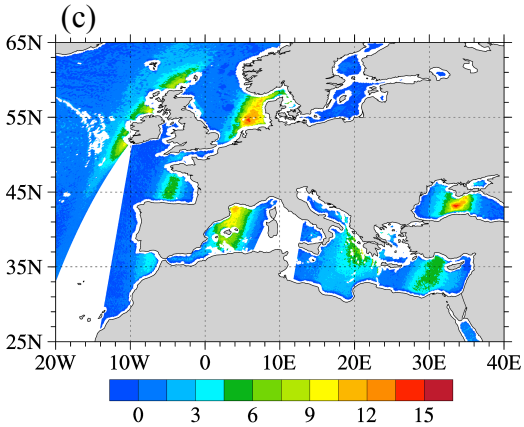

Figure 3.12: (a) AMSR2 observed and (b) regression-model predicted brightness temperatures (unit: K) of 10.65 GHz channel at horizontal polarization on March 2, 2014. (c) Differences between (b) and (a).

A statistical evaluation of an overall performance of the empirical models for TFI correction at X-bands is provided in Figure 3.13. There are about 10% of TFI affected data with glint angle $\alpha \le 30^o$. Similar to results in Figure 3.9 for the K-band channels over U.S., the presence of TFI introduces positive biases to X-band channels over Europe and the remaining biases are negative after TFI correction. The monthly biases are around 2.5 K and 1.2 K for the 10.65 GHz channels at horizontal and

vertical polarization, respectively. After TFI correction, these biases are reduced to about -0.5 K and -0.3 K.

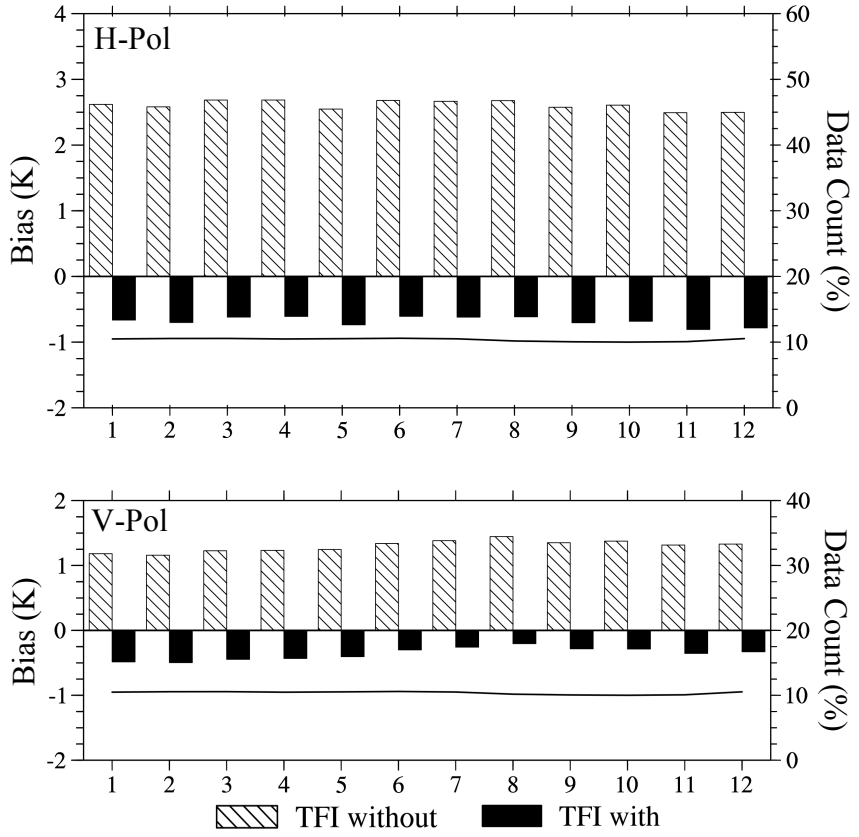

Figure 3.13: Same as Figure 3.9 except at 10.65 GHz channels.

3.3 Detection of TFI over Reflective Land Surface

The United States are fully covered with TV signals at K-band frequencies from both DirecTV-11 at 99.2˚W and DirecTV-12 at 102.8˚W. TV signals could be reflected and interfere with AMSR2 beam cones. Therefore, when AMSR2 is scanning the Earth's atmosphere to measure imager radiances over land in the U.S., it is possible that the TV signals reflected by snow surfaces can enter the antenna, which is similar to TFI over ocean (Tian and Zou 2016; Zou et al. 2014). Figure 3.14

provides a schematic illustration of a potential occurrence of television frequency interference over land. It shows the AMSR2-retrieved snow depth on 5 January 2014, the coverage of DirecTV-12 with its signal intensity indicated (Figure 3.14a), as well as the angle between a reflected TV signal vector (α, Figure 3.14b) and AMSR2's scene vector. It is noticed that the DirecTV-12 signal intensity is strongest near the east coast. The signal intensity distribution from DirecTV-11 is similar to that of DirecTV-12 (Tian and Zou 2016). The symbol α refers to TFI glint angle. The smaller the TFI glint angle is, the more probable it is that the radiance observation can be interfered. Therefore, a small TFI glint angle is a necessary condition for TFI to occur. Besides glint angle, snow can also increase the spectral differences between low and high frequencies. Impacts of snow on radiative emission can only be detected at channels with frequencies greater than 20 GHz, which was the main principle for retrieving snow of reasonable depth. The signal at 36.5 GHz can penetrate a shallow layer of snow. Therefore, a combination of 23.8 and 89.0 GHz channels can be applied to retrieve shallow snow depth in order to avoid the sensitivity of snow retrieval to shallow snow (Kelly 2009; Kelly et al. 2003).

If TV signals are reflected over snow surfaces and enter the antenna of AMSR2, the brightness temperatures at K band channels (18.7 GHz) measured by AMSR2 would be warmer than those from natural radiation, while the brightness temperatures at 23.8 GHz channels are not affected by TFI. Figure 3.15 shows the scatter plot of the same spectral difference with respect to TFI glint angles. It evidently indicates that the spectral difference values are abnormally high only when TFI glint angles are acute enough for the interference to enter AMSR2's antenna.

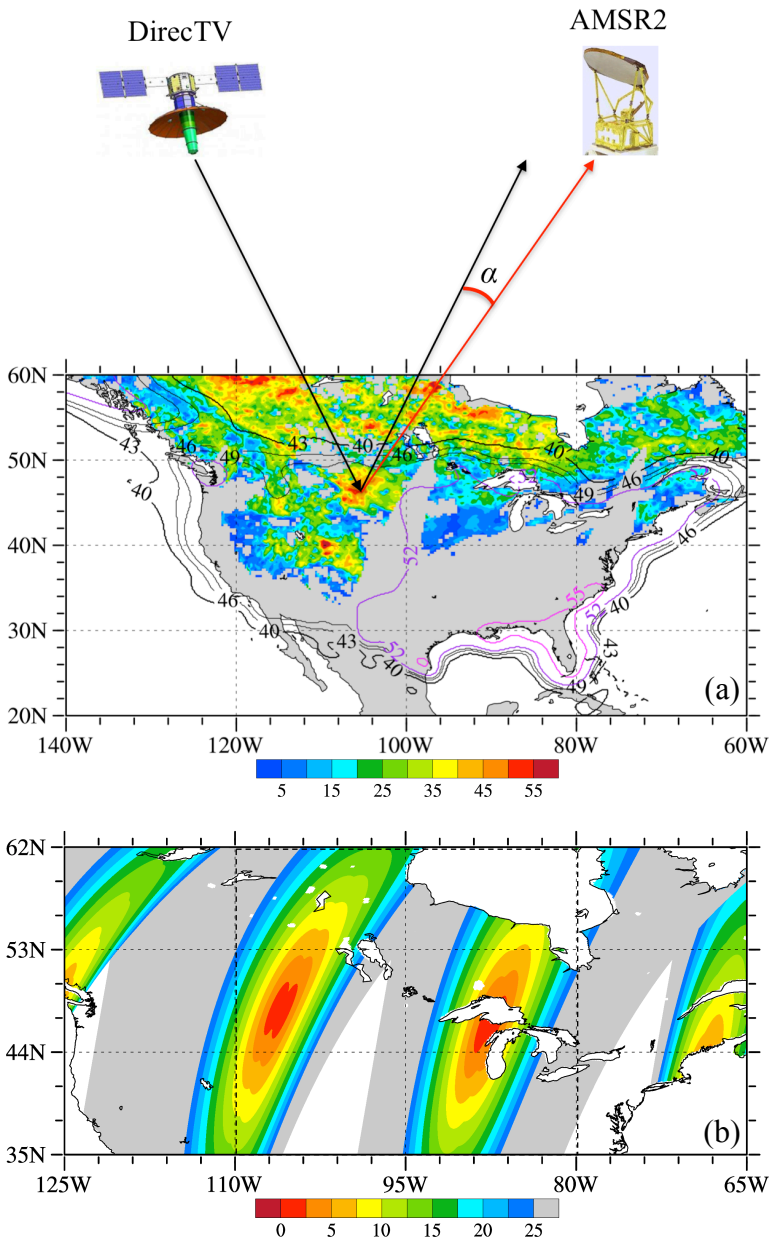

Figure 3.14: (a) A schematic illustration of a potential occurrence of television frequency interference over land, showing the AMSR2-retrieved snow depth (cm, shaded in color) on 5 January 2014, and the coverage of DirecTV-12 with its signal intensity indicated in purple (55 dbW), light purple (52 dbW) and black contours (<52 dbW) at 3 dbW intervals. The symbol α represents the angle between a reflected TV signal vector (upward arrow in black) and AMSR2's scene vector (upward arrow in red). (b) The spatial distribution of α.

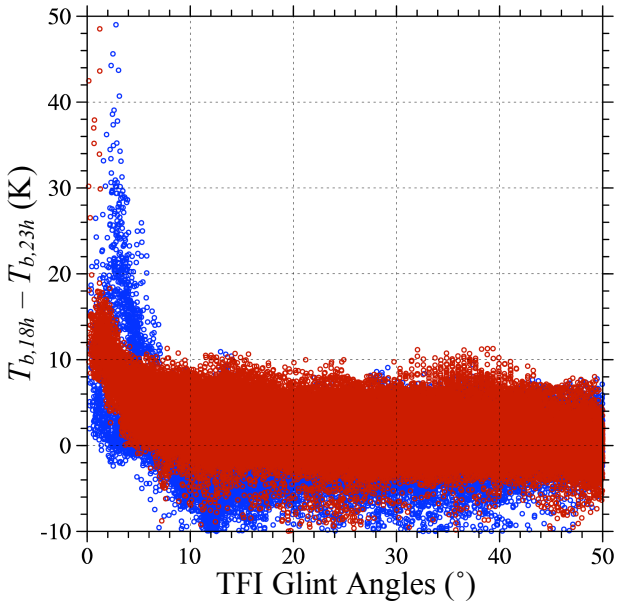

Figure 3.15: Scatter plot of spectral differences distributions of brightness temperatures at horizontal polarizations of 18.7 and 23.8 GHz channels with respect to the TFI glint angles within the range in Figure 3.15 on January 5, 2014. Data from the two swaths in Figure 3.15 are colored in blue (east swath in the box of Figure 3.14b) and red (west swath in the box of Figure 3.14b), respectively.

The geographical distributions of differences of brightness temperature observations at the horizontally polarized state between 18.7 GHz and those of 23.8 GHz on a winter snowing day (January 5) and a summer day (August 17) in 2014 are shown in Figure 3.15. Since this study focus on TFI over land, observations for AMSR2 pixels with land fractions being less than 90% are excluded in Figure 3.16 in order to avoid lake effects on spectral differences, which can be significant in summer. The AMSR2 on these two days have the same swath distributions since the AMSR2's swath repeating time is 16 days. The TFI glint angle fields with respect to the geostationary TV satellites are also the same on January 5 and August 17, 2014. In Figure 3.15a, the two largest spectral differences of brightness temperature observations between 18.7 GHz and those of 23.8 GHz are found west of Lake

Michigan and the great plains of the U.S., where the TFI glint angles are small. These two areas are populated with snow (see Figure 3.14a).

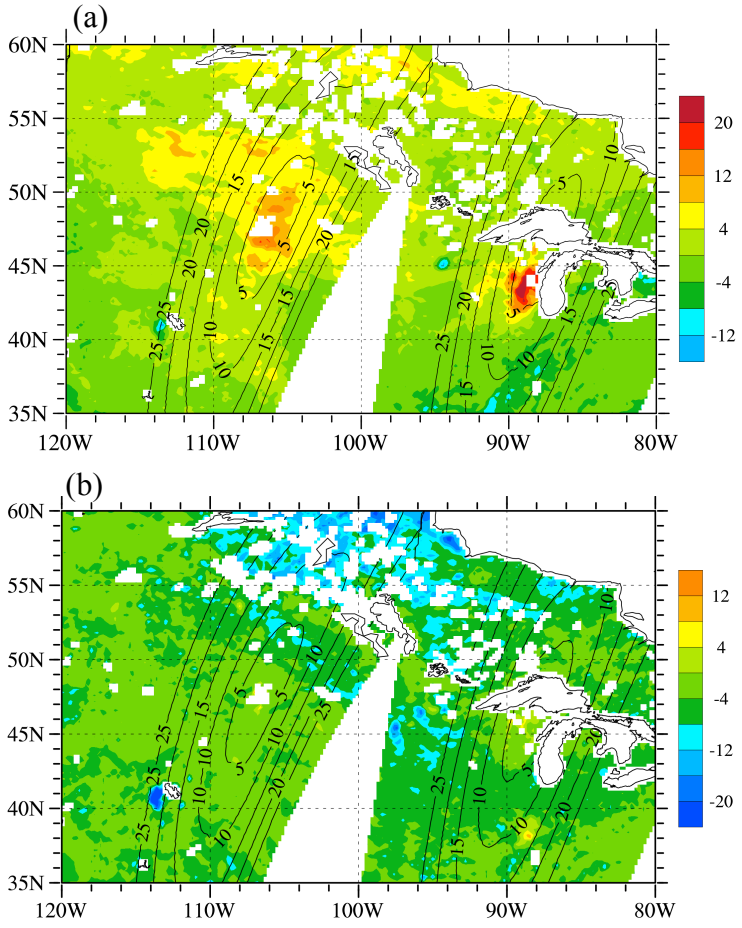

Figure 3.16: Spectral differences (K) distributions of brightness temperatures at horizontal polarizations between 18.7 and 23.8 GHz channels (18.7 minus 23.8, shaded in color) and TFI glint angles (contoured for values less than 25˚) on (a) 5 January and (b) 17 August 2014. Observations for AMSR2 pixels with land fractions being less than 90% are excluded to avoid lake effects on spectral differences.

However, such large spectral differences of brightness temperature observations between 18.7 GHz and those of 23.8 GHz are not found west of Lake Michigan and the great plains of the U.S. in summer (Figure 3.15b) although the TFI glint angles are also small. It can thus be inferred that the K-band observations with snow

coverage on January 5, 2014 could be TFI-contaminated in the above-mentioned two areas. Compared with snow depth distribution shown in Figure 3.14a, it seems that the spectral differences between 18.7 GHz and 23.8 GHz are positive and large over areas with large snow depth, which is expected due to larger scattering effects of snow at higher frequencies. However, the area characterized by the largest spectral differences between 18.7 GHz and 23.8 GHz west of Lake Michigan has small snow depth. In other words, the TFI occurrence would increase the brightness temperatures of 18.7 GHz channels and snow scattering would decrease the brightness temperatures at 23.8 GHz more significantly than 18.7 GHz channels. Both TFI occurrence and snow reflection could increase the spectral differences between 18.7 GHz and those of 23.8 GHz channels. It is thus difficult to distinguish the effects of snow from the effects of TFI by simply examining the spectral differences between two different frequencies.

In order to isolate TFI from natural radiation over land with snow coverage, a spectral difference index vector, $Index_{TFI-18H}$, is firstly defined for detecting TFI at 18.7 GHz at horizontal polarization. It consists of five spectral differences as its components

$$Index_{TFI-18H} = \begin{pmatrix} T_{b,18H} - T_{b,23H} \\ T_{b,10H} - T_{b,36\mathrm{H}} \\ T_{b,10V} - T_{b,36\mathrm{V}} \\ T_{b,23H} - T_{b,89\mathrm{H}} \\ T_{b,23\mathrm{V}} - T_{b,89\mathrm{V}} \end{pmatrix}_{5x1} \tag{3.9}$$

where $Index_{\mathrm{TFI\text{-}18H}}$ denotes the spectral difference index vector for 18.7 GHz H-Pol channel. All five components of the vector $Index_{\mathrm{TFI\text{-}18H}}$ are related to earth surface

type information, such as snow, but TFI only exists in the first component of the vector. A data matrix is constructed from $Index_{\text{TFI-18H}}$ as follows

$$\mathbf{A}_{5\times N} = \begin{pmatrix} Index_{18H,1} & Index_{18H,2} & \cdots & Index_{18H,N} \end{pmatrix}_{5xN} \tag{3.10}$$

where N is the total number of observation pixels over land with TFI glint angles less than 25˚. The TFI glint angle threshold is set to 25˚ to ensure that all interfered observations are included (see Figure 3.15). The covariance matrix $\mathbf{R}_{5\times 5}$ can be given by $\mathbf{R}_{5\times 5} = \mathbf{A}\mathbf{A}^T$. The eigenvalues and eigenvectors of the covariance matrix can then be obtained by solving the following equation,

$$\mathbf{R}\mathbf{e}_i = \lambda_i \mathbf{e}_i \tag{3.11}$$

where λ_i is the i^{th} eigenvalue and $\mathbf{e}_i = [e_{1,i}, e_{2,i}, \cdots, e_{5,i}]$ is the i^{th} PC mode of $\mathbf{R}_{5\times 5}$. The i^{th} eigenvalue λ_i quantifies the i^{th} greatest variance contribution of the ith PC mode in the total variance of the data matrix **A**. A set of PC coefficients, $\mathbf{u}_i$, can be derived by projecting the original data matrix **A** onto the orthogonal space spanned by the eigenvectors $\mathbf{e}_i$:

$$\begin{pmatrix} \mathbf{u}_1 \\ \mathbf{u}_2 \\ \vdots \\ \mathbf{u}_5 \end{pmatrix} = \mathbf{E}^T\mathbf{A} \tag{3.12}$$

The original data matrix defined in eq. (3.11) can be exactly reconstructed with the PC coefficients and PC modes:

$$\mathbf{A} = \sum_{i=1}^{5} \mathbf{A}_i, \text{ where } \mathbf{A}_i = \mathbf{e}_i\mathbf{u}_i \tag{3.13}$$

in eq. (3.13) where $\mathbf{A}_i$ is the i^{th} component accounting for the i^{th} greatest variance in the original data matrix. Figure 3.17 gives the eigenvectors yielded in the PCA for the data matrix composed with vectors defined in eq. (3.9). It is noticed that the first component of the fifth eigenvector, i.e., $TI_{18H}^{\mathbf{A}_5} = \left(T_{b,\,18H} - T_{b,\,23H}\right)^{\mathbf{A}_5}$, has the greatest value, reflecting a presence of TFI in the first component of the fifth eigenvector. Therefore, a new TFI intensity index over land with snow coverage is finally defined as

$$I_{TFI-18H,snow} = \left(T_{b,18H} - T_{b,23H}\right)^{\mathbf{A}_5} \tag{3.14}$$

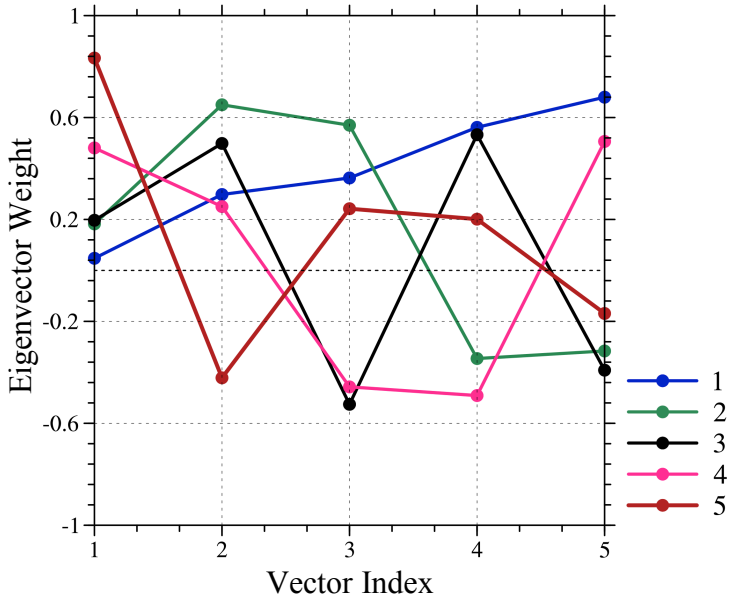

Figure 3.17: The five PC modes (or eigenvectors) calculated in the principal component analysis of spectral differences distributions of brightness temperatures at horizontal polarizations of 18.7 and 23.8 GHz channels for the swath passing through 110˚W in Figure 3.15a.

3.4 Numerical Results

The spatial distribution of $I_{TFI-18H,snow}$ for the AMSR2 observations in a typical snowing winter day is shown in Figure 3.18. The large values of $I_{TFI-18H,snow}$ are found only over areas west of Lake Michigan and the great plain with snow coverage and small TFI glint angles. Other areas with large spectral differences of brightness temperatures between 18.7 GHz and those of 23.8 GHz seen in Figure 3.16 are characterized with low TFI intensities. The TFI affected AMSR2 observations over snow surfaces are identified by the glint-angle constrained PCA algorithm.

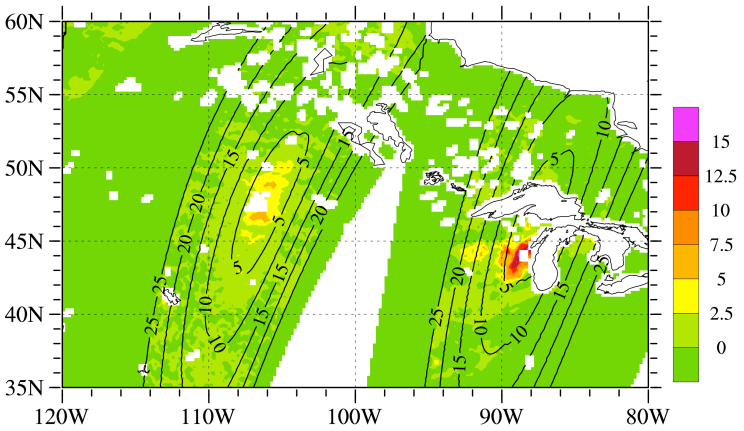

Figure 3.18: TFI signal intensity (K) detected with PCA method and TFI glint angles (contoured for values less than 25˚) on 5 January 2014.

The TFI glint angles are determined by both the differences of zenith and azimuth angles between the reflected TV signal vectors from the geostationary satellite and the Earth scene vectors of AMSR2. AMSR2 is a conical scanner with a fixed local incident angle of 55˚. The angles of reflected TV signals are the same as those of the TV signals from DirecTV satellites. While the TV signal sources, i.e., the geostationary DirecTV satellites, are fixed with respect to the Earth, the incident angles for TV signals vary with respect to geographical locations. Only when the

incident angles of TV signal vectors are close to 55˚ degrees, the TFI glint angles approach zero. The TFI of AMSR2 observations would most likely take place when TFI glint angles approach zero. To confirm this, we show in Figure 3.19 a monthly distribution of the maximum TFI intensity during in January 2014. The 55˚ incident angle of TV signals from DirecTV-11 and DirecTV-12 are indicated by dashed and solid black curves, respectively. Within the one-month period, TFI over land by snow reflection is found in a latitudinal band following the two 55˚ incident angle lines of DirecTV-11 and Direct-12, extending from west to east coasts. The largest TFI is found over the east coast, where the intensity of TV signals is strongest (see Figure 3.14a).

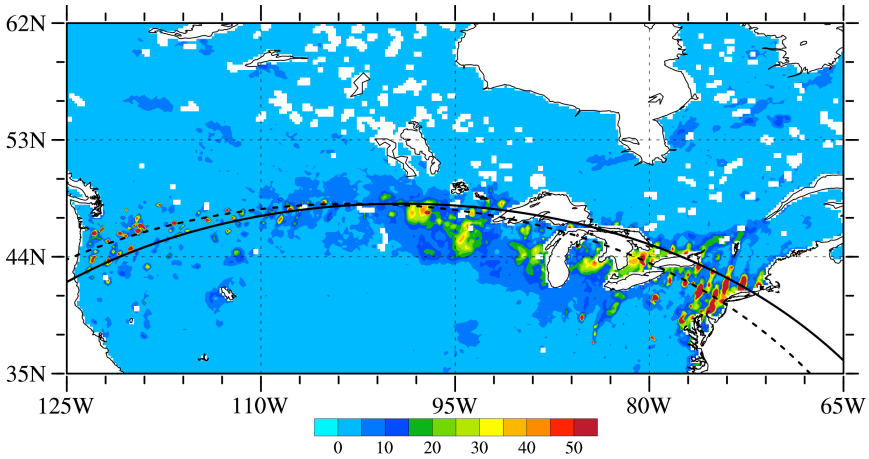

Figure 3.19: The maximum TFI intensity (K) distribution in 1˚x1˚ grid boxes for all the data in January of 2014 (shaded). The 55˚ incident angle lines of DirecTV-11 and Direct-12 are indicated by the dashed and solid black curves, respectively.

Chapter 4: ATMS and AMSU-A Derived Hurricane Warm Cores

4.1 A Description of Temperature Retrieval Algorithm

The atmospheric temperature at a given pressure level can be expressed as a linear combination of brightness temperatures of ATMS temperature sounding channels (Zhu and Weng 2013; Zhu et al. 2002):

$$T(p) = C_0(p) + \sum_{i=5}^{15} C_i(p) T_b(v_i) + C_{sz}(p) \frac{1}{\cos(\theta)} \tag{4.1}$$

where p is pressure level, θ is the sensor zenith angle (i.e. the angle between the earth view beam and the local normal direction), v_i is the ATMS channel frequency of the i^{th} channel (i=5, 6, …, 15), T_b are the brightness temperatures observed by ATMS, and C_0, C_i and C_{sz} are regression coefficients.

In order to obtain the regression coefficients, the ATMS observations over ocean during the period of two weeks prior to Hurricane Sandy, i.e., from 8 to 21 October 2012 are used as a training data set. NCEP GFS atmospheric temperature fields are available at four times, i.e., 0000 UTC, 0600 UTC, 1200 UTC, and 1800 UTC on each day. A global distribution of the total number of ATMS observations collocated with GFS analysis within 0.5°×0.5° grid boxes and ± 1 h during the time period from 8 to 21 October 2012 is provided in Figure 4.1a.

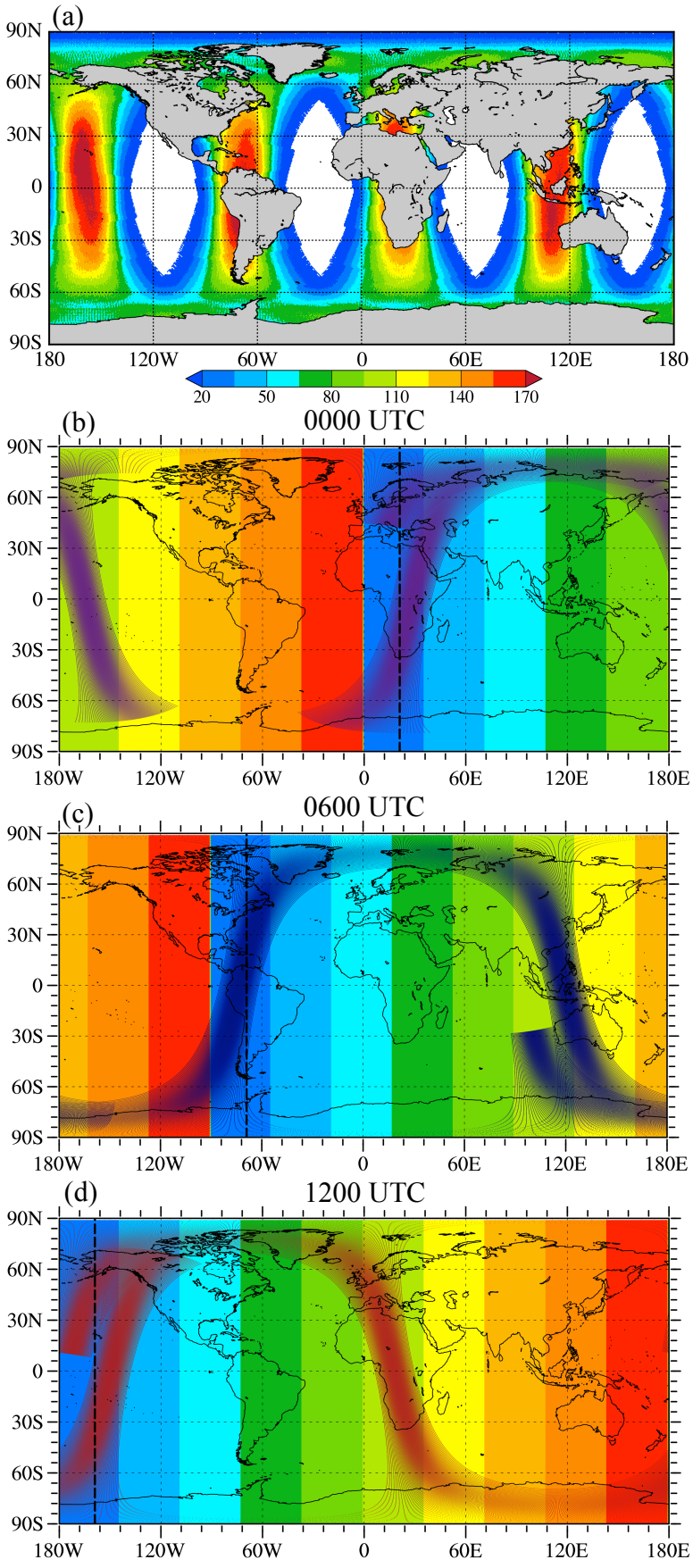
(a)
90N
60N
30N
0
30S
60S
90S
180
120W
60W
0
60E
120E
180
20
50
80
110
140
170
(b)
0000 UTC
90N
60N
30N
0
30S
60S
90S
180W
120W
60W
0
60E
120E
180E
(c)
0600 UTC
90N
60N
30N
0
30S
60S
90S
180W
120W
60W
0
60E
120E
180E
(d)
1200 UTC
90N
60N
30N
0
30S
60S
90S
180W
120W
60W
0
60E
120E
180E

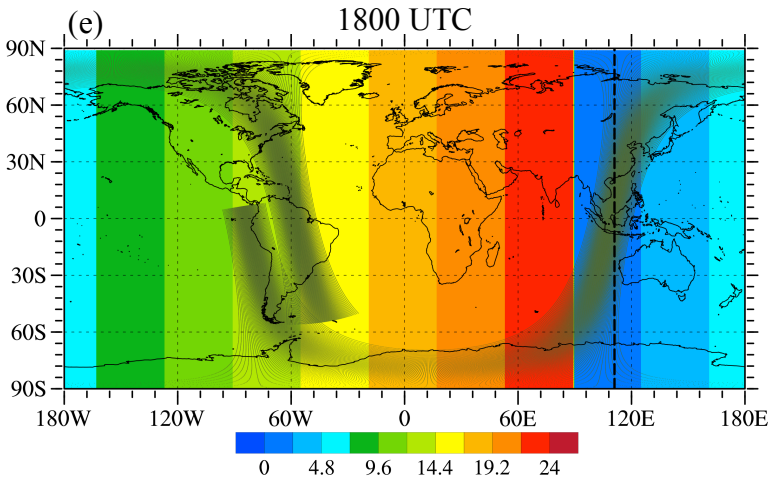

Figure 4.1: (a) Global distribution of the total number of ATMS observations collocated with GFS analysis within 0.5° × 0.5° grid boxes and ±1 h during the time period from 8 to 21 August 2012. ATMS orbits within (b) 0000 ±1 h UTC, (c) 0600±1 h UTC, (d) 1200 ±1 h UTC, and (e) 1800 ±1 h UTC, respectively, on 24 October 2012. The meridional dashed line marks the longitude where the local time is 13:30. The color shadings are the global distribution of local time at each UTC time.

In equation (4.1), the regression coefficients C_0 and C_i are independent of scan angle, and the last term is included to characterize the scan angle dependent feature in ATMS observations at temperature sounding channels. However, this last term alone is probably not sufficient for accounting for all the dependencies on zenith angles, causing the retrieved atmospheric temperatures to have scan biases. All observations on the same position of their scan lines, however, are independent from their zenith angles. Therefore, in order to better accommodate the scan dependence, the coefficient training and the temperature retrieval are performed separately at each scan angle instead of once using data from all scan angles. Accordingly, the zenith angle term in equation (4.1) is removed, while all other terms becomes functions of scan positions or scan angles. It is also pointed out that observations of all sounding channels 5-15 are included to retrieve atmospheric temperatures at any pressure level. However, the temperatures at a specific pressure level may be correlated to some

channels but not all channels. Including those uncorrelated channels could do more damage than help to the retrieval of temperatures at that pressure level. A modified temperature retrieval algorithm is thus proposed that employs the following equation

$$T(p,\theta) = C_0(p,\theta) + \sum_{i=i_{1,p}}^{i_{2,p}} C_i(p,\theta) T_b(v_i,\theta) \tag{4.2}$$

where $i_{1,p}$, …, $i_{2,p}$ are a subset of ATMS channels 5-15 that are correlated with the temperature at the pressure level p. This algorithm is simpler and computationally more efficient than the one-dimensional variational algorithm called Microwave Integrated Retrieval System (MIRS) (Boukabara et al. 2011). MIRS is used operationally at NOAA to provide its products to the user community in real-time and from the archive.

At a given channel, the brightness temperatures do not respond to temperatures at all pressure levels. Figure 4.2 shows the relationship between ATMS brightness temperatures at channel 6 and GFS temperatures at 500 hPa (Figure 4.2a) and 30 hPa (Figure 4.2b) as well as the relationship between ATMS brightness temperatures at channel 10 and GFS temperatures at 100 hPa (Figure 4.2c) and 10 hPa (Figure 4.2d) for all collocated data from August 10 to October 31, 2012. ATMS channel 6 is a lower tropospheric sounding channel with its peak WF located at 700 hPa and channel 10 is a stratospheric sounding channel with its peak WF located at 100 hPa. As can be expected, the atmospheric temperatures at 500 hPa (100 hPa) are highly correlated with the ATMS brightness temperatures at channel 6 (channel 10). In contrast, the atmospheric temperatures at 30 hPa (10 hPa) are not correlated with the ATMS brightness temperatures at channel 6 (channel 10) at all. The correlations

and R^2 values for a linear regression between the GFS temperatures and brightness temperatures for (a) are 0.9623 and 92.6%; for (b) are -0.3518 and 12.3%; for (c) are 0.9702 and 94.1%; and for (d) are -0.2721 and 7.41%.

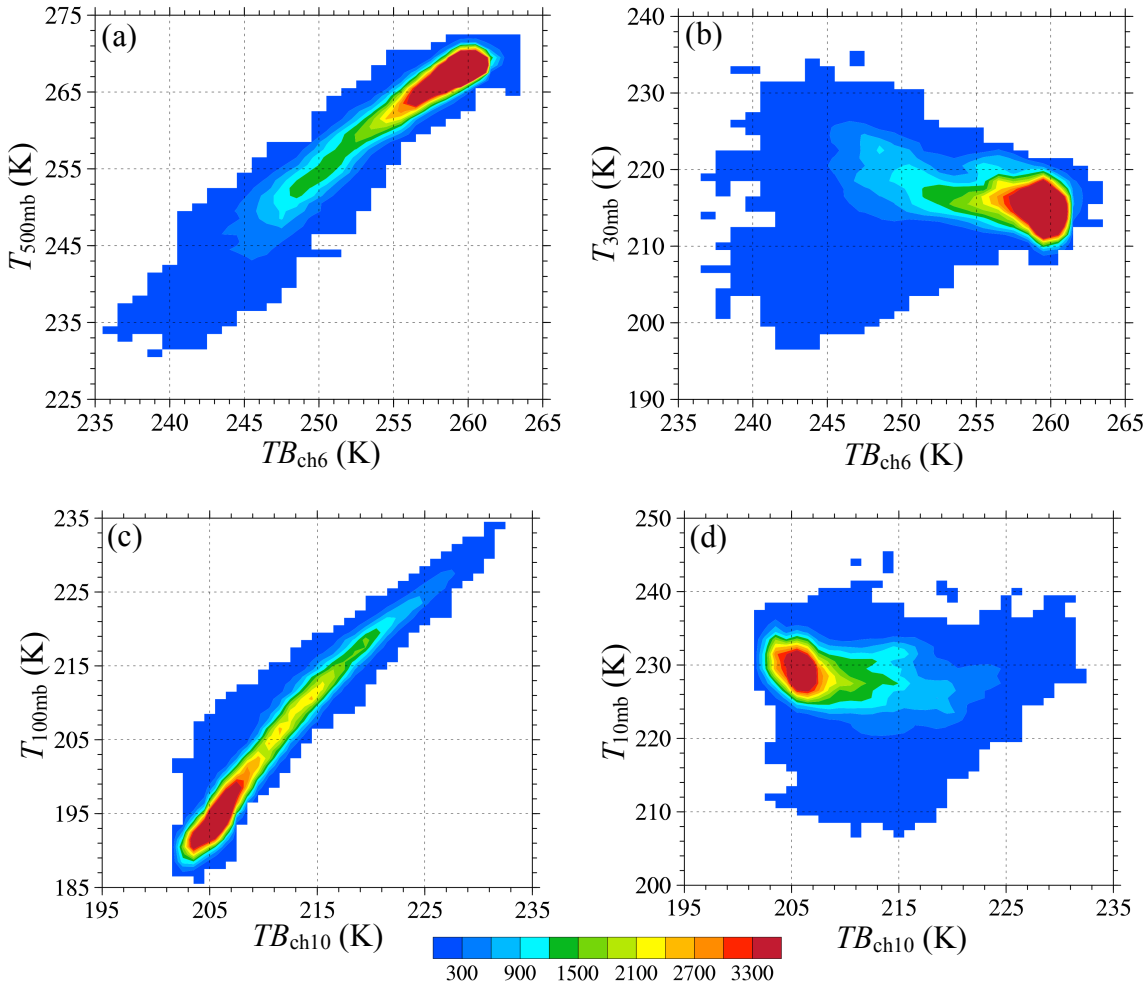

Figure 4.2: Data counts for ATMS brightness temperatures at channel 6 versus GFS temperatures at (a) 500 hPa and (b) 30 hPa and ATMS brightness temperatures at channel 10 versus GFS temperatures at (c) 100 hPa and (d) 10 hPa for all collocated data that are expressed in data counts within 1 K × 1 K grid boxes. The correlations and R2 values for a linear regression between the GFS temperatures and brightness temperatures for (a) are 0.9623 and 92.6%, for (b) are 0.3518 and 12.3%, for (c) are 0.9702 and 94.1%, and for (d) are 0.2721 and 7.41%.

Correlations between ATMS brightness temperatures at channels 5-15 and GFS temperatures from surface to 1 hPa are provided in Figure 4.3. Only clear-sky

data at nadir (scan positions 48 and 49) are used. Areas with correlations being greater than 0.5 or the weighting functions of ATMS channels 5-15 (shown in red curves) being greater than 0.1 are shaded in grey. At each pressure level, the channels included in equation (2) are either the channels that are correlated with temperatures or the channels whose weighting functions are not negligible at this pressure level, i.e. the channels shaded in grey. At a specific pressure level, those channels that satisfy neither of the criteria are considered "unnecessary" in retrieving the atmospheric temperatures, as brightness temperatures at these channels convey little information of atmospheric temperatures at the specified pressure level.

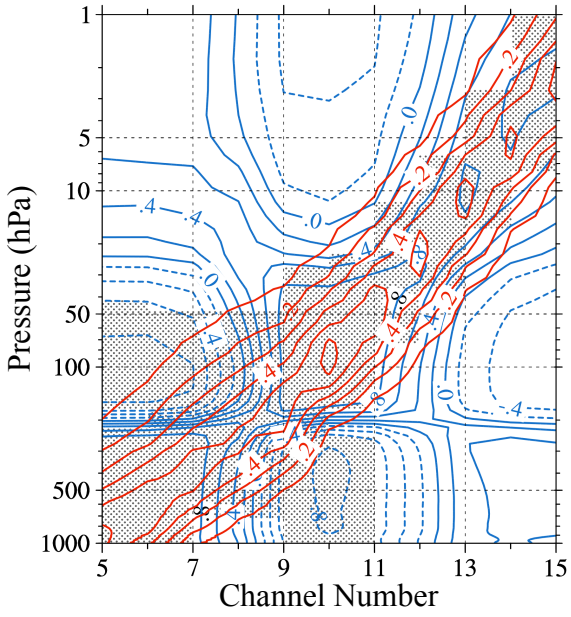

Figure 4.3: Correlations between ATMS brightness temperatures at channels 5–15 and GFS temperatures from surface to 1 hPa (blue curves). Only clear-sky data at nadir (FOVs 48 and 49) are used. Areas with an absolute value of the correlations greater than 0.5 or the weighting functions of ATMS channels 5–15 being greater than 0.1 (shown in red curves) are shaded in grey.

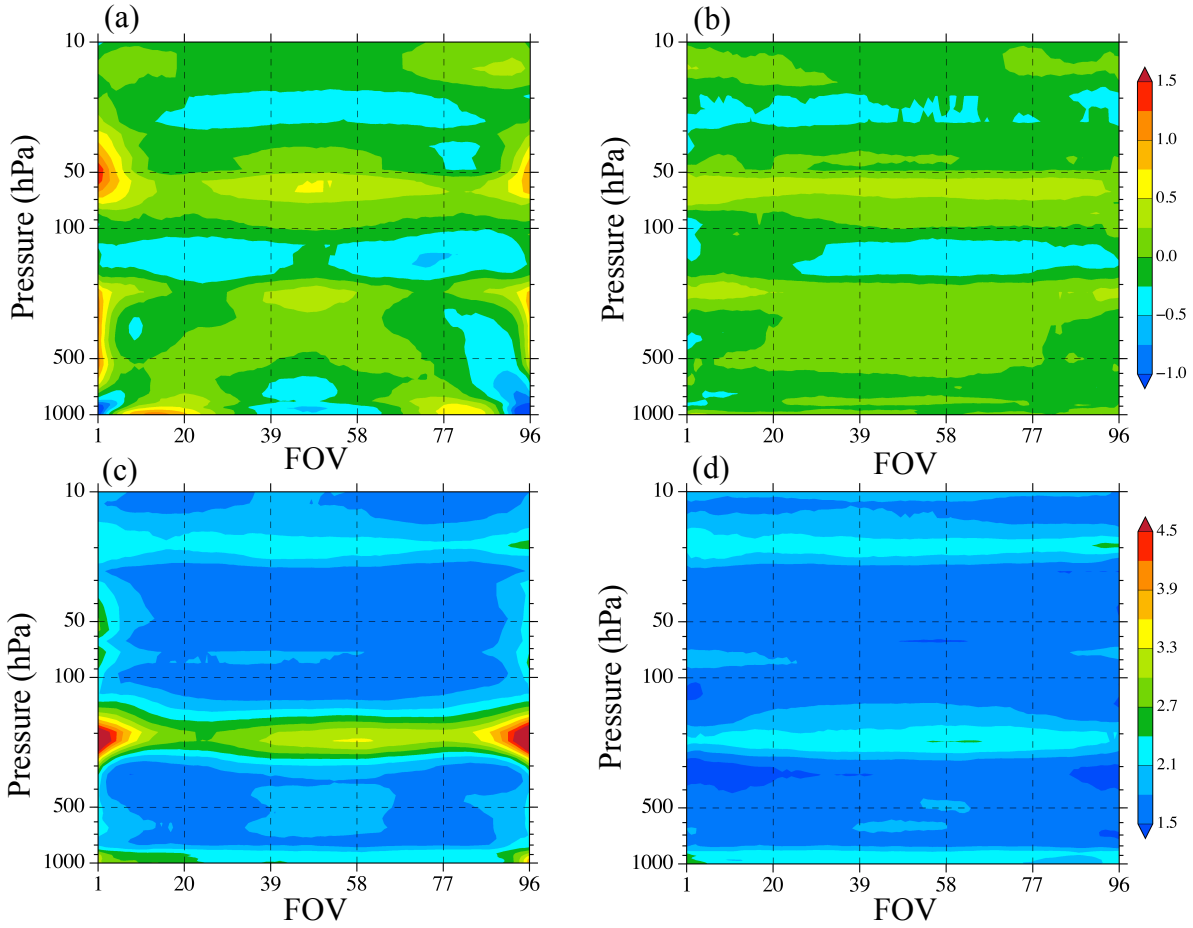

Figure 4.4: (a and b) Biases and (c and d) root-mean-square errors of the temperatures between ATMS retrievals and GFS reanalysis within the period from 22 to 31 October 2012. (a) and (c) are with the traditional algorithm and Figures 5b and 5d with the revised algorithm (W(p) > 0.1 or |corr| > 0.5).

The atmospheric temperatures at 64 vertical levels from GFS analysis and the collocated ATMS observation pixels with a ±1 h difference during the period from 8 to 21 October 2012 are included to train the regression coefficients in both the traditional and revised temperature retrieval algorithms. The biases of the atmospheric temperatures between ATMS retrievals and the GFS analysis during the period of Hurricane Sandy (from 22 to 31 October 2012) are shown in Figure 4.4. A significant scan dependent bias is found throughout the atmosphere (between 1000-10 hPa) for the temperature retrieval using the traditional method (Figure 4.4a). As was

mentioned above, the reason for this is that the last term in equation (4.1), $C_{sz}(p)\frac{1}{\cos(\theta)}$, for taking account for the scan biases for a cross-track radiometer in the traditional retrieval algorithm does not sufficiently remove the dependencies of ATMS observations on scan angles. In comparison, biases in the temperature retrievals from the revised algorithm are very small ($<\pm 0.5$ K) and have no scan dependence (Figure 4.4b). Figures 5c-d present the root mean square (RMS) errors between ATMS retrieved atmospheric temperatures using the traditional (Figure 4.4c) and revised (Figure 4.4d) methods and GFS temperatures ($\sigma = \sqrt{E\left[\left(T_{GFS} - T_{ATMS}\right)^2\right]}$). The revised ATMS temperature retrieval algorithm not only eliminated scan biases, but also considerably reduced the variability of the retrieved atmospheric temperatures.

4.2 Retrieved Warm Core Structures of Hurricanes Sandy and Michael

Hurricane Sandy developed from a tropical wave in the Caribbean Sea on October 22, 2012. It rapidly intensified and became a named tropical storm on the same day. As shown in Figure 4.5, Hurricane Sandy initially moved westward in the Caribbean Sea, then northward over Cuba and Bahamas and northeastward when entering middle latitudes. Hurricane Sandy intensified to a Category 1 hurricane on October 24 and further to a Category 3 prior to landfall in Cuba. Instead of continuing its northeastward movement, Sandy curved northwestward between 28 and 29 October 2012 and made its landfall on 30 October 2012.

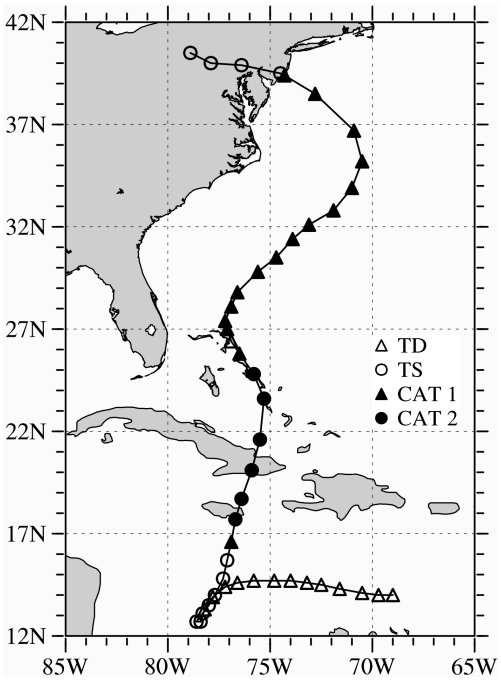

Figure 4.5: The track of Hurricane Sandy from 1200 UTC October 19 to 1800 UTC 30 October 2012, at 6 h interval. Sandy reached a peak intensity of category 3 at 0525 UTC October 2012.

The atmospheric temperature and anomalies throughout the life span of Sandy are retrieved from ATMS observations. Figure 4.6 shows the temporal and vertical structural evolutions of the temperature anomalies and potential temperatures retrieved with the traditional (Figure 4.6a) and revised (Figure 4.6b) algorithms at the hurricane center. The temperature anomalies are defined as the ATMS-retrieved temperatures subtracted by its average temperature within the 15˚ latitude/longitude box but outside of the 34-knot wind radial distance from the center of the hurricane. The evolution of Sandy's central sea level pressure (SLP) and maximum sustained surface wind obtained from the best track data is shown in Figure 4.6c. The significant difference in the upper tropospheric warm anomaly between the traditional and revised algorithms is quite stark during 22-25 October 2012 when Sandy evolved

from a tropical storm to Categories 2 and 3 hurricanes. The revised algorithm gives a consistent warm core structure in the upper troposphere between 200-300 hPa during this period (Figure 4.6a), which was barely captured by the traditional scheme (Figure 4.6a). Although being a Category 3 hurricane prior to landfall in Cuba, whose terrain height is indicated in Figure 4.6a-b, Sandy experienced a slight weakening moving over Cuba and became a Category 2 hurricane. It is noticed that the vertical structures of the temperature anomaly at the center of Sandy are significantly different before and after 1800 UTC 22 October as well as before and after 0600 UTC 26 October 2012. The temperature at the center of the storm initially has a slightly warm anomaly from the ocean surface to 300 hPa from 1800-2400 UTC 21 October 2012, during which Sandy remains a tropical depression. A warm anomaly in the upper troposphere and cold anomaly in the mid- and lower troposphere developed when Sandy evolved from a tropical depression to tropical storm, and intensified and extended to about 200-250 hPa when Sandy intensified more quickly to reach the highest intensity of Category 2. At about 0600 UTC 26 October 2012 when Sandy moved into subtropical and middle latitudes, a strong warm anomaly is found throughout the troposphere from the surface to about 200 hPa when Sandy remains a Category 1 hurricane.

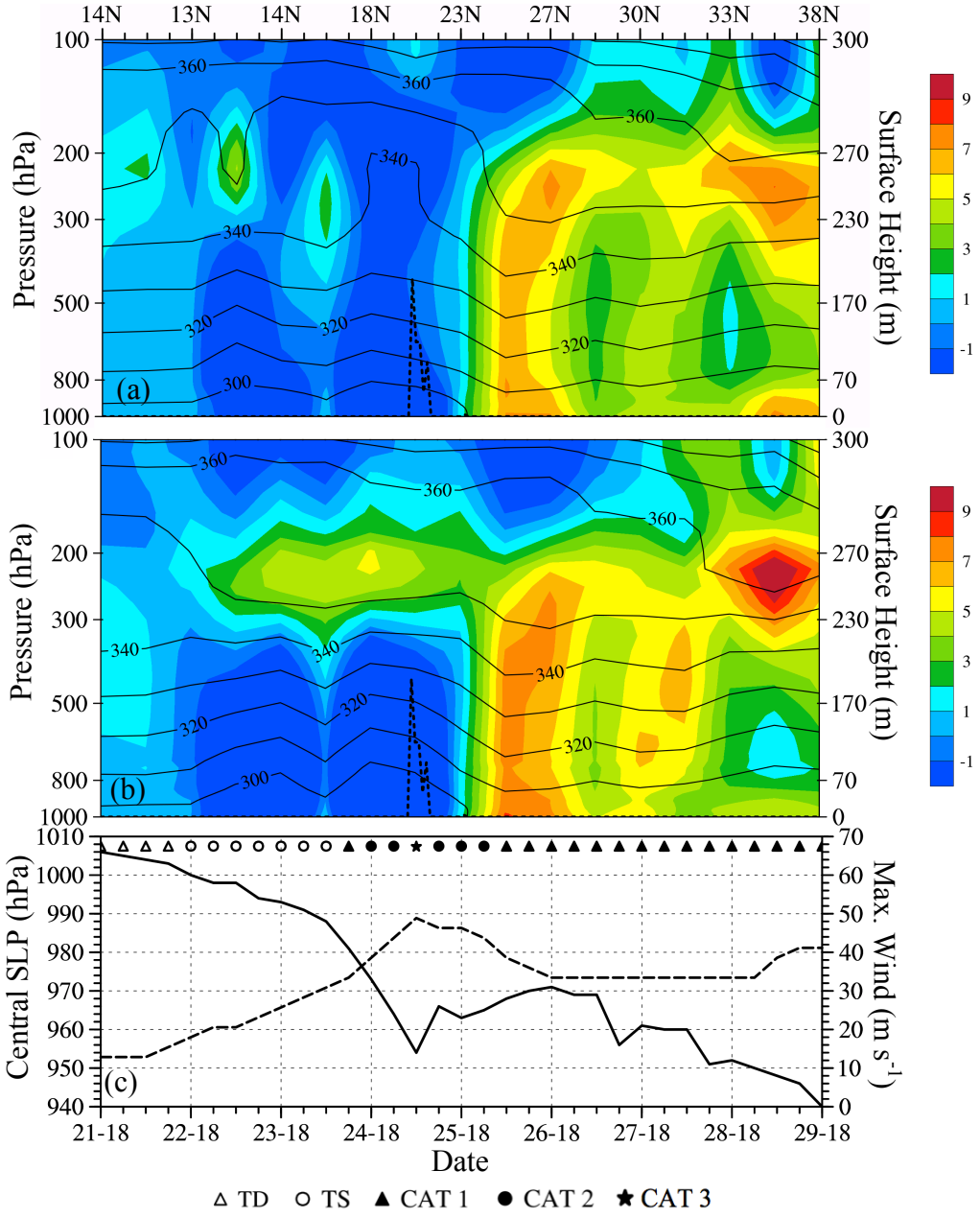

Figure 4.6: Temporal evolution of temperature anomalies (shaded) and potential temperatures (contour) at the center of Hurricane Sandy using the (a) traditional and (b) revised algorithms and (c) the central SLP (solid) and maximum sustained surface wind (dashed) of Hurricane Sandy from the best track data. The terrain height is indicated by dashed curve in (a) and (b).

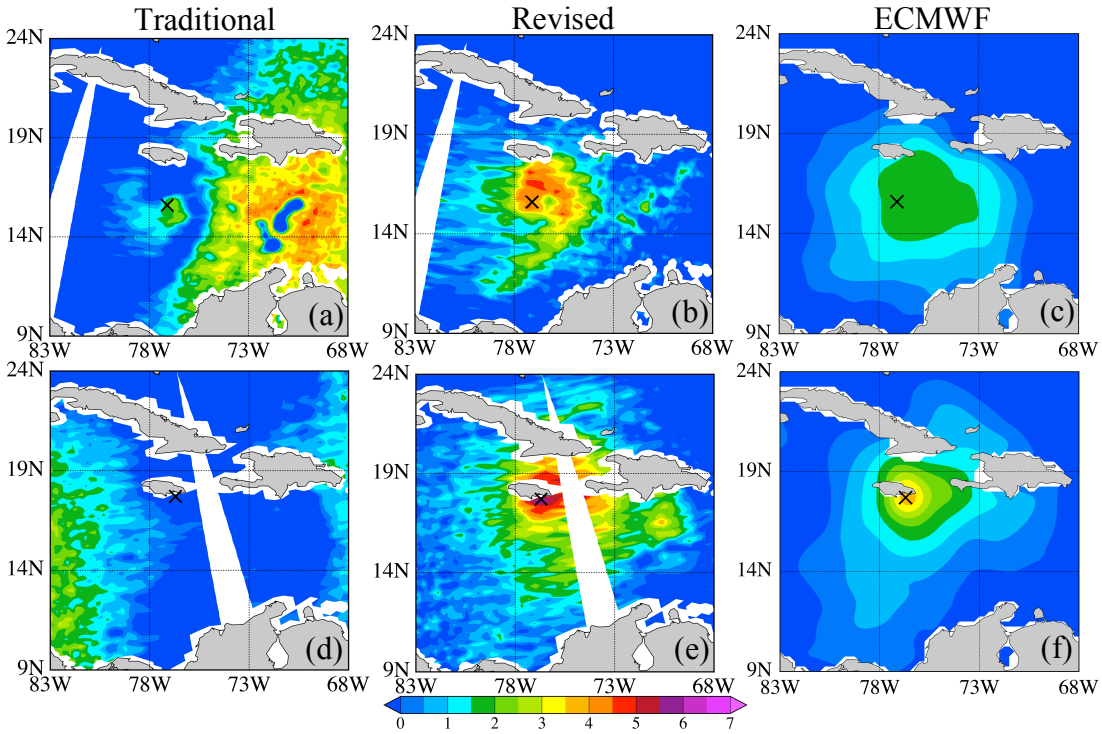

Figure 4.7: Temperature anomalies at 250 hPa at the (a-c) descending (0712 UTC) and (d-f) ascending (1822 UTC) nodes of S-NPP obtained with the traditional (a and d) and revised (b and e) ATMS temperature retrieval algorithms, as well as temperature anomalies at 250 hPa of ECMWF Interim at 0600 UTC (c) and 1800 UTC (f) for Hurricane Sandy on 24 October 2012.

The horizontal distributions of ATMS derived temperature anomalies at 250 hPa within Sandy at ATMS descending (0712 UTC) and ascending (1822 UTC) nodes on 24 October 2012 are provided in Figure 4.7. Figure 4.7b and 4.7e are the temperature anomalies calculated with the revised retrieval algorithm, Figure 4.7c and 4.7f being the temperature anomalies from ECMWF interim analysis. At 0600 UTC and 1800 UTC on October 24, Sandy is classified as tropical storm and Category 1 hurricane, respectively. Its warm cores are discernible in the temperature anomalies from ECMWF interim analysis. However, the temperature anomalies retrieved with both the descending and ascending node observations from traditional algorithm

(Figs. 4.7a and 4.7d) do not provide any warm core structures at 250 hPa, which is due to the scan biases that especially prevails when close to the swath edges as demonstrated in Figure 4.4. The results with the same ATMS observations but from revised algorithm can yield warms cores that are much more comparable to those in ECMWF interim analysis from the perspectives of both shapes and intensities, despite the location of the hurricane center with respect to a swath. Figure 4.8 demonstrates a similar comparison with Figure 4.7 only on October 28. By October 28, Sandy had entered middle latitudes and developed into a Category 1 Hurricane. At 250hPa, the warm core is primarily due to adiabatic heating of the descending air (Chen and Zhang 2012; Liu et al. 1999; Zhang and Chen 2012) The warm cores at 250 hPa retrieved with traditional method (Figure 4.8a and 4.8b) are broader at both the descending (0630 UTC) and ascending (1822 UTC) nodes of SNPP than those obtained by the revised algorithm. The warm cores in the ECMWF interim analysis are misplaced to the southeast. It seems that the reanalysis product cannot capture the warm core structure as realistically as satellite observations.

Figure 4.9 shows the cloud top pressure retrieved from VIIRS observations (Figure 4.9a) and VIIRS Day Night Band (DNB) radiance (Figure 4.9b) at 0600 UTC on October 28. In both the cloud top pressure and VIIRS DNB, Hurricane Sandy is highly asymmetric and the southeast half of the storm area is indicated to be covered with only low-level clouds or even clear sky. Hence, for the southeast half of the storm area, it is certain that convection should have little impact on the temperature field at 250 hPa. The strongest convection was located at the eyewall northwest of the center of Hurricane Sandy. Using the revised new algorithm, the warm core at this

time (Figure 4.8c) has the maximum temperature anomaly of more than 7 K being located at the same location where the convection is the strongest, i.e., the eyewall northwest of the center of Hurricane Sandy.

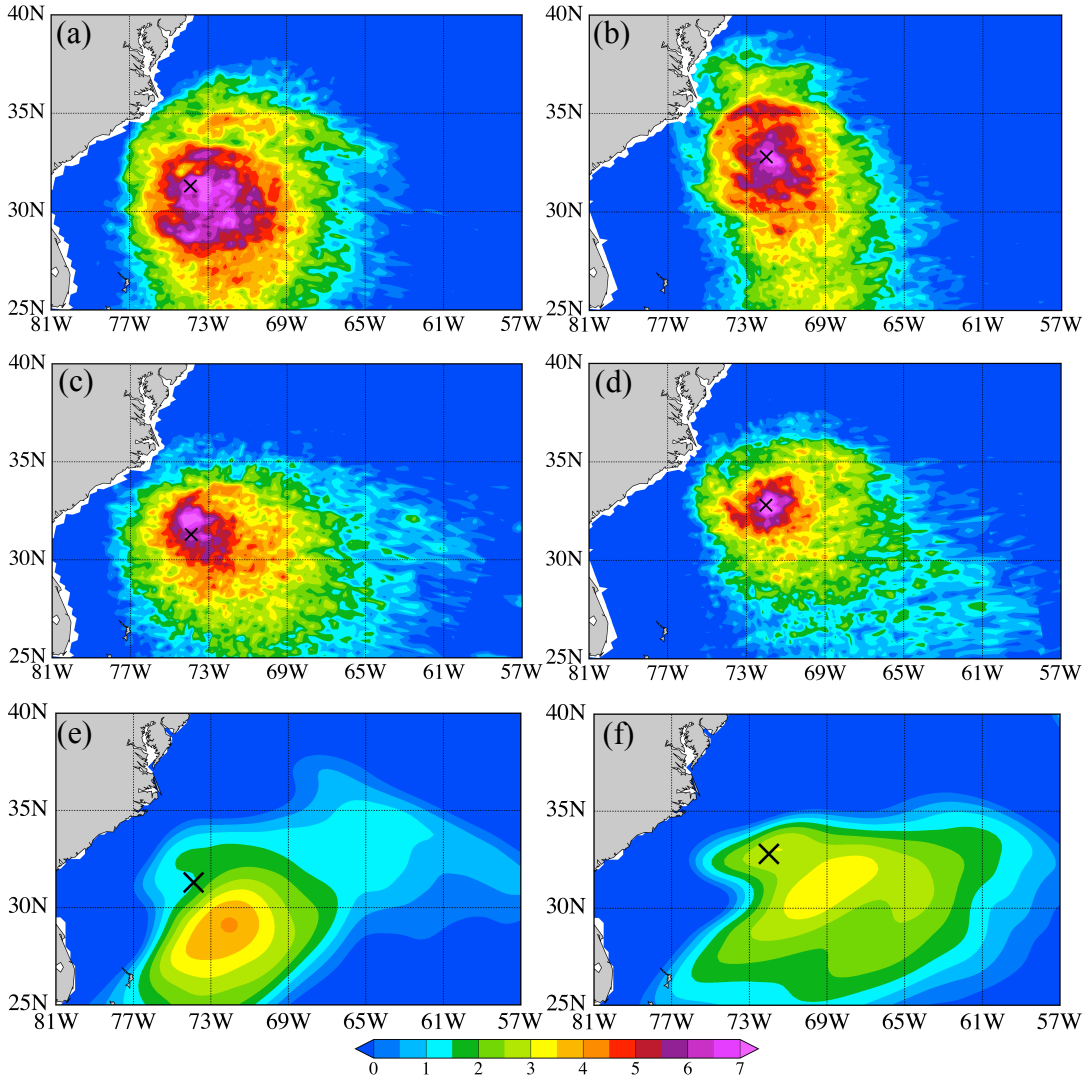

Figure 4.8: Temperature anomalies at 250 hPa at the (a, c, and e) descending (0630 UTC) and (b, d, and f) ascending (1822 UTC) nodes of S-NPP obtained with the traditional (a and b) and revised (c and d) ATMS temperature retrieval algorithms, as well as temperature anomalies at 250 hPa of ECMWF Interim analysis at 0600 UTC (e) and 1800 UTC (f) for Hurricane Sandy on 28 October 2012.

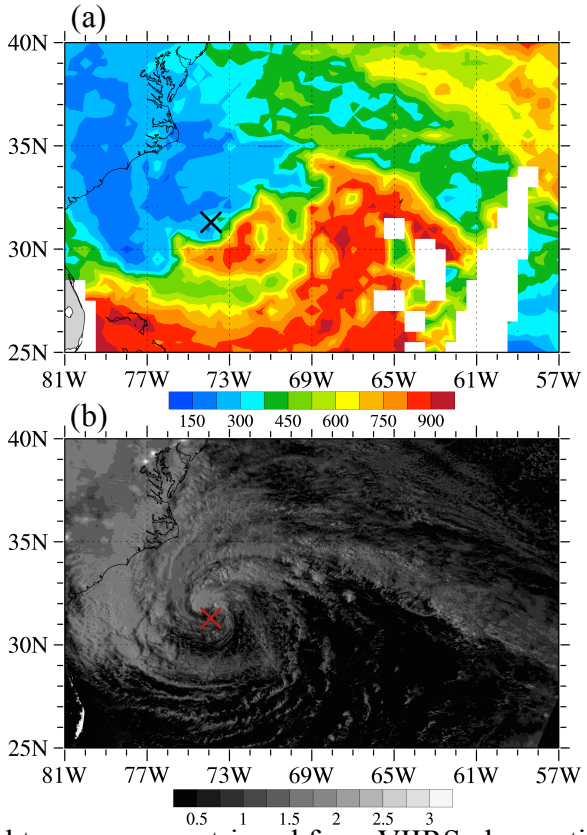

Figure 4.9: (a) Cloud top pressure retrieved from VIIRS observations at 0630 UTC on 28 October 2012. (b) VIIRS DNB radiance (unit: 10^{-8} W cm^{-2} sr^{-1}) on the descending node (~06:30 UTC) of S-NPP on 28 October 2012.

On October 26 (Figure 4.10), Sandy left Cuba and passed the Tropic of Cancer. The warm anomaly was located slightly to the east side of the center and stretched throughout the troposphere. When Sandy re-intensified to a well-developed hurricane, the warm core became more dominant in the upper troposphere on 28-29 October 2012, which is caused mainly by adiabatic warming of descending air from upper levels induced by radial inflows along the eye wall. The lower troposphere, nonetheless, also has a warm anomaly east of the center of Sandy, corresponding a clear atmosphere at this region (see Figure 4.9). It is worth mentioning that the TC's thermal structure in the lower troposphere between 700 hPa and 500 hPa may not be accurately represented by ATMS or model simulation in the presence of clouds.

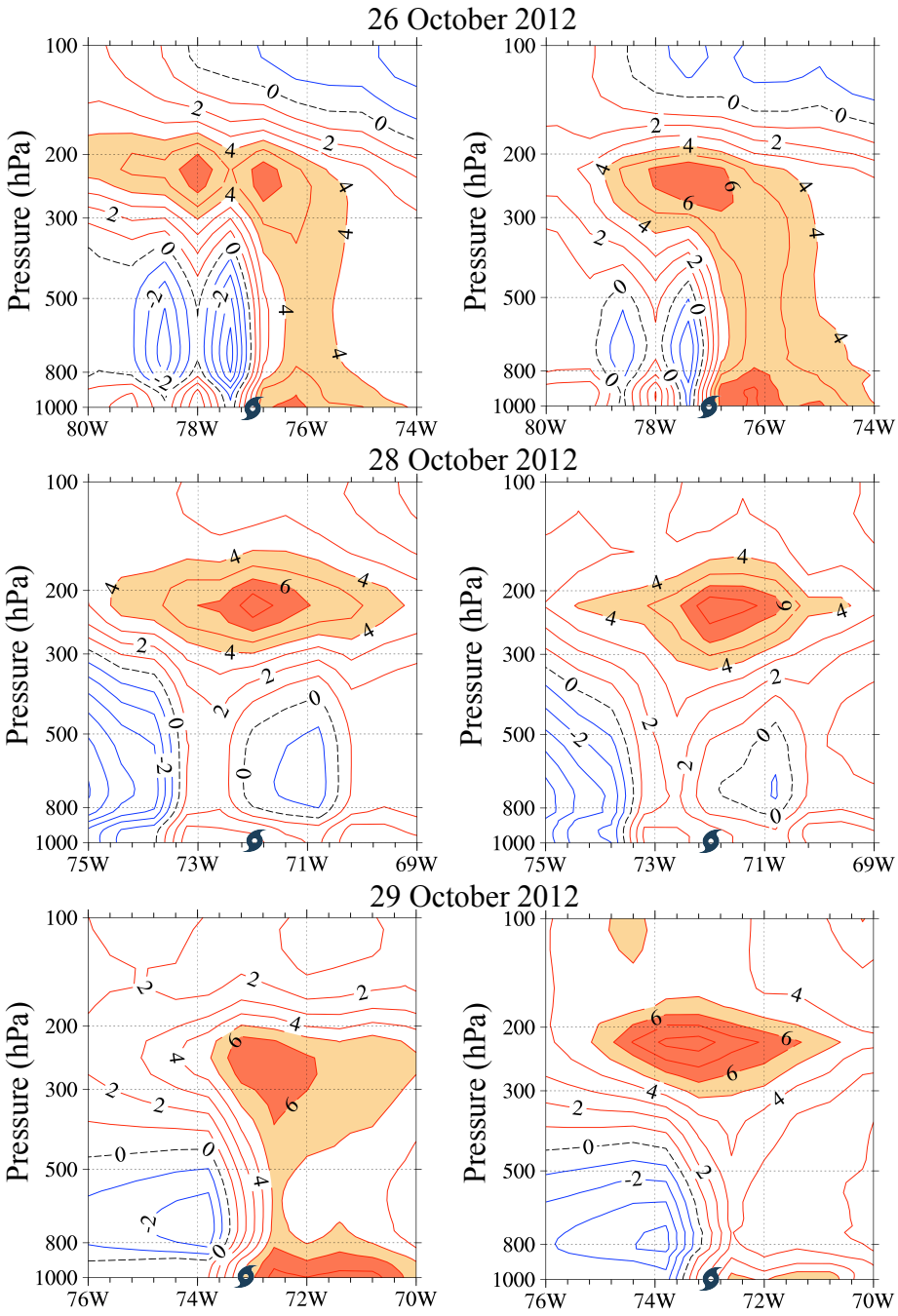

Figure 4.10: Vertical cross sections of temperature anomalies along the constant latitude passing through the center of Hurricane Sandy at 1800 UTC on 26, 28, and 29 October 2012 using the (left column) traditional and (right column) revised algorithms.

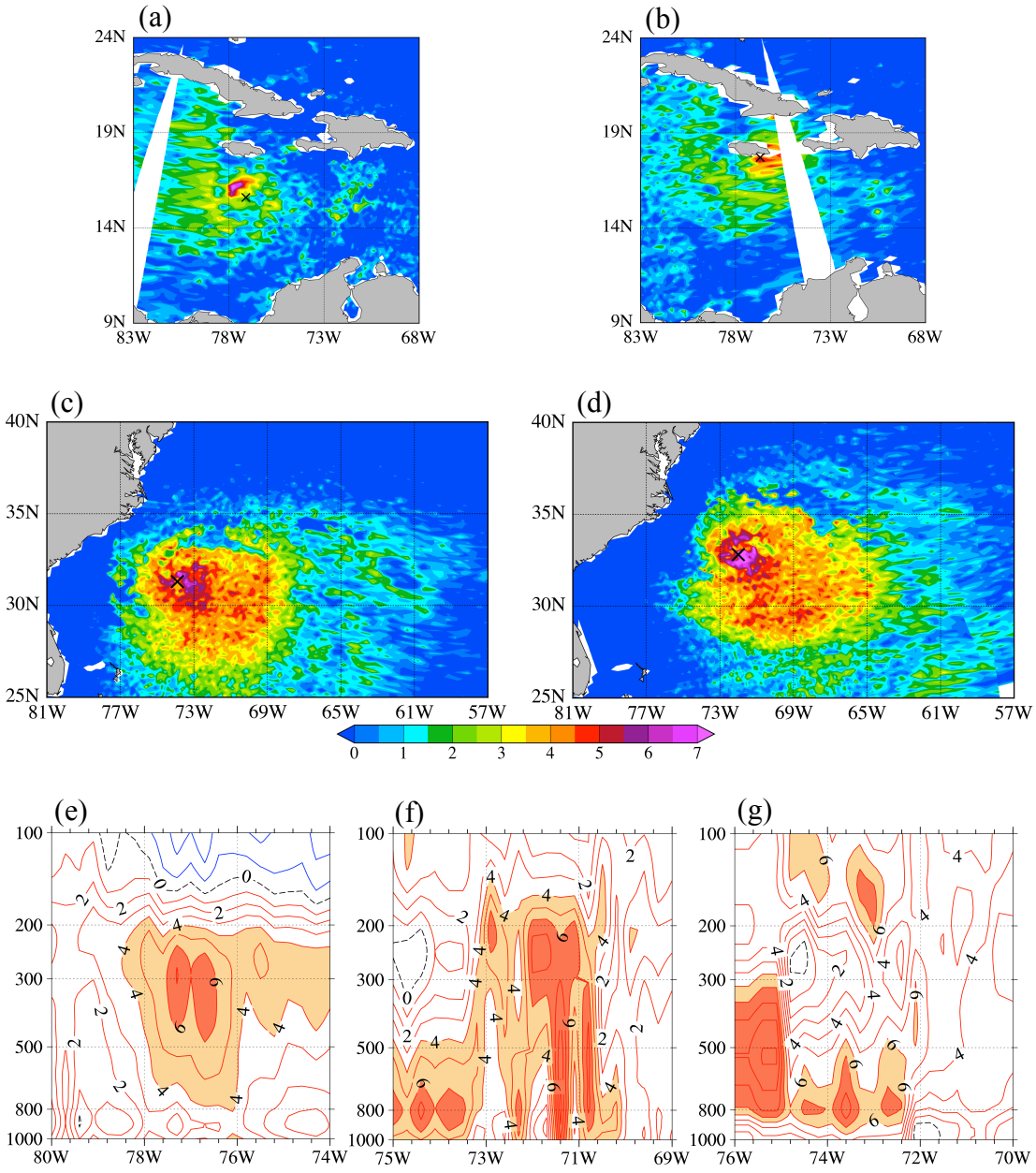

Figure 3.11: Temperature anomalies at 250 hPa on (a and b) 24 October and (c and d) 28 October 2012 obtained by MIRS from ATMS at the descending (a and c) and ascending (b and d) nodes of S-NPP. (e-g) Same as Figure 3.10 except for MIRS results.

In order to compare the results obtained by the proposed revised retrieval algorithm for Hurricane Sandy with the operational MIRS retrievals, we show in Figure 4.11 the temperature anomalies at 250 hPa on 24 October (Figure 4.11a-b) and 28 October (Figure 4.11c-d) 2012 obtained by MIRS from ATMS at both the

descending and ascending nodes of S-NPP, we well as the vertical cross sections of temperature anomalies along the constant latitude passing through the center of Hurricane Sandy at 1800 UTC on 26, 28 and 29 October 2012. The warm cores obtained from the MIRS operational retrievals on both 24 (Figure 4.11a-b) and 28 (Figure 4.11c-d) October 2012 are weaker and have smaller spatial scales than the temperature anomalies retrieved by the new algorithm (Figure 4.7b, e; Figure 4.8c-d). The vertical cross sections of the MIRS warm anomalies through the center of Hurricane Sandy along the constant latitude at 1800 UTC on 26, 28 and 29 October 2012 are quite different from those from the traditional and revised retrieval algorithms (Figure 4.10). The temperature anomalies obtained by the MIRS have features of smaller scales than those from the traditional and revised retrieval algorithms.

Hurricane warm core retrievals are made publicly available by the operational one-dimensional variation Microwave Integrated Retrieval System (MIRS). The MIRS retrievals are based on AMSU-A observations. In order to compare with the more sophisticated MIRS, the proposed revised retrieval algorithm is applied to AMSU-A onboard NOAA-18. Since ATMS channels 5-15 involved in the new modified retrieval algorithm are the same as AMSU-A channels 4-14, the same channel selection is used for the AMSU-A warm core retrieval using the proposed algorithm. Numerical results are then compared between the two algorithms for the warm core structures of Hurricane Michael (2012), which was a named storm at 0600 UTC 4 September 2012. Same as for Sandy, a two-week training period from 15 to 29 August 2012 is used for the regression of the modified scheme when it is applied

to Hurricane Michael. Figure 4.12 provides the temperature anomalies at 250 hPa in the hurricane core obtained by the revised algorithm and those from the MIRS retrievals at 1800 UTC 7 September and 1800 UTC 9 September 2012. Hurricane Michael had a hurricane intensity of Category II at 1800 UTC September 7 and Category I at 1800 UTC September 9, respectively. At both times the revised algorithm is able to retrieve a well-defined warm core structure in the upper troposphere. The warm cores obtained from the MIRS retrievals are much weaker and have a less coherent structure. Similar to Hurricane Sandy case, it seems that the reanalysis product also cannot capture the warm core structure of Hurricane Michael as realistically as satellite observations.

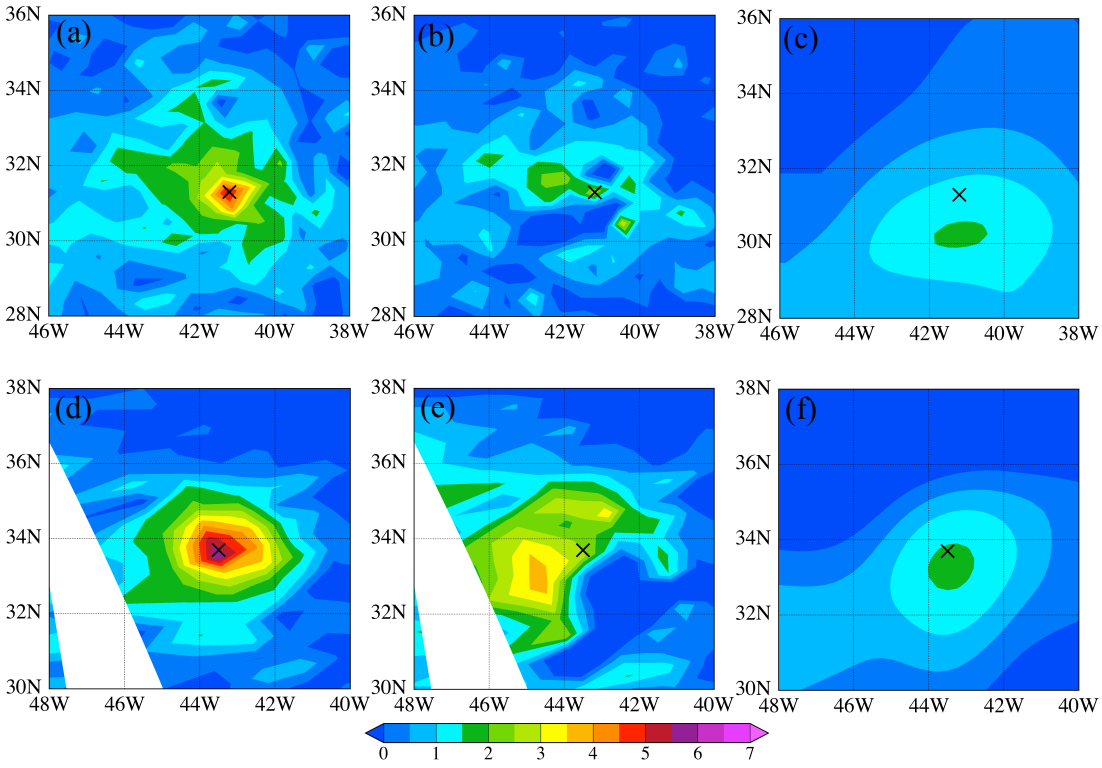

Figure 3.12: Temperature anomalies at 250 hPa from AMSU-A on board NOAA 18 at (a and b) 1800 UTC 7 September (hurricane category 2) and (d and e) 1800 UTC 9 September (hurricane category 1) 2012 using the revised warm core retrieval algorithm (a and d) and from MIRS (b and e). Temperature anomalies at 250 hPa of ECMWF Interim analysis at (c)

1800 UTC 7 September 2012 and (f) 1800 UTC 9 September 2012 for Hurricane Michael. The black cross indicates the center of Hurricane Michael which was located at (31.3°N, 41.2°W) for (a) and (b) and (33.7°N, 43.5°W) for (c) and (d).

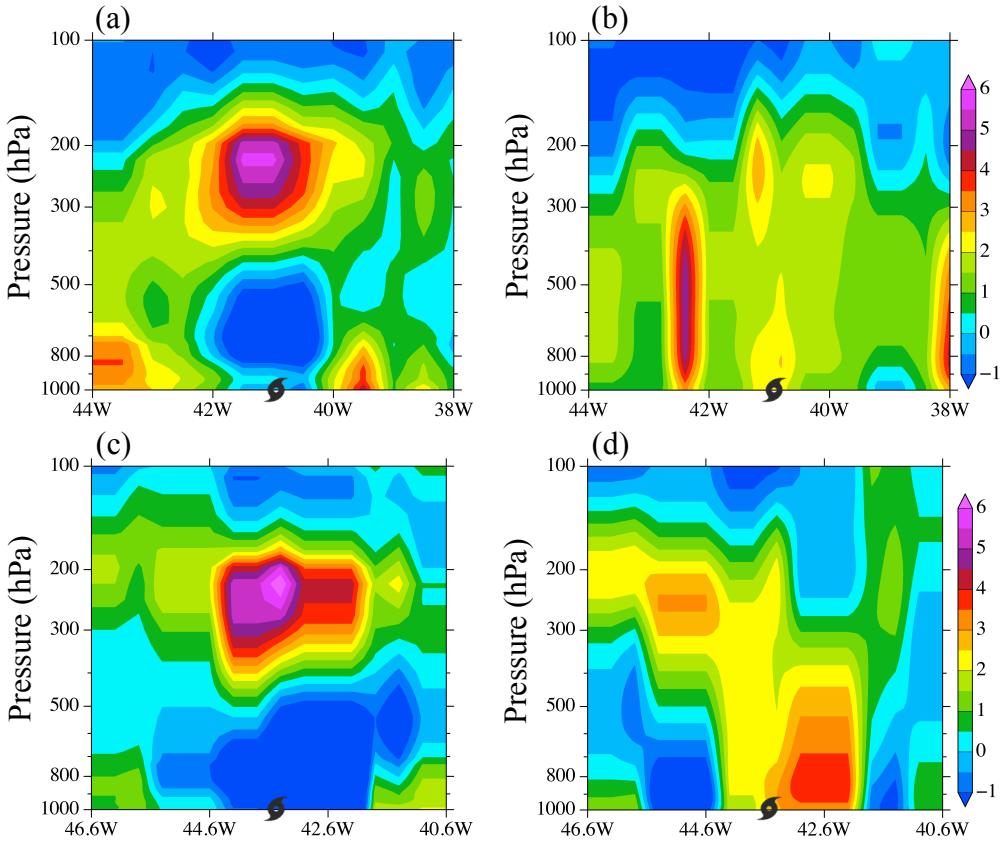

Figure 4.13: Same as Figure 4.12 except for cross sections from west to east at the latitudes of the center of Hurricane Michael (2012).

The vertical cross-sections from west to east across the center of Hurricane Michael for the same two times shown in Figure 4.12 are provided in Figure 4.13. Hurricane Michael from the revised algorithm (Figure 4.13a and c) had a well-defined warm core in the upper troposphere and a cold core below the warm core. The MIRS retrievals (Figure 4.13b and d) differ greatly from those obtained by the proposed algorithm and did not give a typical warm core feature for a hurricane at Categories I and II.

Chapter 5: A Simplified 4D-Var Vortex Initialization Model

5.1 A Description of Axisymmetric Hurricane Model

The nonhydrostatic hurricane model simulates the compressible and axisymmetric flow on an *f*-plane with a cylindrical coordinates (*r, ϕ, z*) (Rotunno and Emanuel 1987). The governing equations are as follows:

$$\frac{du}{dt}-\left(f+\frac{v}{r}\right)v=-c_p\overline{\theta}_v\frac{\partial\pi}{\partial r}+D_u \tag{5.1}$$

$$\frac{dv}{dt}+\left(f+\frac{v}{r}\right)u=D_v \tag{5.2}$$

$$\frac{dw}{dt}=-c_p\overline{\theta}_v\frac{\partial\pi}{\partial z}+g\left\{\frac{\theta-\overline{\theta}}{\overline{\theta}}+0.61\left(q_v-\overline{q}_v\right)-q_l\right\}+D_w \tag{5.3}$$

$$\frac{\partial\pi}{\partial t}+\frac{\overline{c}^2}{c_p\overline{\rho}\overline{\theta}_v^2}\left\{\frac{1}{r}\frac{\partial\left(ru\overline{\rho}\overline{\theta}_v\right)}{\partial r}+\frac{\partial\left(w\overline{\rho}\overline{\theta}_v\right)}{\partial z}\right\}=0 \tag{5.4}$$

$$\frac{d\theta}{dt}=M_\theta+D_\theta+R \tag{5.5}$$

$$\frac{dq_v}{dt}=M_{q_v}+D_{q_v} \tag{5.6}$$

$$\frac{dq_l}{dt}=M_{q_l}+D_{q_l} \tag{5.7}$$

During model calculation, the $\frac{d}{dt}$ operator will be converted into combinations of partial derivatives as $\frac{d}{dt}\equiv\frac{\partial}{\partial t}+u\frac{\partial}{\partial r}+w\frac{\partial}{\partial z}$. The dependent variables include radial (u), azimuthal (v), and vertical (w) velocities, nondimensional pressure perturbation from the initial state (π), the potential temperature (θ), the mixing ratios of water

vapor (q_v), and of liquid water (q_l). The M terms in eq. (5.5), (5.6), and (5.7) denotes microphysics effects described as follows:

$$M_\theta = -\frac{L}{c_p \pi}\frac{dq_{vs}}{dt} \tag{5.8}$$

$$M_{qv} = \frac{dq_{vs}}{dt} \tag{5.9}$$

$$M_{q_l} = -\frac{dq_{vs}}{dt} + \frac{1}{\bar{\rho}}\frac{\partial\left(\bar{\rho} V q_l\right)}{\partial z} \tag{5.10}$$

where L in eq. (5.8) is the latent heat of vaporization. The rate of condensation/evaporation is denoted by $\frac{dq_v}{dt}$. The V in eq. (5.10) represents terminal velocity of liquid water, value of which is given as

$$V = \begin{cases} 0\ ms^{-1}, & ql \le 1\ \text{g kg}^{-1} \\ 7\ ms^{-1}, & ql > 1\ \text{g kg}^{-1} \end{cases}.$$

The "D" terms in the governing equations denotes turbulence effects that are given as

$$D_u = \frac{1}{r}\frac{\partial r\tau_{rr}}{\partial r} + \frac{\partial \tau_{rz}}{\partial z} - \frac{\tau_{\phi\phi}}{r} \tag{5.11}$$

$$D_v = \frac{1}{r^2}\frac{\partial r^2\tau_{r\phi}}{\partial r} + \frac{\partial \tau_{z\phi}}{\partial z} \tag{5.12}$$

$$Dw = \frac{1}{r}\frac{\partial r\tau_{rz}}{\partial r} + \frac{\partial \tau_{zz}}{\partial z} \tag{5.13}$$

$$D_\theta = -\frac{1}{r}\frac{\partial rF_r^\theta}{\partial r} - \frac{\partial F_z^\theta}{\partial z} \tag{5.14}$$

$$D_{q_v} = -\frac{1}{r}\frac{\partial rF_r^{q_v}}{\partial r} - \frac{\partial F_z^{q_v}}{\partial z} \tag{5.15}$$

$$D_{q_l} = -\frac{1}{r}\frac{\partial r F_r^{q_l}}{\partial r} - \frac{\partial F_z^{q_l}}{\partial z} \tag{5.16}$$

where τ are the stresses and the F are the fluxes for each variable, which are calculated as

$$\tau_{rr} = 2\nu\frac{\partial u}{\partial r}, \qquad \tau_{\phi\phi} = 2\nu\left(\frac{u}{r}\right), \qquad \tau_{zz}=2\nu\frac{\partial w}{\partial z}$$
$$\tau_{r\phi} = \nu r\frac{\partial}{\partial r}\left(\frac{v}{r}\right), \ \tau_{rz} = \nu\left(\frac{\partial u}{\partial z}+\frac{\partial w}{\partial r}\right), \ \tau_{z\phi} = \nu\frac{\partial v}{\partial z},$$
$$F_r^{\chi} = -\nu\frac{\partial \chi}{\partial r}, \qquad F_z^{\chi} = -\nu\frac{\partial \chi}{\partial z}$$

where χ may denote θ, q_v or q_l. The ν is the eddy viscosity and $\nu = l^2 S$. S is given by

$$S^2 = 2\left[\left(\frac{\partial u}{\partial r}\right)^2+\left(\frac{u}{r}\right)^2+\left(\frac{\partial w}{\partial z}\right)^2\right]+\left(\frac{\partial u}{\partial z}+\frac{\partial w}{\partial r}\right)^2+\left(\frac{\partial v}{\partial r}-\frac{v}{r}\right)^2+\left(\frac{\partial v}{\partial z}\right)^2 \tag{5.17}$$

The R in eq. (5.5) denotes radiative cooling effects. The purpose is to remedy the large surface heat flux due to the increase of saturation equivalent temperature given rise by the pressure drop in the vortex evolution.

$$R = -\frac{\left(\theta-\bar{\theta}\right)}{\tau_R} \tag{5.18}$$

where $\tau_R = 12h$.

A rigid lid is placed on the upper boundary ($w = 0$). Also, at $z = z_{top}$, $\tau_{rz} = 0$, $\tau_{z\phi} = 0$ and $F_z^{\chi} = 0$. A sponge layer called the "graveyard for old gravity waves" is also set to damp out the gravity waves reflected back by the rigid lid. A Newtonian damping term $-\alpha(z)(\psi-\bar{\psi})$ is added to the right-hand side of all prognostic equations except for the one for π. $\alpha = 0$ for $z \le z_{sponge}$, and then increase to $\alpha_{\max}$ at

$z = z_{top}$. A few basic model parameters were taken as follows, $r_{outer} = 1500km$ and $z_{top} = 25km$ and cover this domain by 100 and 25 grid distances in the horizontal and vertical, respectively. So the radial grid size is $\Delta r = 15km$, and the vertical grid size is $\Delta z = 1km$. The "sponge" layer begins at 20 km. The large time step is $\Delta t = 20s$, so that a total of 32400 times steps are required to integrate out to 180h, the time by which the solutions become nearly steady (Figure 5.1a). The model evolves with a staggered grid, the alignment of which is shown in the Figure 5.1b. Variables including θ, π, q_v, and q_l also sit on the grids of v.

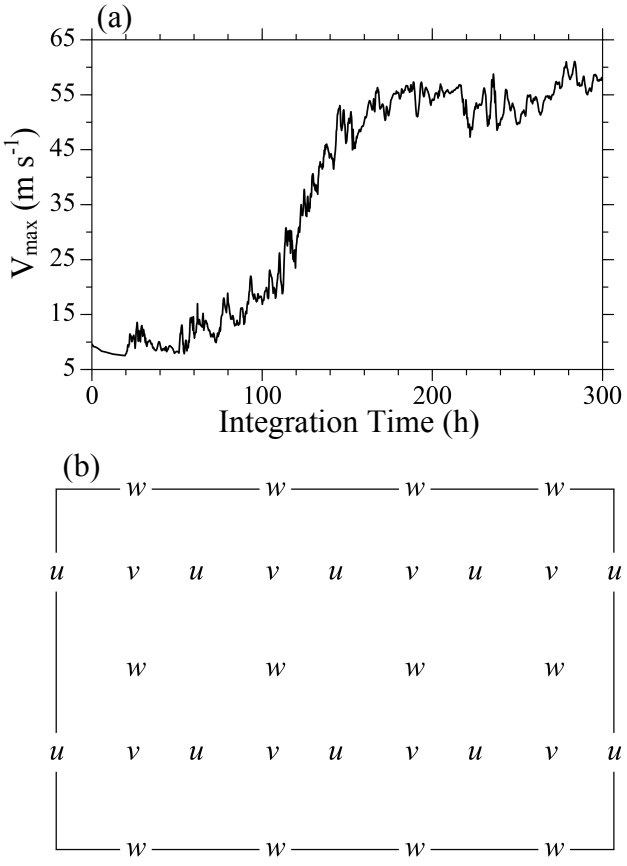

Figure 5.1: (a) The evolution of maximum tangential wind with respect to the integration time of the forward RE model. (b) Staggered grid alignment.

The RE model forecast results of all model variables with an integration time of 226.7 hours are given in Figure 5.2. The reason for selecting this specific time is explained in section 5.3.

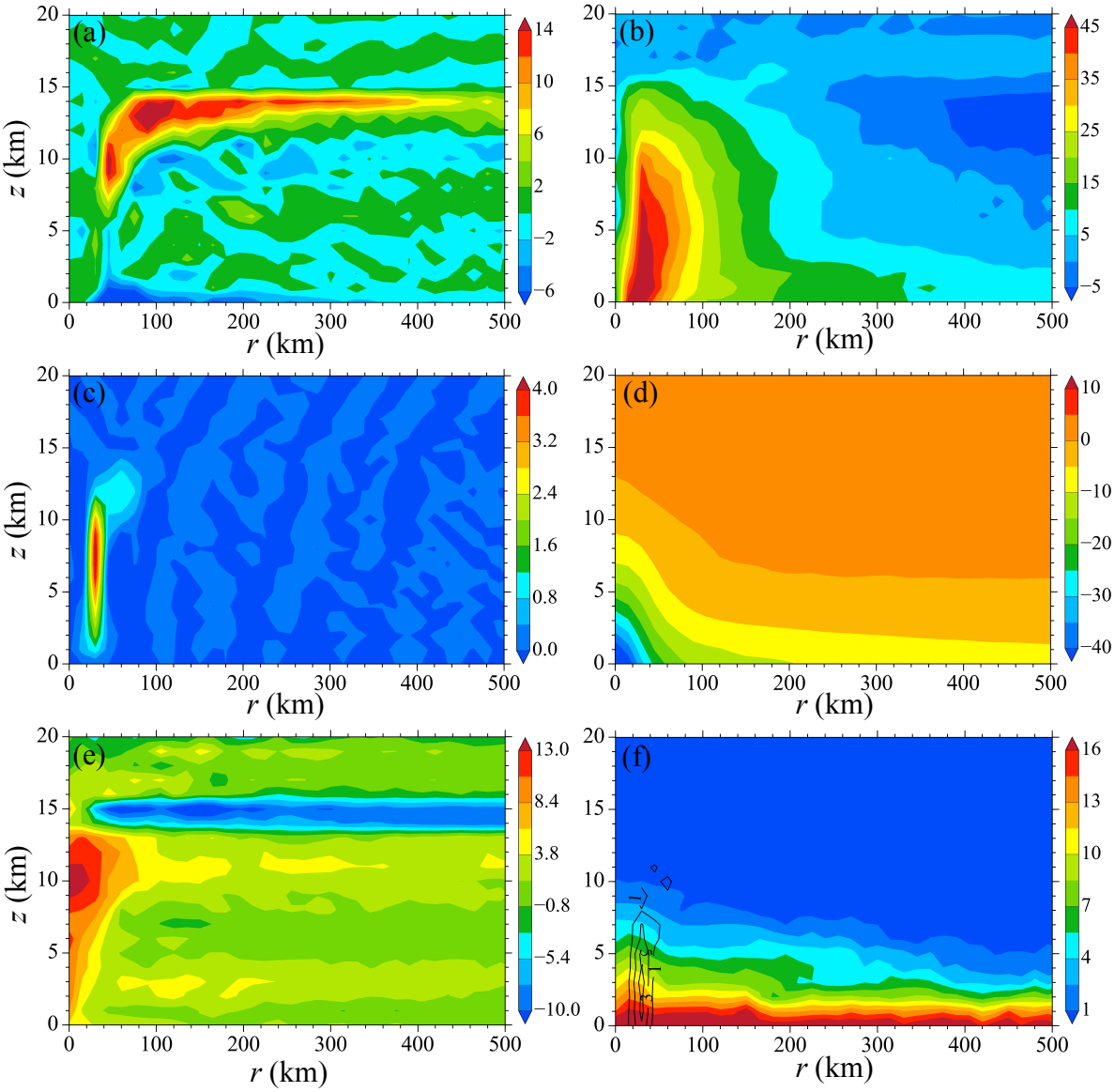

Figure 5.2: (a) Radial wind (u, $m\ s^{-1}$), (b) tangential wind (v, $m\ s^{-1}$), (c) vertical velocity (w, $m\ s^{-1}$), (d) pressure perturbation (p', hPa), (e) temperature anomaly (T', K), and (f) water vapor (q_v, $g\ kg^{-1}$) and liquid water (q_l, $g\ kg^{-1}$) mixing ratios predicted with RE forward model. The integration time is 226.7 hours.

5.2 A 4D-Var Hurricane Vortex Initialization Model

The 4D-Var hurricane vortex initialization model is to minimize the following cost function (Navon et al. 1992; Zou et al. 1993)

$$\begin{aligned} J(\mathbf{x}_0) &= J^b + J^o \\ &= \frac{1}{2}(\mathbf{x}_0 - \mathbf{x}_b)^T \mathbf{B}^{-1}(\mathbf{x}_0 - \mathbf{x}_b) \\ &+ \frac{1}{2}\sum_{r=0}^{n}(\mathbf{H}_r(\mathbf{x}_r) - \mathbf{y}_r)^T \mathbf{O}_r^{-1}(\mathbf{H}_r(\mathbf{x}_r) - \mathbf{y}_r) \end{aligned} \tag{5.19}$$

where $\mathbf{x}_0$ is the analysis vector on the analysis/forecast grid at time t_0. The $\mathbf{x}_b$ is the background field given by the model forecast at the time of interest. The $\mathbf{x}_r$ and $\mathbf{y}_r$ are model forecast and observations at time r. The $\mathbf{H}_r$ is the observation operator(s) that transforms model variables to observation space. $\boldsymbol{O}_r$ is the observation error covariance matrix of the r^{th} observation time. $\mathbf{B}$ is the background error covariance matrix. The first term on the right hand side, J^b, accounts for the model's contribution to the value of the cost function, i.e. the misfit between the model initial state and all available information prior to the assimilation period, summarized by the background field $\mathbf{x}_b$. The second term, J^o, measures distances of the model states from the observations at appropriate times within the assimilation window, which can consist of various types of observations within the assimilation window.

In order to minimize the cost function, the gradient of J with respect to the initial condition (IC) ($\mathbf{x}_0$) is required by any optimization algorithms:

$$\begin{aligned} \nabla J &= \nabla J^b + \nabla J^o \\ &= \mathbf{B}^{-1}(\mathbf{x}_0 - \mathbf{x}_b) + \sum_{r=0}^{R} \mathbf{P}_r^T \mathbf{H}_r^T \mathbf{O}_r^{-1}(\mathbf{H}_r(\mathbf{x}_r) - \mathbf{y}_r) \end{aligned} \tag{5.20}$$

where $\mathbf{H}_r^T$ is the adjoint of the linearized observation operator; $\mathbf{P}_r^T$ is the adjoint model of RE model. Similar to eq. (5.19), the gradient of the cost function with respect to IC consists of contributions from the misfit between the solution and background, ∇J^b, and the distance between the model state and the observations, ∇J^o. From eq. (5.20), it is obvious that the adjoint operators of both RE model and linearized observation operators are required in order to find the solution where the cost function is the minimum.

The RE hurricane forecast model is a limited domain nonhydrostatic finite-difference model, which can be denoted as

$$\mathbf{x}(t_r) = \mathbf{Q}_r(\mathbf{x})\mathbf{x}_0 \tag{5.21}$$

where $\mathbf{x}_0$ represents IC. The $\mathbf{x}$ includes all seven model variables specified in Section 5.1. The forward model $\mathbf{Q}_r(\mathbf{x})$ is nonlinear in nature. Linearizing the RE model, i.e. $\mathbf{Q}_r(\mathbf{x})$, the tangent linear model (TLM) can be obtained as

$$\mathbf{x}'(t_r) = \mathbf{P}_r(\mathbf{x})\mathbf{x}'_0 = \frac{\partial \mathbf{Q}_r}{\partial \mathbf{x}}\mathbf{x}'_0 \tag{5.22}$$

where primes represent perturbations of the corresponding variables. Integrating the RE TLM from a perturbed IC $(\mathbf{x}'_0)$, the perturbation solution $\mathbf{x}'(t)$ obtained is accurate to the first-order approximation $O\left(\left\|\mathbf{x}'_0\right\|^2\right)$ compared to the perturbation solution

$$\mathbf{x}'_{ture}(t) = \mathbf{x}(t)\big|_{(\mathbf{x}_0+\mathbf{x}'_0)} - \mathbf{x}(t)\big|_{(\mathbf{x}_0)}, \tag{5.23}$$

the TLM solution $\mathbf{x}'$ satisfies the following equation

$$\mathbf{x}'_{ture}(t) = \mathbf{x}'(t) + O\left(\left\|\mathbf{x}'_0\right\|^2\right) \tag{5.24}$$

With the aid of relationship (5.24), the correctness of the tangent linear model can be checked with examining the results of

$$\Phi(\alpha)=\frac{\left\|\mathbf{Q}_r(\mathbf{z}+\alpha\mathbf{h})-\mathbf{Q}_r(\mathbf{z})\right\|}{\alpha\mathbf{P}_r\mathbf{h}}=1+O(\alpha) \tag{5.25}$$

The result of applying eq. (5.25) can be found in Figure 5.3. It is shown that the value of $\Phi(\alpha)$ is linearly approaching unity as the size of α decreases. When α becomes smaller than 10^{-7}, the $\Phi(\alpha)$ starts to gradually drift away from 1.

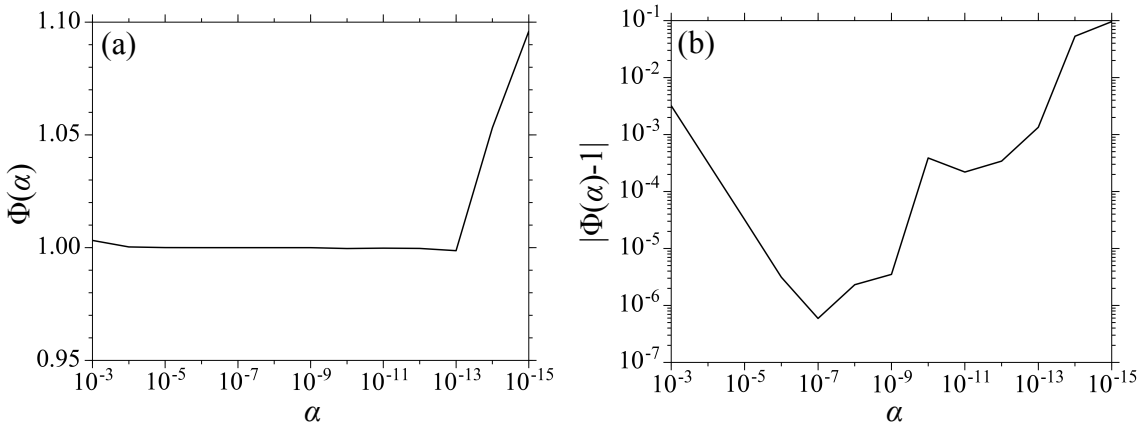

Figure 5.3: Verification of the TLM check calculation: (a) the variation of $\Phi(\alpha)$ with respect to α; (b) variation of $|\Phi(\alpha)-1|$ with respect to α in logarithm scale.

The adjoint model corresponding to the TLM given in eq. (5.22) is

$$\hat{\mathbf{z}}^r=\mathbf{P}_r^T(\mathbf{x})\mathbf{x}(t_r) \tag{5.26a}$$

$$\hat{\mathbf{x}}(t_r)=(\textit{forcing term}),\ r=R,\ R-1,\ \ldots,\ 0 \tag{5.26b}$$

where the hat represents that the variable is an adjoint variable. The t_r represents the final time of interest. R is the total number of time steps at which forecast fields are examined. A comparison between eq. (5.26) and eq. (5.24) indicates that the adjoint model is simply the transpose of the TLM. Therefore, the development of the adjoint

model is to rewrite the TLM line by line so to realize the transpose of the TLM. The correctness of adjoint model can be checked with

$$\left(\mathbf{P}_r\mathbf{z}\right)^T\left(\mathbf{P}_r\mathbf{z}\right)=\mathbf{z}^T\left(\mathbf{P}_r^T\left(\mathbf{P}_r\mathbf{z}\right)\right) \tag{5.27}$$

The left hand side (LHS) of eq. (5.27) is the results from TLM with an initial perturbation $\mathbf{z}$ as the input. The right hand side (RHS) is the product of $\mathbf{z}^T$ and the results of adjoint model taking $\mathbf{P}_r\mathbf{z}$ as input. In this study, the LHS is 2977863.8507716, the RHS being 2977863.8507647, which has 11 of the same effective digits that is close to the machines precision. A detailed derivation and instruction on the development of adjoint model can be found in Zou et al. (1997).

In this research two types of "observations" are assimilated into the initialization model, which are 1) three-dimensional temperature field retrieved with ATMS observations and 2) liquid water path (LWP) and total precipitable water (TPW) retrieved with AMSR2 observations. Accordingly, two types of observation operators ($\mathbf{H}_r$) are developed to transform model variables to match each observation type. In the case of ATMS, the operator takes pressure perturbations (π) and potential temperatures (θ) from model forecast as input to generate atmospheric temperatures and interpolate to match with ATMS observations pixels. For AMSR2 variables, the operator takes pressure perturbations (π), potential temperatures (θ), water vapor (q_v), and liquid water (q_l) mixing ratios as inputs and generates LWP and TPW to match AMSR2 observation variables and locations. The tangent linear and adjoint of the observation operators are then coded in the same fashion as those of the RE model. The model and observation error covariance matrices are chosen to be both diagonal without considerations of error correlations. The model errors variances are the

variances of differences between the forecasts at each time step during a 50-hour period of time after the RE model reaches the steady state (from 227h to 277h) and the mean state during the same period. The observations errors variances, including those for temperatures from ATMS and LWP and TPW from AMSR2, are calculated as the variances of the differences between the retrieved variables and the same variables from ECMWF Interim Reanalysis. With every element in eq. (5.20) ready, the correctness of the cost function gradient, similar with the correctness check of TLM, can be verified through

$$\psi(\alpha)=\frac{J^o(\mathbf{x}_0+\alpha\mathbf{h})-J^o(\mathbf{x}_0)}{\alpha\mathbf{h}^T\nabla J^o(\mathbf{x}_0)}=1+O(\alpha) \tag{5.28}$$

The result of eq. (5.28) is shown in Figure 5.4.

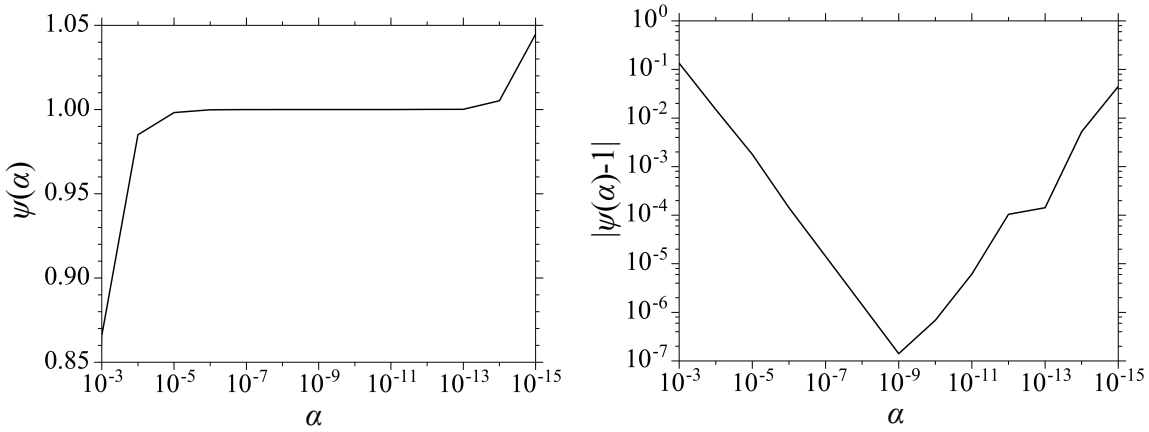

Figure 5.4: Verification of the gradient check calculation: (a) the variation of $\psi(\alpha)$ with respect to α; (b) variation of $|\psi(\alpha)-1|$ with respect to α in logarithm scale.

Once the cost function and the gradients of the cost function are calculated, they can be input into a minimization algorithm to search the minimum values. The

minimization algorithm adopted in this study is limited memory BFGS (L-BFGS) method (Liu and Nocedal 1989; Zhu et al. 1997).

5.3 Application of the Vortex Initialization Model in Hurricane Gaston (2016)

Hurricane Gaston (2016) was a storm with the highest intensity of Category 3 hurricane that originated near the west coast of Africa on 22 August 2016. It reached the hurricane intensity at 12:00 UTC on 24 August, its peak intensity by 18:00 UTC 27 August, and weakened below hurricane intensity by 12:00 UTC on 2 September. The recorded maximum wind speed is 54.65 m s^{-1}. The storm track can be found in Figure 5.5.

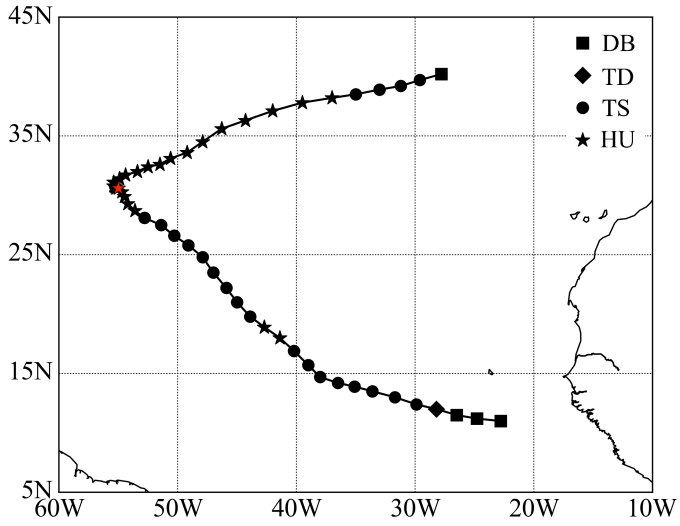

Figure 5.5: The storm track of Hurricane Gaston (2016) from August 22 to September 3, 2016. The red pentagon is at 18:00 UTC on August 28, 2016.

At 18:00 UTC on August 28 (marked in red pentagon), the Hurricane Gaston was about to take a turn from westward to eastward propagation. The observations of both ATMS and AMSR2 near this time are selected for assimilation into the initialization model to get an analysis field. As the RE model evolves in time that is relative to the

initial condition, in order to match a model time step to the hurricane intensity at 18:00 UTC August 28, the maximum wind of Hurricane Gaston from BestTrack is compared with the maximum wind evolution shown in Figure 5.1. The matching time step is 40800, i.e. 226.7 hours integrating from the initial condition. The model forecast results are then compared with ATMS and AMSR2 observations scanning through the storm in ascending nodes for the assimilation model to obtain an analysis that is 20 minutes (60 time strides) prior. The observed warm core, LWP, and TPW surrounding Hurricane Gaston on August 28 is given in Figure 5.6.

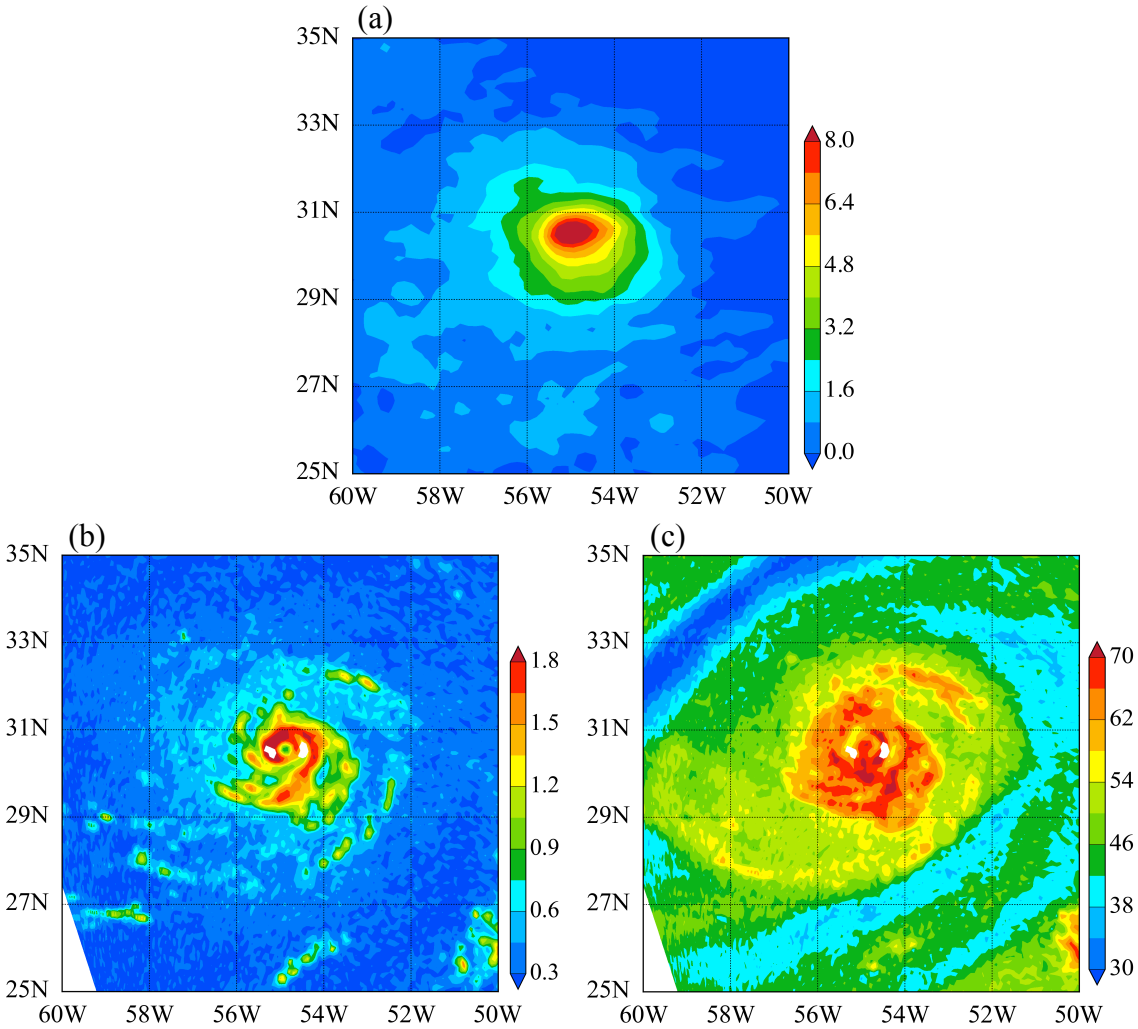

Figure 5.6: (a) The temperature anomalies at 250 hPa retrieved with ATMS observations, (b) LWP, and (c) TPW retrieved with AMSR2 observations at ascending nodes on August 28, 2016.

With the L-BFGS minimization algorithm, the values of the normalized cost functions and the norm of the gradients are shown in Figure 5.7. The norm of the gradient is reduced by two orders of magnitude, which verifies that the cost function obtained is a minimum.

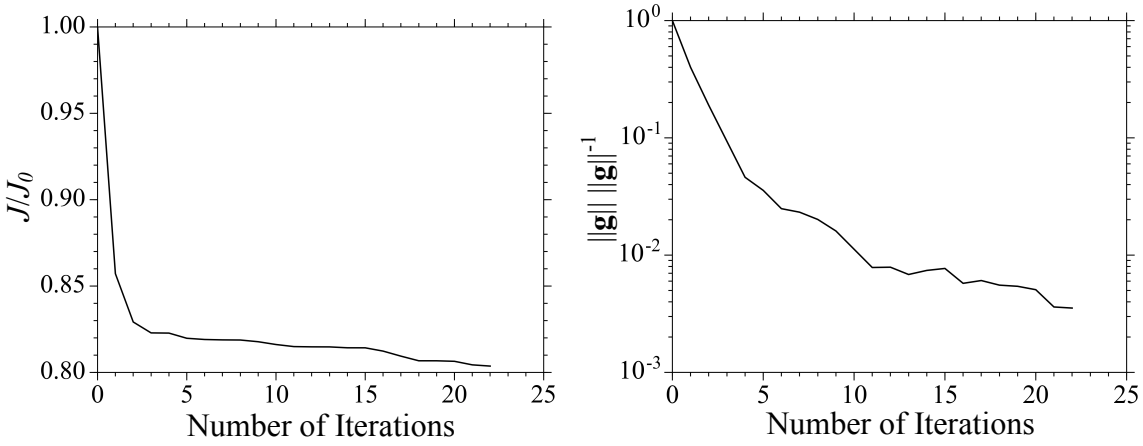

Figure 5.7: Variations of the normalized cost function (J/J_0) and normalized gradient ($\|\mathbf{g}\|\ \|\mathbf{g}\|^{-1}$) with the number of iterations.

The solution at which the cost function reaches its minimum is then compared with the initial guess, i.e. RE model forecast results at step 40800. The increments of every model variables are plotted in Figure 5.8.

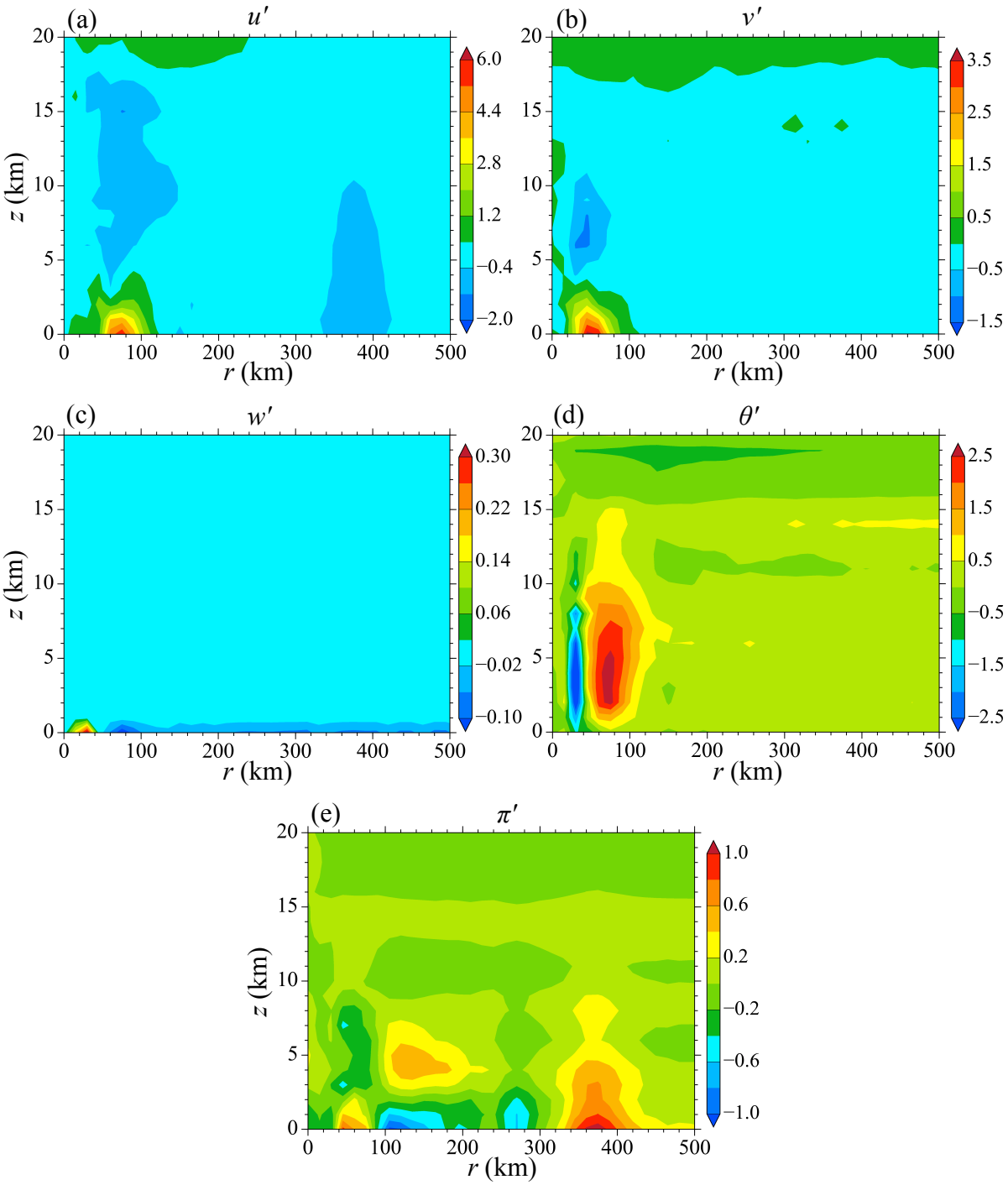
(a)
u'
6.0
4.4
2.8
1.2
−0.4
−2.0
(b)
v'
3.5
2.5
1.5
0.5
−0.5
−1.5
(c)
w'
0.30
0.22
0.14
0.06
−0.02
−0.10
(d)
θ'
2.5
1.5
0.5
−0.5
−1.5
−2.5
(e)
π'
1.0
0.6
0.2
−0.2
−0.6
−1.0
z (km)
r (km)
0
5
10
15
20
100
200
300
400
500

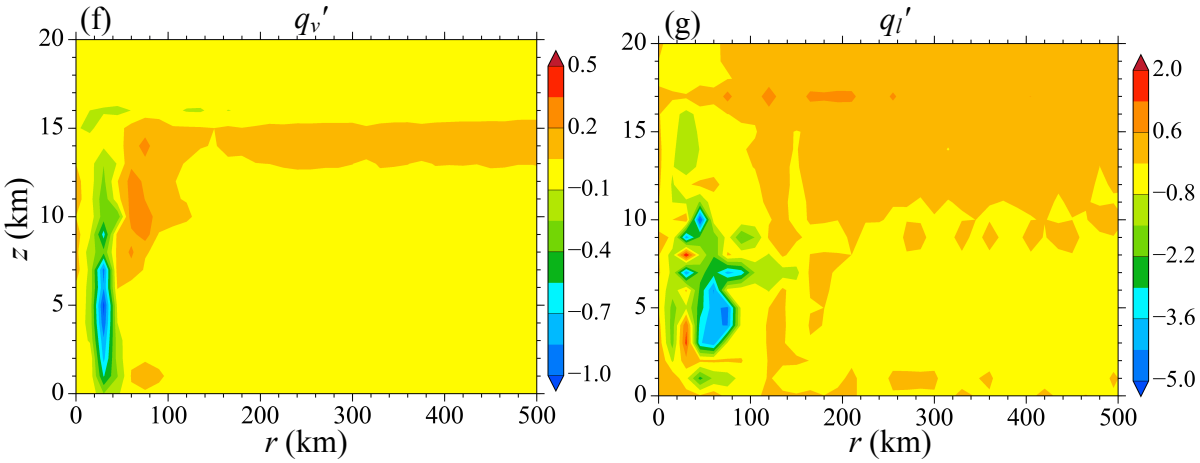

Figure 5.8: The increments of the analysis field with respect to the first guess of (a) radial wind (*u, m s*$^{-1}$), (b) tangential wind (*v, m s*$^{-1}$), (c) vertical velocity (*w, m s*$^{-1}$), (d) pressure perturbation (*p', 10*$^{-7}$•*hPa*), (e) temperature anomaly (*T', K*), (f) water vapor (q_v, *10*$^{-5}$•*g kg*$^{-1}$), and (g) liquid water (q_l, 10^{-8}•*g kg*$^{-1}$) mixing ratios.

It is indicated that for both the the tangential and radial wind fields, while the increments on most areas are close to zero, they are enhanced compared with the first guess for the layer below 5 km and region within 100 km radius from the storm center. In the layer above 5 km, both wind components are slightly reduced. In the case of vertical velocity, the ascending near surface was made stronger within about 40 km of the center. In other near surface regions, the vertical velocities become smaller. The increment of the potential temperature fields shows a band of negative modifications between 20 km and 40 km from the center, and a band of positive increments immediately outside the negatives. It is likely that the warm core of the hurricane is being shifted slightly outward. Nonetheless, the increments in water vapor and liquid water mixing ratios are orders of magnitudes smaller than the fields themselves. Therefore, with the current model configurations, the assimilation of LWP and TPW is not introducing any significant changes into the two hydrological variables. Figure 5.9 is the hurricane warm core structure from the analysis and that

by averaging observations into the same coordinates. Comparing Figure 5.9a and Figure 5.2e, in the layer below 5 km and the region between 20 to 40 km away from the center, a band that is colder than the model forecast appears, which agrees with the observed features of a rain band in immediate periphery of the hurricane center in Figure 5.6. In both the analysis and observations, the position of the most intense warm core agrees, while the intensity of the observed one is greater than the analysis. It is also worth mentioning is that in both the analysis and observations, cold anomalies exist at the height of about 15 km, but with different intensities and locations relative to the hurricane.

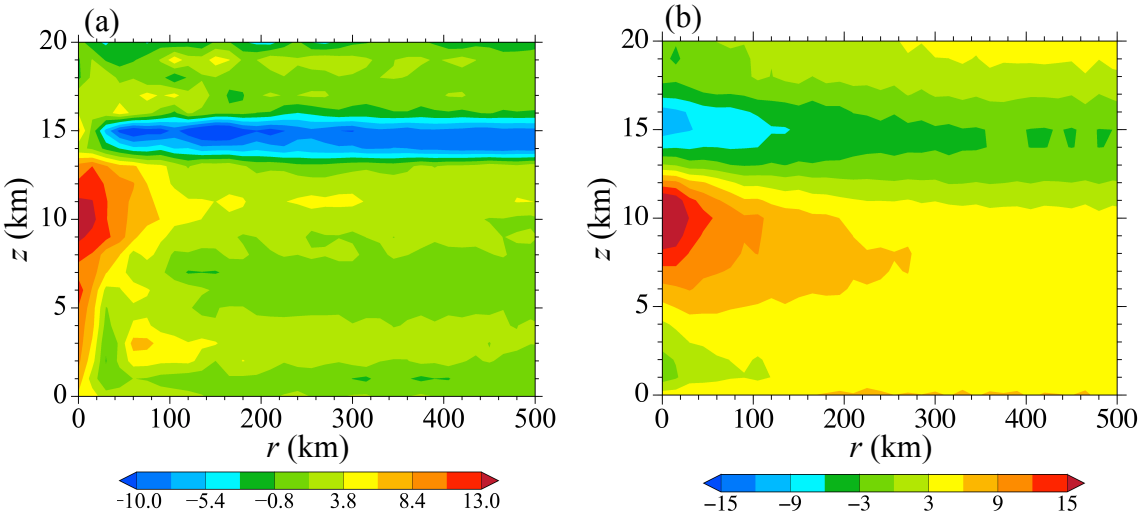

Figure 5.9: The warm core structures of (a) the analysis field and (b) the temperatures retrieved from ATMS observations.

Chapter 6: Summary and Conclusions

6.1 TFI Correction and Detection in AMSR2

In the presence of TFI, the amount of natural radiation emitted by the Earth surface is concealed by the energy from the reflected TV signals. The TFI detection prevents erroneous geophysical retrieval products from being produced by discarding the TFI-affected AMSR2 data. This study aims not only to detect the occurrence of TFI but also to correct the TFI so that these TFI-affected data can be made useful for geophysical variable retrieval. The occurrence of TFI from a particular TV satellite depends on the glint angle and the background TV signal intensity at the AMSR2 observation location. The contribution of the reflected TV signals to an AMSR2 observation at a specific channel can be calculated by an empirical model developed in this research given the AMSR2 glint angle with respect to those TV satellites that can have an effect to the AMSR2 pixel location. The glint angles can be accurately assessed with the instrument's observation geometry. This empirical model can predict the features of oceanic TFI that enable the AMSR2 observations from the natural radiation recovered even at the TV interfered locations. It is shown that positive biases in AMSR2 data are significantly reduced after TFI correction. The TFI-induced errors in the geophysical retrieval products can be considerably reduced over the TFI-contaminated regions so that variations of the retrieval variables are consistent with the vicinity regions. The background TV signal intensity field, once determined, is fixed for future applications as long as the same geostationary TV

satellites are functioning. It is worth emphasizing that the TFI-correction model proposed in this study does not rely on any radiance observations, which was not the case in all of the previous studies. It is pointed out that the effects of surface roughness induced by SSW as well as atmospheric attenuations by water vapor on reflected TV signals are not considered in the empirical model that was developed and tested in this study. Neglect of these two factors results in small negative biases of this TFI correction model. Further investigations are required on accounting quantitatively for the effects of surface roughness and atmospheric attenuation.

Observations of microwave imagers at K-band channels, such as AMSR2, are of significant values for snow and ice retrievals. Since the reflectivity of snow is greater than that of bare land, TV signals from TV geostationary satellites can also be reflected back to space and enter the antenna of microwave radiometers. This study also investigated the K-band channel TFI over land with snow coverage and developed a PCA-based algorithm with TFI glint angles as a constraint. Over North America, TFI signals only exist at K-band channels and bring no correlations with other channels at different frequencies. The natural emissions measured at different frequencies are correlated—even under snowy conditions. A new PCA method is developed for TFI detection over snow-covered land. Small angles between the reflected TV signal vectors and Earth scene vectors of radiometers are necessary conditions for TFI. The conical scan feature of AMSR2 determines that most TFI would occur over areas where the incident angles of TV signals from the geostationary satellites are close to the incident angles of AMSR2. The monthly maximum TFI distribution results from the proposed PCA detection algorithm

confirmed this theoretical expectation. All TFI throughout the month are confined within the areas near the 55◦ incident angle curves of DirecTV-11 and DirecTV-12.

6.2 ATMS and AMSU-A Hurricane Warm Core Retrievals

The improved observing capability of ATMS can be readily applied to monitoring critical weather events such as hurricanes. The temperature retrieval algorithm proposed in previous studies is further improved in order to more accurately retrieve atmospheric temperatures with ATMS observations. As a cross-track microwave scanner, ATMS observations naturally have scan biases, which are found to affect the retrieved temperatures at different pressure levels. To resolve this issue, the regression coefficient training and retrieval process is performed at each individual scan positions. Accordingly, the retrieved atmospheric temperatures from the revised algorithm show no biases related to scan position. The temperature sounding channels of ATMS respond linearly to atmospheric temperature over specific ranges of pressure levels, which is essentially what the weighting function implies. At any pressure level where a given channel's weighting function is close to zero, the atmospheric temperatures and the brightness temperatures turn out to have little correlation. Including all channels in retrievals can even have negative impacts on the accuracies of the retrieved temperatures. In this study, the temperatures in the upper troposphere retrieved when all channels are included are influenced by low-level convection even when convection is absent at upper levels. Therefore, it is not desired to have all temperature sounding channels involved at retrievals of every pressure level. In this study, the involvement of channels at a given pressure level is determined based on the channel's weighting function values and the correlations

between the brightness temperature observations at this channel and the atmospheric temperatures at the given pressure level.

With these refinements incorporated into the retrieval algorithm, the retrieved atmospheric temperatures turn out to be unbiased with respect to scan position and with more accuracy when compared with the temperature fields in GFS analysis. The observations covering the period of Hurricane Sandy when it is located in both the tropics and mid-latitudes are examined with the traditional and revised retrieval algorithms, respectively. It is found that the revised algorithm can capture the asymmetric warm core structures of Hurricane Sandy despite the storm's position within a swath. The warm cores retrieved at upper troposphere are more homogenous compared with the traditional algorithm. The warm core features from the revised method applied to ATMS and AMSU-A observations on board S-NPP and NOAA 18 are compared with the warm cores calculated with temperature profiles retrieved with the same instrument from the operational MIRS retrieval for Hurricane Sandy (2012) and Hurricane Michael (2012), respectively. It was shown that the horizontal and vertical structures of warm cores from the revised new algorithm are more realistic than those from the MIRS operational retrieval. In the future, the retrieved temperatures at stratosphere levels will be examined, as channels 9-15 of ATMS have their peak weighting functions at levels above 200 hPa.

6.3 A Simplified 4D-Var Vortex Initialization Model

With the purpose of initializing more realistic hurricane vortices for numerical forecast models to integrate from, a simplified 4D-Var assimilation model is proposed based on an axisymmetric hurricane simulation model proposed by Rotunno and

Emanuel (1987). The model is nonhydrostatic and most applicable in cases where the hurricanes are relatively mature. Its axisymmetric nature limits the model from accounting for any asymmetric features of storms. Nonetheless, the structural features of hurricanes given by this model are dynamically consistent between all model variables in the axisymmetric domain. When observations are assimilated with the 4D-Var method, the increments will be constrained by the dynamical relationships and, therefore, also dynamically coherent. Hereby the initialized vortices are both observation-based and dynamically consistent. When incorporated into HWRF, the spinup time for the hurricane forecast model is expected to be less than the cases with empirically specified vortices.

The tangent linear model and adjoint model are developed for the calculation of cost function gradients. The observation operators transforming model variables to match with both ATMS and AMSR2 observations are also written. The correctness of the TLM, adjoint model, and gradient calculations are checked to ensure the assimilation process converges. Overall, the developed assimilation model takes the three-dimensional temperature field retrieved with ATMS radiance observations, liquid water path and total precipitable water retrieved with AMSR2 radiance observations as input and incorporates it into the hurricane model to generate dynamically consistent vortices. With both the dynamical consistency and observed realistic features, the resulting vortices will hopefully help to improve intensity forecast accuracies in hurricane predictions. In this research, a case study about Hurricane Gaston (2016) is performed. The model forecast is first matched with the BestTrack records of Hurricane Gaston. Both the ATMS and AMSR2 observations

are assimilated into the hurricane initialization model. The minimization of the cost function reaches the minimum within 23 iterations. The resulting vortex is compared with the original hurricane model forecast, i.e. the first guess, and with the observed structures. It is found that, in regions near the storm center, low-level winds tend to be intensified with upper-level ones weakened in the analysis field. The warm core structure is modified so that a rain-band like feature is manifested in low-level areas. However, the increments of water vapor and liquid water mixing ratios prove to be almost negligible in magnitudes when compared with the model variables themselves.

Future work will start with this initialization model and incorporate the RE model and its tangent linear and adjoint operators and the resulting satellite observation based vortices into the HWRF system to improve hurricane track and intensity forecasts. The asymmetric features can be obtained by integrating the baratropic vorticity equation with a symmetric initial condition as described in Zou et al. (2015). The performances of the forecasts with the original HWRF bogus vortices and with the vortices resulting from the simplified assimilation model will be compared.

References

Adams, I. S., M. H. Bettenhausen, P. W. Gaiser, and W. Johnston, 2010: Identification of Ocean-Reflected Radio-Frequency Interference Using WindSat Retrieval Chi-Square Probability. *IEEE Trans. Geosci. Remote Sens.*, **7,** 406-410.

Bender, M. A., R. J. Ross, R. E. Tuleya, and Y. Kurihara, 1993: Improvements in Tropical Cyclone Track and Intensity Forecasts Using the GFDL Initialization System. *Mon. Wea. Rev.*, **121,** 2046-2061.

Boukabara, S. A., and Coauthors, 2011: MiRS: An All-Weather 1DVAR Satellite Data Assimilation and Retrieval System. *IEEE Trans. Geosci. Remote Sens.*, **49,** 3249-3272.

Chen, H., and D.-L. Zhang, 2012: On the Rapid Intensification of Hurricane Wilma (2005). Part II: Convective Bursts and the Upper-Level Warm Core. *J. Atmos. Sci.*, **70,** 146-162.

Chen, Y., Y. Han, and F. Weng, 2013: Detection of Earth-rotation Doppler Shift from Suomi National Polar-Orbiting Partnership Cross-Track Infrared Sounder. *Appl. Opt.*, **52,** 6250-6257.

Demuth, J. L., M. DeMaria, and J. A. Knaff, 2006: Improvement of Advanced Microwave Sounding Unit Tropical Cyclone Intensity and Size Estimation Algorithms. *J. Appl. Meteorol.*, **45,** 1573-1581.

Demuth, J. L., M. DeMaria, J. A. Knaff, and T. H. Vonder Haar, 2004: Evaluation of Advanced Microwave Sounding Unit Tropical-Cyclone Intensity and Size Estimation Algorithms. *J. Appl. Meteorol.*, **43,** 282-296.

Dolling, K., and G. M. Barnes, 2011: Warm-Core Formation in Tropical Storm Humberto (2001). *Mon. Wea. Rev.*, **140,** 1177-1190.

Emanuel, K. A., 1986: An Air-Sea Interaction Theory for Tropical Cyclones. Part I: Steady-State Maintenance. *J. Atmos. Sci.*, **43,** 585-605.

Ferraro, R. R., N. C. Grody, F. Weng, and A. Basist, 1996: An Eight-Year (1987–1994) Time Series of Rainfall, Clouds, Water Vapor, Snow Cover, and Sea Ice Derived from SSM/I Measurements. *Bull. Am. Meteorol. Soc.*, **77,** 891-905.

Galarneau, T. J., C. A. Davis, and M. A. Shapiro, 2013: Intensification of Hurricane Sandy (2012) through Extratropical Warm Core Seclusion. *Mon. Wea. Rev.*, **141,** 4296-4321.

Gall, R., J. Franklin, F. Marks, E. N. Rappaport, and F. Toepfer, 2012: The Hurricane Forecast Improvement Project. *Bull. Am. Meteorol. Soc.*, **94,** 329-343.

Hilton, F., and Coauthors, 2011: Hyperspectral Earth Observation from IASI: Five Years of Accomplishments. *Bull. Am. Meteorol. Soc.*, **93,** 347-370.

Janssen, M. A., 1993: Atmospheric Remote Sensing by Microwave Radiometry. *Wiley Ser. Remote Sens.*, John Wiley & Sons, Ltd., 572.

Kachi, M., and Coauthors, 2008: Status of GCOM-W1/AMSR2 development and science activities. *Proc. SPIE*, 71060P-71060P-71068.

Kelly, R., 2009: The AMSR-E snow depth algorithm: Description and initial results. *J. Remote Sens. Soc. Jpn.*, **29,** 307-317.

Kelly, R. E., A. T. Chang, T. Leung, and J. L. Foster, 2003: A Prototype AMSR-E Global Snow Area and Snow Depth Algorithm. *IEEE Trans. Geosci. Remote Sens.*, **41,** 230-242.

Kidder, S. Q., and Coauthors, 2000: Satellite Analysis of Tropical Cyclones Using the Advanced Microwave Sounding Unit (AMSU). *Bull. Am. Meteorol. Soc.*, **81,** 1241-1259.

Kurihara, Y., M. A. Bender, and R. J. Ross, 1993: An Initialization Scheme of Hurricane Models by Vortex Specification. *Mon. Wea. Rev.*, **121,** 2030-2045.

Kurihara, Y., M. A. Bender, R. E. Tuleya, and R. J. Ross, 1990: Prediction Experiments of Hurricane Gloria (1985) Using a Multiply Nested Movable Mesh Model. *Mon. Wea. Rev.*, **118,** 2185-2198.

——, 1995: Improvements in the GFDL Hurricane Prediction System. *Mon. Wea. Rev.*, **123,** 2791-2801.

LeMarshall, J., and Coauthors, 2006: Improving Global Analysis and Forecasting with AIRS. *Bull. Am. Meteorol. Soc.*, **87,** 891-894.

Li, L., P. W. Gaiser, M. H. Bettenhausen, and W. Johnston, 2006: WindSat Radio-Frequency Interference Signature and Its Identification over Land and Ocean. *IEEE Trans. Geosci. Remote Sens.*, **44,** 530-539.

Liu, D. C., and J. Nocedal, 1989: On the Limited Memory BFGS Method for Large Scale Optimization. *Math. Prog.*, **45,** 503-528.

Liu, Q., and Coauthors, 2006: Hurricane initialization in HWRF model. *27th Conference on hurricanes and tropical meteorology*, Monterey, CA, Amer. Meteor. Soc. P.

Liu, Y., D.-L. Zhang, and M. K. Yau, 1999: A Multiscale Numerical Study of Hurricane Andrew (1992). Part II: Kinematics and Inner-Core Structures. *Mon. Wea. Rev.*, **127,** 2597-2616.

McKague, D., J. J. Puckett, and C. Ruf, 2010: Characterization of K-band radio frequency interference from AMSR-E, WindSat and SSM/I. *IEEE International Geoscience and Remote Sensing Symposium (IGARSS)*, IEEE, 2492-2494.

Navon, I. M., X. Zou, J. Derber, and J. Sela, 1992: Variational data assimilation with an adiabatic version of the NMC spectral model. *Mon. Wea. Rev.*, **120,** 1433-1446.

Njoku, E. G., and L. Li, 1999: Retrieval of Land Surface Parameters Using Passive Microwave Measurements at 6-18 GHz. *IEEE Trans. Geosci. Remote Sens.*, **37,** 79-93.

Njoku, E. G., T. J. Jackson, V. Lakshmi, T. K. Chan, and S. V. Nghiem, 2003: Soil Moisture Retrieval from AMSR-E. *IEEE Trans. Geosci. Remote Sens.*, **41,** 215-229.

Park, K., and X. Zou, 2004: Toward Developing an Objective 4DVAR BDA Scheme for Hurricane Initialization Based on TPC Observed Parameters. *Mon. Wea. Rev.*, **132,** 2054-2069.

Poisel, R., 2012: *Antenna systems and electronic warfare applications.* Artech House.

Pu, Z.-X., and S. A. Braun, 2001: Evaluation of Bogus Vortex Techniques with Four-Dimensional Variational Data Assimilation. *Mon. Wea. Rev.*, **129,** 2023-2039.

Rotunno, R., and K. A. Emanuel, 1987: An Air–Sea Interaction Theory for Tropical Cyclones. Part II: Evolutionary Study Using a Nonhydrostatic Axisymmetric Numerical Model. *J. Atmos. Sci.*, **44,** 542-561.

Spencer, R. W., and W. D. Braswell, 2001: Atlantic Tropical Cyclone Monitoring with AMSU-A: Estimation of Maximum Sustained Wind Speeds. *Mon. Wea. Rev.*, **129,** 1518-1532.

Thu, T. V., and T. N. Krishnamurti, 1992: Vortex initialization for typhoon track prediction. *Meteor. Atmos. Phys.*, **47,** 117-126.

Tian, X., and X. Zou, 2016: An Empirical Model for Television Frequency Interference Correction of AMSR2 Data Over Ocean Near the U.S. and Europe. *IEEE Trans. Geosci. Remote Sens.*, **54,** 3856-3867.

Truesdale, D., 2013: A Probability Distribution Method for Detecting Radio-Frequency Interference in WindSat Observations. *IEEE Trans. Geosci. Remote Sens.*, **51,** 3780-3788.

Wang, Y., 1995: An Inverse Balance Equation in Sigma Coordinates for Model Initialization. *Mon. Wea. Rev.*, **123,** 482-488.

Weng, F., and N. C. Grody, 1994: Retrieval of Cloud Liquid Water Using the Special Sensor Microwave Imager (SSM/I). *J. Geophys. Res.*, **99,** 25535-25551.

Weng, F., X. Zou, X. Wang, S. Yang, and M. D. Goldberg, 2012: Introduction to Suomi National Polar-orbiting Partnership Advanced Technology Microwave Sounder for Numerical Weather Prediction and Tropical Cyclone Applications. *J. Geophys. Res.*, **117,** 2156-2202.

Weng, F., L. Zhao, R. R. Ferraro, G. Poe, X. Li, and N. C. Grody, 2003: Advanced Microwave Sounding Unit Cloud and Precipitation Algorithms. *Radio Sci.*, **38,** 3301-3313.

Wentz, F. J., and T. Meissner, 2000: Algorithm Theoretical Basis Document (ATBD) AMSR Ocean Algorithm, 2nd Ed., IEEE.

Wilheit, T., C. D. Kummerow, and R. Ferraro, 2003: NASDA Rainfall Algorithms for AMSR-E. *IEEE Trans. Geosci. Remote Sens.*, **41,** 204-214.

Wiltshire, W. M., M. D. Nilsson, and F. B. Campbell, 2004: Application for Authorization to Launch and Operate DirecTV 10, a Partial Replacement Ka-Band Satellite, at 103 deg. Tech. Rep.

Xiao, Q., X. Zou, and B. Wang, 2000: Initialization and Simulation of a Landfalling Hurricane Using a Variational Bogus Data Assimilation Scheme. *Mon. Wea. Rev.*, **128,** 2252-2269.

Yan, B., and F. Weng, 2008: Applications of AMSR-E measurements for tropical cyclone predictions Part I: Retrieval of Sea Surface Temperature and Wind speed. *Adv. Atmos. Sci.*, **25,** 227-245.

Yang, H., and F. Weng, 2016: Corrections for On-Orbit ATMS Lunar Contamination. *IEEE Trans. Geosci. Remote Sens.*, **54,** 1918-1924.

Zhang, D.-L., and H. Chen, 2012: Importance of the Upper-level Warm Core in the Rapid Intensification of a Tropical Cyclone. *Geophys. Res. Lett.*, **39,** n/a-n/a.

Zhao, J., X. L. Zou, and F. Z. Weng, 2013: WindSat Radio-Frequency Interference Signature and Its Identification Over Greenland and Antarctic. *IEEE Trans. Geosci. Remote Sens.*, **51,** 4830-4839.

Zhu, C., R. H. Byrd, P. Lu, and J. Nocedal, 1997: Algorithm 778: L-BFGS-B: Fortran Subroutines for Large-scale Bound-Constrained Optimization. *ACM Trans.Math. Softw.*, **23,** 550-560.

Zhu, T., and F. Weng, 2013: Hurricane Sandy Warm-core Structure Observed from Advanced Technology Microwave Sounder. *Geophys. Res. Lett.*, **40,** 3325-3330.

Zhu, T., D. Zhang, and F. Weng, 2002: Impact of the Advanced Microwave Sounding Unit Measurements on Hurricane Prediction. *Mon. Wea. Rev.*, **130,** 2416-2432.

Zou, X., and Q. Xiao, 2000: Studies on the Initialization and Simulation of a Mature Hurricane Using a Variational Bogus Data Assimilation Scheme. *J. Atmos. Sci.*, **57,** 836-860.

Zou, X., I. M. Navon, and J. Sela, 1993: Control Of Gravitational Oscillations in Variational Data Assimilation. *Mon. Wea. Rev.*, **121,** 272-289.

Zou, X., X. Tian, and F. Weng, 2014: Detection of Television Frequency Interference with Satellite Microwave Imager Observations over Oceans. *J. Atmos. Ocean. Technol.*, **31,** 2759-2776.

Zou, X., Z. Qin, and Y. Zheng, 2015: Improved Tropical Storm Forecasts with GOES-13/15 Imager Radiance Assimilation and Asymmetric Vortex Initialization in HWRF. *Mon. Wea. Rev.*, **143,** 2485-2505.

Zou, X., F. Vandenberghe, M. Pondeca, and Y.-H. Kuo, 1997: Introduction to Adjoint Techniques and the MM5 Adjoint Modeling System.

Zou, X., J. Zhao, F. Weng, and Z. Qin, 2012: Detection of Radio-Frequency Interference Signal Over Land From FY-3B Microwave Radiation Imager (MWRI). *IEEE Trans. Geosci. Remote Sens.*, **50,** 4994-5003.

Zou, X., F. Weng, B. Zhang, L. Lin, Z. Qin, and V. Tallapragada, 2013: Impacts of Assimilation of ATMS Data in HWRF on Track and Intensity Forecasts of 2012 Four Landfall Hurricanes. *J. Geophys. Res.*, **118,** 11,558-511,576.